

University of Southampton Research Repository

Copyright © and Moral Rights for this thesis and, where applicable, any accompanying data are retained by the author and/or other copyright owners. A copy can be downloaded for personal non-commercial research or study, without prior permission or charge. This thesis and the accompanying data cannot be reproduced or quoted extensively from without first obtaining permission in writing from the copyright holder/s. The content of the thesis and accompanying research data (where applicable) must not be changed in any way or sold commercially in any format or medium without the formal permission of the copyright holder/s.

When referring to this thesis and any accompanying data, full bibliographic details must be given, e.g.

Thesis: Author (Year of Submission) "Full thesis title", University of Southampton, name of the University Faculty or School or Department, PhD Thesis, pagination.

Data: Author (Year) Title. URI [dataset]

University of Southampton

Faculty of Physical and Applied Sciences

School of Physics and Astronomy

**Carrier Recombination Kinetics in Organometal Trihalide Perovskites
Thin Films**

by

Giacomo Marco Piana

Thesis for the degree of Doctor of Philosophy

March 2019

University of Southampton

Abstract

Faculty of Physical and Applied Sciences

School of Physics and Astronomy

Doctor of Philosophy

**Carrier Recombination Kinetics in Organometal Trihalide Perovskites
Thin Films**

By

Giacomo Marco Piana

This work focuses on the description of recombination dynamics in hybrid lead iodide perovskites of composition methylammonium lead tri-iodide (MAPbI_3). Time-resolved spectroscopy was used as main tool to investigate the carrier dynamics in these systems. Further a model was constructed, which is able to accurately reproduce the observed features of the observed dynamical features.

Herein, we will present a series of spectroscopic experiments and we will discuss in detail their results. We will show how the insights on crucial properties of the perovskites, like their exciton binding energy, are necessary for a correct formulation of the model proposed. Later, we will explore various aspects of the model itself and guide the reader into the detailed analysis of each recombination pathway for each of the charges species involved. We aim with this work at providing a deeper understanding on the nature of the electronic and excitonic transitions in hybrid perovskites

We believe that this can aid the perovskite photovoltaics community in developing a clear understanding of some of the important optoelectronic properties. We believe that this in turn will help the development of a more efficient generation of photovoltaic materials, in a historical moment where clean and renewable energy sources is of vital importance for the future of humankind.

Table of Contents

Table of Contents	i
Table of Tables	v
Table of Figures	vii
List of Publications	xiii
Research Thesis: Declaration of Authorship	xv
Acknowledgements	xvii
Chapter 1 Introduction	1
1.1 Motivation of this Thesis	1
1.2 Perovskites carrier dynamics.....	2
Chapter 2 Hybrid Perovskite for Solar Cells	5
2.1 Introduction.....	5
2.2 Crystal Structure and Composition	5
2.3 Methylammonium Lead Trihalide Perovskites.....	7
2.4 Optoelectronics Properties.....	8
Chapter 3 Experimental Techniques	13
3.1 Introduction	13
3.2 Time Resolved Photoluminescence.....	13
3.2.1 Ultrafast Time-Resolved and Steady-State PL setup	13
3.3 Linear Absorption Spectroscopy.....	15
3.4 Sample Preparation	17
3.5 Numerical integration of differential equations	18
Chapter 4 Exciton Binding Energy	21
4.1 Introduction	21
4.2 Exciton Binding Energy from Absorption Measurements.....	23
4.2.1 Elliott's Theory.....	23
4.2.2 Results and discussion	25

Table of Contents

4.3	Urbach Energy	29
4.4	Excitons vs Free carriers	31
4.4.1	Saha equation theory	31
4.4.2	Exciton and free-carriers as a function of N , E_b , T and trap density .	33
Chapter 5	Steady State PL analysis	39
5.1	Introduction.....	39
5.2	PL vs Temperature.....	39
5.2.1	Tetragonal and Orthorhombic phases	39
5.2.2	Temperature-Dependent Linewidth Broadening.....	41
5.3	PL vs Excitation Density	43
5.3.1	Dependence of NBEPL on Excitation Power.....	43
5.3.2	Results and discussion.....	49
Chapter 6	Recombination Processes in Methylammonium Lead Trihalide Perovskites.....	53
6.1	Introduction.....	53
6.2	Recombination Processes Model	55
6.2.1	Rate Equations for the Recombination Processes	56
6.3	Preliminary Considerations on the Recombination Processes	57
6.3.1	Exciton Formation and Dissociation.....	57
6.3.2	Phonon Assisted Rates	62
6.3.3	Dependence of k_{eh} on T and E_g	63
6.3.4	Charges accumulation	63
6.4	Results and discussion.....	64
6.4.1	Tetragonal Phase	65
6.4.2	Orthorhombic phase	72
6.4.3	Influence of T and $N(0)$ on the decay dynamics.....	78
6.5	Conclusions.....	84

Chapter 7 Low-dimensional emissive states in non-stoichiometric methylammonium lead halide perovskites	85
7.1 Introduction	85
7.2 Samples preparation, topographical and structural analysis	88
7.3 94	
7.4 Steady-State Photoluminescence Properties	94
7.5 Time-Resolved Photoluminescence properties	103
7.6 Conclusions	110
Chapter 8 Conclusions	113
8.1 Future Work	114
Bibliography	117

Table of Tables

Table 5-1: Values of the power exponent k for different radiative recombination routes. 49

Table 6-1: Results of the global fit for the tetragonal peak. 70

Table of Figures

Figure 1-1: NREL research cell efficiency records between 1976 and 2018.	2
Figure 2-1: Generic cubic perovskite structure of the form ABX₃.	6
Figure 2-2: Crystalline structures corresponding to MAPI Cubic, Tetragonal and Orthorhombic phases [6].	7
Figure 2-3: Schematic representation of the formation of defect states within VB and CB in APbX₃ perovskites Adapted from [12].	9
Figure 2-4: Variation of the absorption spectra as a function of the iodide-bromide ratio x in lead mixed halogen perovskites thin films [15].	10
Figure 2-5: Absorption coefficient (α) versus wavelength of thin films of perovskite CH₃NH₃PbI₃ plotted together with the AM 1.5G solar spectrum. Adapted from [18].	11
Figure 3-1: Schematic depiction of the automated power-dependent time-resolved spectroscopy setup.	15
Figure 3-2: Schematics representing the setup for transmittance measurements.	16
Figure 3-3: Schematics representing the setup for reflectance measurements.	16
Figure 4-1: Transmission of the MAPI thin-film versus temperature. Steady-state PL of the tetragonal phase a) and orthorhombic phase b) MAPI versus temperature.	26
Figure 4-2: Absorption coefficient versus photon energy obtained for MAPI thin films at different temperatures for the tetragonal phase.	27
Figure 4-3: Absorption coefficient versus photon energy obtained for MAPI thin films at different temperatures for the orthorhombic phase.	28

Table of Figures

Figure 4-4: Temperature dependent results for band gap and exciton binding energy from the Elliott's theory modelling.....	29
Figure 4-5: $\ln(\alpha)$ versus photon energies less than the bandgap for different temperatures.	30
Figure 4-6: Electron densities as a function of T for different excitation densities at fixed exciton binding energy.....	34
Figure 4-7: Excitons densities as a function of T for different excitation densities at fixed exciton binding energy.....	34
Figure 4-8:Ratio between electron and exciton densities as a function of T for different excitation density at fixed exciton binding energy....	35
Figure 4-9:Fraction of electrons and excitons over the total photo-generated charges as a function of T for different excitation density at fixed exciton binding energy.	35
Figure 4-10: Fraction of electrons and excitons over the total photo-generated charges as a function of T for different exciton binding energy at fixed excitation density.	37
Figure 4-11: Fraction of electrons and excitons over the total photo-generated charges as a function of T for different doping densities at fixed exciton binding energy and excitation power.	38
Figure 5-1: Temperature map of time integrated PL of MAPI thin film.	40
Figure 5-2: Experimental and fitted values of FWHM of the PL emission corresponding to the tetragonal phase of MAPI.....	42
Figure 5-3: Radiative and non-radiative transitions included in the model for NBEPL.	44
Figure 5-4: PL vs Excitation Fluence at 290 (a) K and 140 K (b).	50

Figure 5-5: Fit PL vs Intensity for the tetragonal peak (red) and orthorhombic (blue) .	51
Figure 6-1: Schematic diagram of recombination processes in a semiconductor material.	54
Figure 6-2: Radiative and nonradiative transitions included in the model for carrier recombination dynamics in MAPI thin films.	55
Figure 6-3: Electron and exciton density as function of the rate r^0.	59
Figure 6-4: Equilibrium densities as a function of delay time for different values of r^0.	60
Figure 6-5: Free electrons, free excitons and equilibrium densities as a function of delay time for different values of r^0.	61
Figure 6-6: Normalised TRPL spectra of the tetragonal peak. High temperature phase range.	67
Figure 6-7: Normalised TRPL spectra of the tetragonal peak. Low temperature phase range.	69
Figure 6-8: Fitted temperature dependence of trap capture rate, trap re-excitation and trap depopulation for electrons and excitons for the tetragonal phase.	71
Figure 6-9: Fitted electrons (red) and excitons (blue) trap densities as a function of T for the tetragonal peak.	72
Figure 6-10: Normalised TRPL spectra of the orthorhombic peak.	75
Figure 6-11: Fitted temperature dependence of trap capture rate, trap excitation and trap depopulation for electrons and excitons for the tetragonal phase.	77

Table of Figures

Figure 6-12: Fitted electrons (red) and excitons (blue) trap densities as a function of T for the orthorhombic peak.	78
Figure 6-13: Delay time dependence of free and trapped electrons at room temperature for the tetragonal peak emission, for different excitation densities.	79
Figure 6-14: Bimolecular recombination for not doped and doped systems at different excitation densities.	80
Figure 6-15: Time-Resolve PL spectra of MAPI recorded at 290, 260 and 200K showing the fast component of the decay.	81
Figure 6-16: Electron and exciton densities as a function of the carrier excitation density for T=140K.	82
Figure 6-17: Delay time dependence of free and trapped excitons at room temperature for the tetragonal peak emission, for different excitation densities.	83
Figure 7-1: Crystal structure for n=1,2,3 and ∞ perovskites from a parent ABX3 structure (from reference 84).	86
Figure 7-2: Scanning microscope images and atomic force microscopy images for the samples 2.5:1, 3:1 and 3.5:1 (Courtesy of Ben Freestone).	89
Figure 7-3: GIWAS detector patterns from air annealed (a) and nitrogen annealed (b) 3.5:1 samples. Radial integration of three 3.5:1 samples (c) and azimuthal integration around Q for glove box and air annealed 3.5:1 samples (d) (Courtesy of Ben Freestone)	91
Figure 7-4: Simulated powder-XRD patterns and radially integrated GIWAS for 3.5:1 glove box annealed sample (Courtesy of Ben Freestone).	93

<i>Figure 7-5: Model structure representation of the quasi 2D perovskite structure (Courtesy of Ben Freestone).</i>	94
<i>Figure 7-6: Absorption and ssPL spectra for reference and 3.5:1 sample at room temperature and 12 K.</i>	96
<i>Figure 7-7: Temperature dependent normalised steady state PL from a 2.5:1 and 3:1 film.</i>	98
<i>Figure 7-8: Temperature dependent normalised steady state PL from a 3.5:1 film deposited on PEDOT:PSS and deposited on quartz.</i>	100
<i>Figure 7-9: Normalised steady state PL from 3.5:1 films deposited on PEDOT:PSS annealed on nitrogen, air and from a 4:1 film.</i>	102
<i>Figure 7-10: Comparison of the TRPL spectra at different temperatures for the lower energy emission of films obtained from non-stoichiometric precursors.</i>	105
<i>Figure 7-11: Low dimensionality emissive states TRPL spectra of a 3.5:1 film on quartz.</i>	108
<i>Figure 7-12: Decay rates k_1 and k_2 of double stretched exponential fit for 3.5:1 film on quartz.</i>	109

List of Publications

- *Phonon-Assisted Trapping and Re-excitation of Free Carriers and Excitons in Lead Halide Perovskites*

Giacomo M. Piana, Christopher G. Bailey, and Pavlos G. Lagoudakis

The Journal of Physical Chemistry C, 2019, **123** (32), 19429-19436

- *Low-dimensional emissive states in non-stoichiometric methylammonium lead halide perovskites*

Benjamin G. Freestone, Joel A. Smith, Giacomo M. Piana, Rachel C. Kilbride, Andrew J. Parnell, Luca Sortino, David M. Coles Orianna B. Ball, Natalia Martsinovich, Courtney J. Thompson, Tarek I. Alanazi, Onkar S. Game, Alexander I. Tartakovskii, Pavlos Lagoudakis and David G. Lidzey

Journal of Materials Chemistry A 2019, **7**, 11104-11116

- *Efficient light harvesting in hybrid quantum dot-interdigitated back contact solar cell via resonant energy transfer and luminescent downshifting*

Chirenjeevi Krishnan, Thomas Mercier, Tasmiat Rahman, Giacomo M. Piana, Mael Brossard, Timur Yagafarov, Alexander To, Michael E. Pollard, Peter Shaw, Darren M. Bagnall, Bram Hoex, Stuart A. Boden, Pavlos G. Lagoudakis and Martin D. B. Charlton

Nanoscale, 2019, **11**, 18837-18844

- *High-Energy Optical Transitions and Optical Constants of $CH_3NH_3PbI_3$ Measured by Spectroscopic Ellipsometry and Spectrophotometry*

Christopher G. Bayley, Giacomo M. Piana and Pavlos G. Lagoudakis

Under review { preprint arXiv:1909.03907

Conferences

- *Temperature dependent photoluminescence measurements on $CH_3NH_3PbI_{3-x}Cl_x$.*

Giacomo M. Piana, Christopher G. Bailey, and Pavlos G. Lagoudakis

International Conference on Hybrid and Organic Photovoltaics
(HOPV 16), Swansea, 2016 – Poster presentation

- *Effect of light soaking and ambient conditions on charge carrier dynamics in $CH_3NH_3PbI_3$ and $CH_3NH_3PbI_{3-x}Cl_x$ thin films.*

Giacomo M. Piana, Christopher G. Bailey, and Pavlos G. Lagoudakis

International Conference on Hybrid and Organic Photovoltaics
(HOPV 17), Lausanne, 2017 – Poster presentation

- *Excitons and free charges recombination dynamics modeling in $CH_3NH_3PbI_3$ thin films.*

Giacomo M. Piana, Christopher G. Bailey, and Pavlos G. Lagoudakis

International Conference on Physics of Light-Matter Coupling in
Nanostructures

(PLMCN-20), Moscow, 2019 – Poster presentation

Research Thesis: Declaration of Authorship

Print name:	Giacomo Marco Piana
-------------	---------------------

Title of thesis:	Carrier Recombination Kinetics in Organometal Trihalide Perovskites Thin Films
------------------	---

I declare that this thesis and the work presented in it are my own and has been generated by me as the result of my own original research.

I confirm that:

1. This work was done wholly or mainly while in candidature for a research degree at this University;
2. Where any part of this thesis has previously been submitted for a degree or any other qualification at this University or any other institution, this has been clearly stated;
3. Where I have consulted the published work of others, this is always clearly attributed;
4. Where I have quoted from the work of others, the source is always given. With the exception of such quotations, this thesis is entirely my own work;
5. I have acknowledged all main sources of help;
6. Where the thesis is based on work done by myself jointly with others, I have made clear exactly what was done by others and what I have contributed myself;
7. None of this work has been published before submission

Signature:		Date:	25/03/2019
------------	--	-------	------------

Acknowledgements

Grazie a tutti di cuore

Chapter 1 **Introduction**

1.1 **Motivation of this Thesis**

Never in the past has the world faced such a huge need for clean energy as it does today. The global population, which is in constant growth and has many rapidly expanding economies, challenges the old western economies on many levels. One aspect of this competition is the control of fossil fuel reserves. As fossil fuel consumption exponentially increases, estimations predict that only a few hundred years' supply may be available. Effects of this new era of competition for resources stacks with all the scars left on Earth by the abuse of non-renewable energy sources. The combination of the two is clearly visible in its absolutely detrimental results. Moreover, the shortage of fossil fuels is an even more serious problem in the countries of the “old” Europe, which possess a limited number of natural resources when compared to other continents. These and similar reasons led in the past to the development of many alternative energy sources. Among these, photovoltaics (PV) gained one of the most recognisable status among public opinion. This has helped to channel attention and resources into the research and development of technologies that are at present day a competitive and reliable alternative to fossil fuels. The photovoltaic effect relies on light in order to generate electrical energy that can be then harvested. But even if the Sun will provide free energy for several millions of years, there is another aspect on which the photovoltaic effect heavily relies on. This is the ability of a material to be able to transform the incoming radiation into electrical charges. Unfortunately, the availability of these materials is not as abundant as sunlight. Therefore, an increasing demand in renewable energy translates directly into the demand for new, abundant and more efficient photovoltaics technologies. Current commercial mainstream technologies have probably reached, or will soon reach, the theoretical peak of their efficiency, like for example silicon-based PV. In other cases, their possibility to be scaled to high volumes of production will never be possible, because these technologies rely on rare or expensive materials.

Experimental Techniques

One particular class of hybrid semiconductor materials, however, is beginning to address existing problems of developing renewable energy solutions. Perovskites have recently begun attracting the attention of scientists and those interested in making the Earth a greener planet. Their potential of providing low cost and energy-efficient renewable energy shows considerable potential of address current issues of renewable energy

1.2 Perovskites carrier dynamics

Since the breakthrough paper of 2012 [1], perovskite solar cells have drawn great interest in the PV community. This interest directly correlated to a rise in the efficiency over time never seen before between all the existing PV technologies.

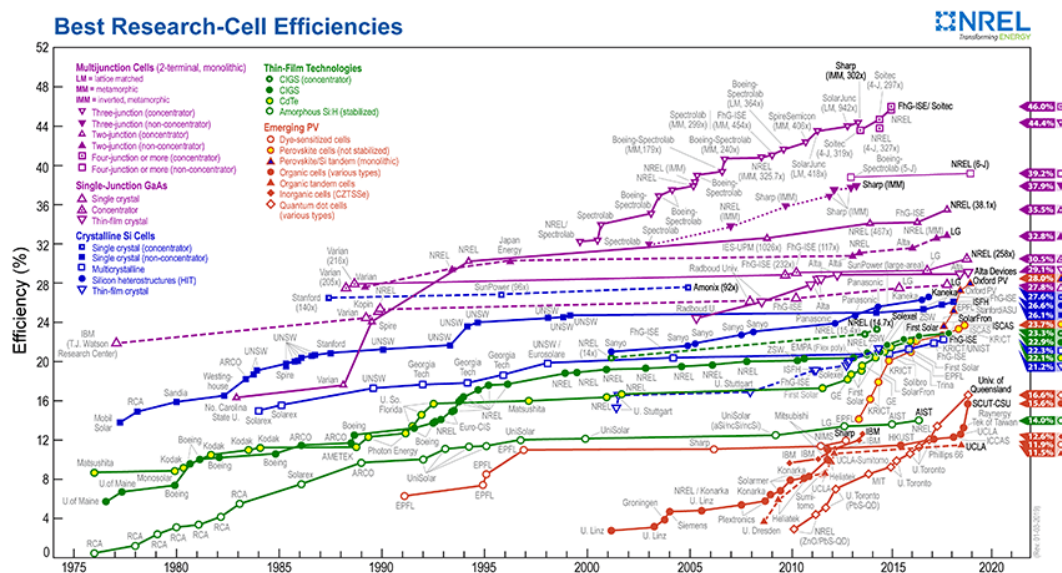


Figure 1-1: NREL research cell efficiency records between 1976 and 2018.
Perovskite cells are shown as red and yellow circles.

Therefore, more efficient perovskite solar cells were expected to reach in excess of 20% power conversion efficiency (PCE), based on the possibility of better engineering this family of devices thanks to the contribution from the modern infrastructures and research technologies. The breakthrough of 20% PCE finally was observed in 2016 [2]. At the time the we are writing this thesis the record for perovskite cells amounts an astonishing 23.3% being certified in 2018, as can be seen in Figure 1-1. Moreover, perovskite solar cells promised so far to have the

three key features to be a truly low cost per watt serious competitor to Si in the PV market. These are high efficiency, low manufacturing cost and long lifetime. The previous chart just showed the potential for future efficiency escalation. Sufficiently long lifetime is arguably at the moment the most uncertain criteria for perovskite PV, since it is not yet proven. Finally, the low manufacturing cost and the related problem of large-scale production seems to be one of the highlights of this technology. Also evident is the advantage over other solar cells that use significantly less abundant or more expensive elements (Te, In etc). It is also evident how vast the parameter space is for potential material combination, dependent on which atoms or molecules are used in the perovskite structure. This aspect plays a crucial role for determining and selecting the most performing optical and electronic properties, such as bandgap and absorption, mobility and diffusion length.

Despite all these promising premises many aspects of perovskite based solar cells are under vivid debate. Topics include the previously mentioned lifetime and the presence of lead. Furthermore, there has also been discussion on the optical density and absorption of these materials which is lower than other thin film absorbing materials. As a result, the perovskites devices require thicker light-harvesting layers (hundreds of nanometres) which may cause some fabrication limitations; particularly for solution processed devices where creating such thick layer with high uniformity can be difficult. Finally, it is important to stress how the operational methods and physical phenomena underlying the behaviour of perovskite PV are still relatively new and not fully understood. A deeper understanding of the photo physics and structural chemistry is necessary both under a pure scientific point of view and also as theoretical background for a full optimization of the devices. Finally, perovskites have shown an excellent incorporation into standards organic photovoltaics (OPV) and thin film architectures, together with the development of a low temperature solution-based production process with high scalability potential.

Chapter 2 Hybrid Perovskite for Solar Cells

2.1 Introduction

The following chapter will introduce some of the crystallographic and photo physical properties of lead iodide hybrid perovskites. First a brief introduction to the structure and phase properties of the general class of materials will be given in Section 2.2. Following this a more detailed description of methylammonium lead iodide (MAPI) perovskites will be provided in section 2.3. The chapter is then concluded in Section 2.4 with an overview of the optoelectronic properties that are more relevant to the energy harvesting application of these materials.

2.2 Crystal Structure and Composition

The name Perovskites identifies a general crystal structure that was discovered in Russia in the early XIX century while studying calcium titanate minerals of composition CaTiO_3 . Due to the large variety of chemical compounds that belong to the perovskite family, such materials exhibit different physical properties depending on the atoms included in the structure, such as ferroelectricity, piezoelectricity, superconductivity and properties of optoelectronic interest. The ideal perovskite structure appears in the form of ABX_3 , which is schematically illustrated in Figure 2-1. It shows a cubic reticule, where A is the larger cation that occupies the eight angles of the cube, B is a smaller cation occupying the centre of the cube and it's octrahedrally coordinated with an anion X, that therefore lies in the centre of each face. It was proposed in 1923 by Goldschmidt that having the general composition ABX_3 was not sufficient for a solid to be able to arrange effectively into the perovskite structure. In addition to the stoichiometry he postulated the existence of a tolerance factor for the ionic radii r_A , r_B and r_X defined as:

$$t = \frac{r_B + r_X}{\sqrt{2}(r_A + r_B)}.$$

Values of t between 0.1 and 1 allow a stable perovskite structure [3], [4]. A tolerance factor of 1 corresponds to the higher-symmetry cubic phase. Many combinations of different ions, however, result into $t \neq 1$. This results in the structure needing to rearrange to account for the different equilibrium. This fact is subsequently responsible for structural distortions into lower-symmetry structures. Other sources of strain can lead to the formation of structures different from the cubic one. These noticeably are often vibrational motion and chemical bonds. In particular, the vibrational motion is responsible for phase transitions that many perovskites exhibit at different temperatures.

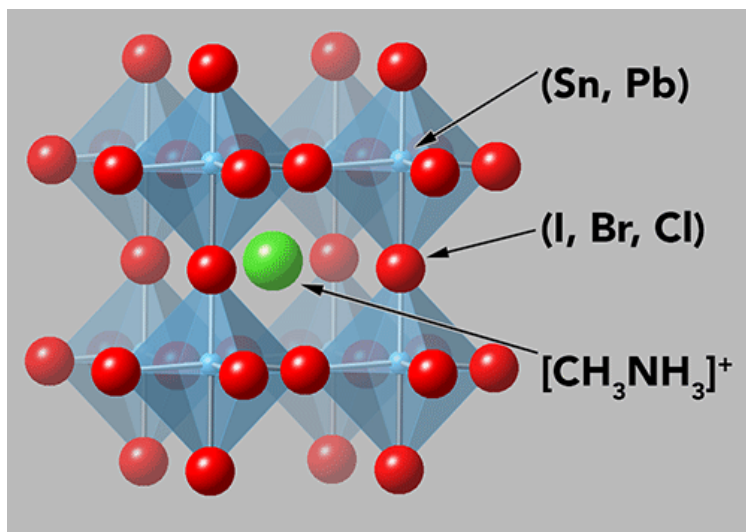


Figure 2-1: Generic cubic perovskite structure of the form ABX_3 . The site A is occupied by one large cation (green sphere). Site B (small blue spheres) and site X (red spheres) are respectively occupied by a metal cation and a halide anion. In the schematic it's possible to observe the octahedra surrounding the lead atom formed by the 6 halide ions. In the crystalline cell charge neutrality is ensured by the balance between positive ions, i.e. A^+ and the 8 B^{2+} cations shared by 8 cells each gives a positive charge of +3, and the negatively charged ions C, i.e. 12 C^- atoms shared each between 4 cells resulting in a neat negative charge of -3.

2.3 Methylammonium Lead Trihalide Perovskites

Organometal halide represents a new generation of the perovskite family where site A is occupied by a large cation, site B is occupied by a metal cation and a single one or a mixture of halide anions are sitting in the position X. A very wide number of different compounds in this class of perovskites show extremely promising properties suitable for optoelectronics applications. The most common combinations present a large organic cation such as methylammonium (CH_3NH_3^+) or formamidinium ($\text{CH}(\text{NH}_2)_2^+$) or alternatively a large inorganic cation as Cs^+ , a post transition metal such as Pb_2^+ and halides such as I^- , Cl^- or Br^- . The possibility to use different atoms or molecules in the crystallographic positions of ABX_3 structure can overcome the problems related to the presence of lead (even if used in small quantities), for example through substitution with Sn.

Methylammonium lead iodide perovskites (MAPI) typically present three phases. Above 315 K they exist in their cubic phase, in the range of temperatures between 315 K and 150 K they rearrange in a tetragonal phase and finally below 150 K they adopt the orthorhombic phase. Experimental evidence points toward the possibility of a coexistence between phases, noticeably the tetragonal and the orthorhombic ones in the range between 140 and 110 K [5]

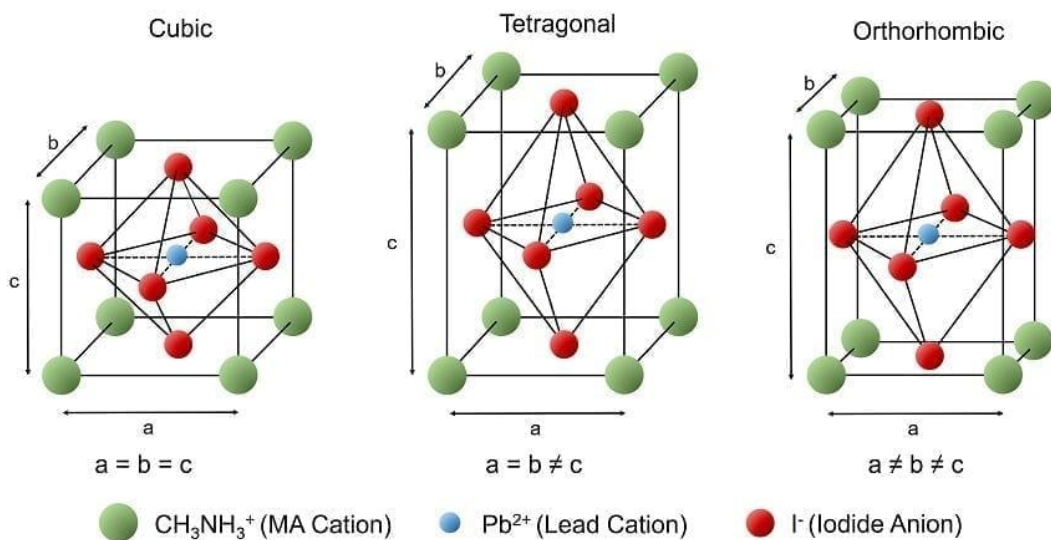


Figure 2-2: Crystalline structures corresponding to MAPI Cubic, Tetragonal and Orthorhombic phases [6].

2.4 Optoelectronics Properties

Organometal halide perovskite have attracted great attention among scientist due to the abundance of many desirable photophysical properties. They exhibit high absorption coefficient and high emission typical for direct band-gap semiconductors [7]. However, they also have slow charge recombination usually observed in phonon assisted transitions in indirect band gap semiconductors [8]. Therefore various models have been proposed to try to account for these observations in terms of trap assisted recombination as the main mechanism for the slowing down of the charge recombination [9]–[11]. The electronic structure of methylammonium lead iodide perovskites appears to be determined primarily by the large metal cation (Pb^{2-}) and the halide ion (I^-). In particular, the valence band (VB) and the conduction band (CB) are formed from π^* and σ^* -antibonding orbitals originating from hybridization of Pb [6s] and I [5p] orbitals. The band formation in this family of perovskites has a deep connection with the positioning of defect and trap states within the energy bands. Figure 2-3 illustrate how vacancies originating from the antibonding orbitals result in shallow intra-band trap states that are located energetically close to the surface of the VB or CB.

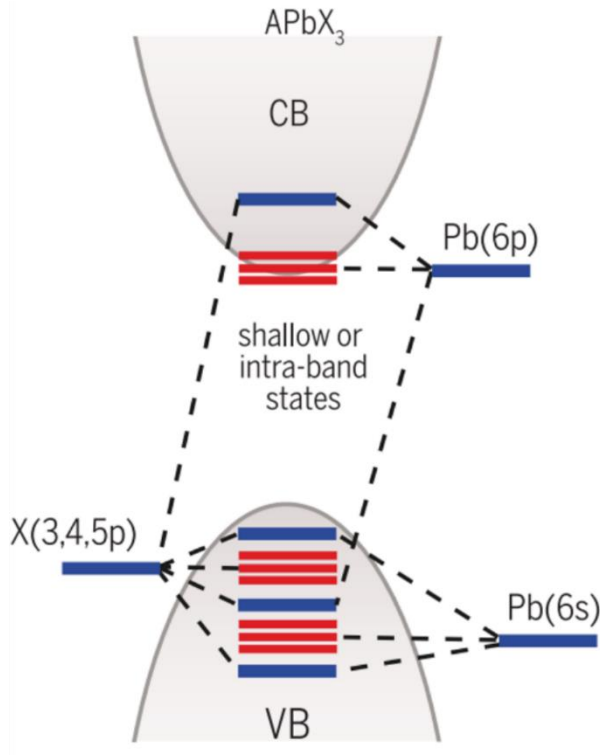


Figure 2-3: Schematic representation of the formation of defect states within VB and CB in $APbX_3$ perovskites Adapted from [12].

Hybrid perovskites possess a wide band gap tunability from the infra-red to the ultra-violet [13], [14] achievable by substitution of the halide anion. An example of this can be seen in Figure 2-4, where the band shifts towards lower energies due to the increasing percentage of Br substituting I in the halide in crystallographic position X.

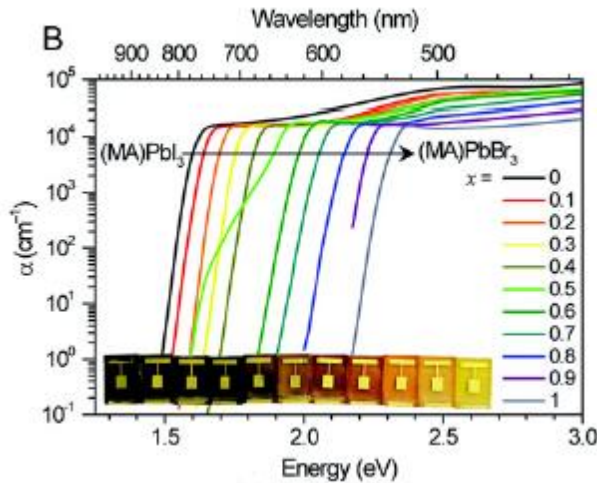


Figure 2-4: Variation of the absorption spectra as a function of the iodide-bromide ratio x in lead mixed halogen perovskites thin films [15]. The figure shows how the band absorption edge is shifted to higher energies as the ratio x is increased from 0 to 1 in $(MA)Pb(I_{1-x}Br_x)_3$.

This can be used to set the bandgap close to the ideal value postulated by the Shockley-Quieser theory and therefore improve the light conversion efficiency or it can be tuned in order to work in tandem with another photovoltaic material [16], [17]. Correlated to this property the possibility to easily control the emission is easily exploitable for LEDs and laser applications. Additionally, they exhibit absorption coefficient of the order of 10^4 - 10^5 cm^{-1} across the visible spectrum, allowing thin layers of few hundreds of nanometres to harvest light efficiently. In Figure 2-5 we report the absorption coefficient versus wavelength of thin films of perovskite $\text{CH}_3\text{NH}_3\text{PbI}_3$ plotted together with the AM 1.5G solar spectrum. It is possible to observe how the overlap between the two curves covers a very good portion of the solar spectrum, therefore indicating the possibility for efficient energy harvesting.

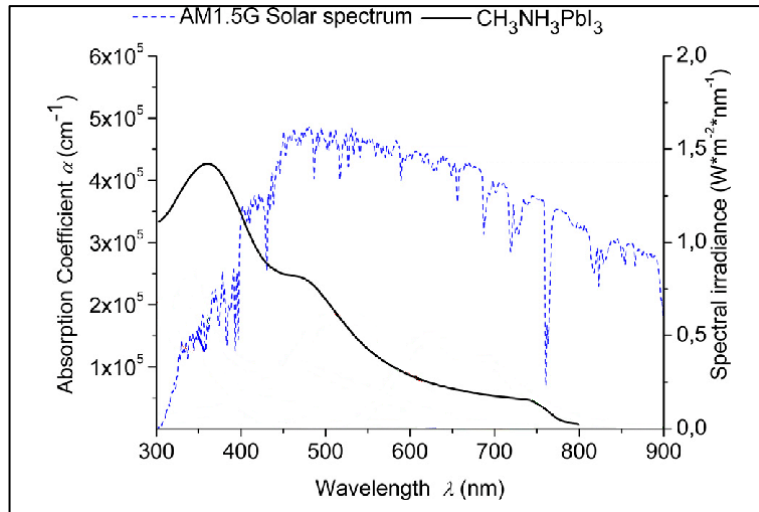


Figure 2-5: Absorption coefficient (α) versus wavelength of thin films of perovskite $\text{CH}_3\text{NH}_3\text{PbI}_3$ plotted together with the AM 1.5G solar spectrum. Adapted from [18].

Efficient carrier collection is supported by their remarkable electrical properties. Many studies have reported very high charge carrier mobilities μ ($> 30 \text{ cm}^2(\text{Vs})^{-1}$) and long lifetimes τ , leading to diffusion lengths L exceeding $1 \mu\text{m}$. For many optoelectronic applications long diffusion length is a very important property because it is related to how far a carrier can travel into the material before recombining radiatively and relates to the probability for the charge to be collected at the electrode and efficiently contribute to the photocurrent of the solar cell. It is useful to remember how carrier mobility and lifetime contribute to the diffusion length [19]:

$$L = \sqrt{\frac{\mu \cdot k_B \cdot T}{r \cdot e}}$$

In this expression μ is the Boltzmann constant, T is the temperature and r is the total recombination rate which is inversely proportional to the lifetime. Therefore, high carrier mobility and long lifetime are highly desirable properties for the efficient application of perovskites as a light harvesting medium.

Chapter 3 **Experimental Techniques**

3.1 **Introduction**

In order to obtain insight into the optoelectronics properties of MAPbX_3 perovskites, we performed a series of optical spectroscopy experiments. The main technique used was photoluminescence spectroscopy, where the light emitted by the photoexcited material is analysed spectrally and temporally. The information carried by the emitted photons were then analysed and combined in order to construct a model of the emission mechanism in the material, accounting for the nature of the photo-generated species and their dynamics, including relaxation rates and radiative and non-radiative decay paths. Further support for this fundamental data came from linear absorption spectroscopy, reflectance measurements, and PL imaging.

3.2 **Time Resolved Photoluminescence**

Fluorescence is generally divided in two main groups: steady-state (ssPL) or time-integrated photoluminescence (TIPL) and time-resolved photoluminescence (TRPL). Steady state regimes can be stimulated with a continuous light source and, because of the nanosecond timescale of the fluorescence, it is achieved practically immediately. Using different instruments, it is then possible to record the intensity of the emitted light or to resolve it spectrally. When the sample is illuminated with a pulse of light that is extremely short when compared to the PL lifetime, the intensity decay can be recorded with a high-speed detection system. This allows us to extract direct information about recombination processes, recombination rates, and lifetimes.

3.2.1 **Ultrafast Time-Resolved and Steady-State PL setup**

Spectroscopy measurements were performed using a fully automatized confocal setup, controlled by a LabVIEW interface, which has been developed to allow for control of the wavelength, repetition rate and power of the excitation, the detection

wavelength range, and the sample temperature. Figure 3-1 provides a schematic representation of this setup. The optical excitation is provided by the part of the setup highlighted with green colour. A tuneable titanium:sapphire laser (Coherent Chameleon Ultra II), is able to generate femtosecond light pulses at a repetition rate of 80 MHz in a spectral range between 680 and 1080 nm. An optical parametric oscillator (OPO) and a second harmonics generator (SHG) extend the final range limits to 3500 and 340 nm respectively, completing the excitation wavelength tunability. A pulse picker is used to modulate the repetition rate, thereby lowering the pulses frequency down to 1 kHz. The beam is then directed to the fully enclosed optical setup. In the section of the setup preponed to modulate the excitation density (highlighted in blue in Figure 3-1), a sequence of motorized ND filters and a half-wave plate combined with a linear polarizer control the excitation beam power; the polarization of the beam is rotated through the half-wave plate, changing the proportion between vertical and horizontal polarization, the latter is then filtered by the polarizer, finely modulating the beam power. A beam splitter sends 5% of the beam to a power meter connected to the monitoring LabVIEW software for real-time monitoring of the excitation power and registration of the beam stability during the measurements. At this point a dichroic mirror is used to direct the beam towards the last part of the setup (yellow highlight), where the excitation of the sample and the collection of the PL are achieved. A microscope objective lens which focuses the excitation laser onto the sample. The sample can be alternatively mounted on a 3D translational stage or inside a close-loop He cryostat. A CMOS camera observes the position, the shape, and the size of the excitation spot on the sample. The temperature of the sample is controlled through an Oxford Instruments ITC503 unit connected to the setup software interface. The photoluminescence generated by the laser pulses are subsequently collected through the objective and directed towards an avalanche photodiode (APD) detector connected to a time-correlated single photon counting (TCSPC) Becker & Hickl GmbH SP-140 card, which time resolves the measurements with a 40 ps resolution. In addition, it is possible to select a specific spectral window of the emission, using a Bentham M300 single monochromator.

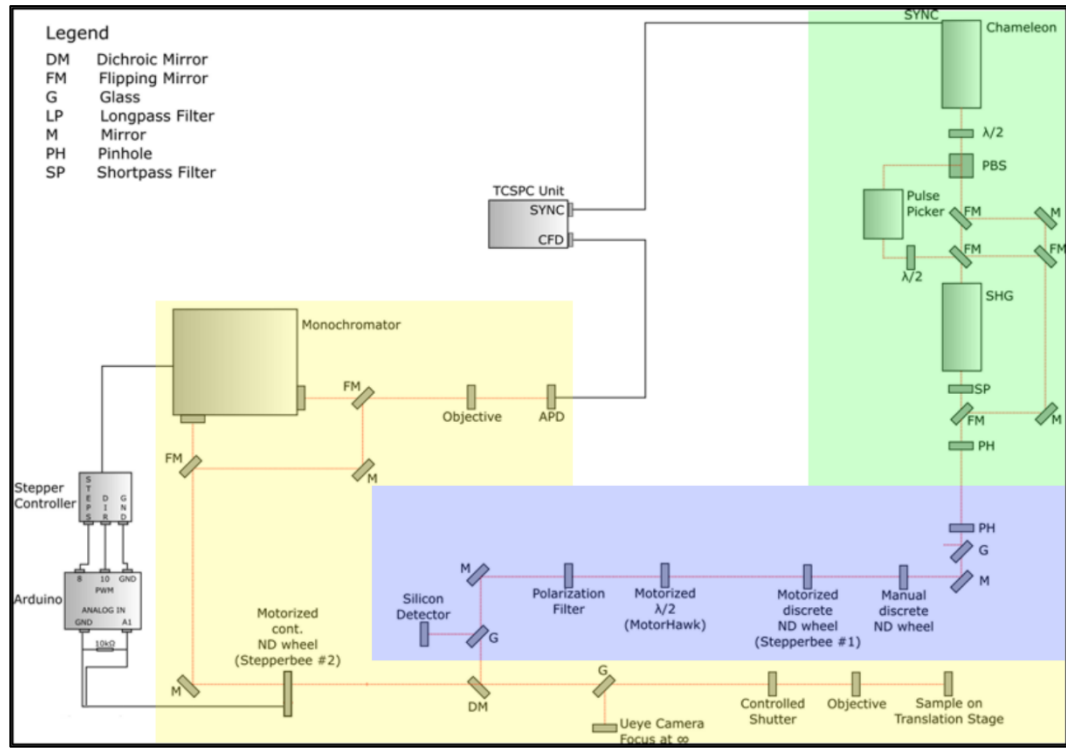


Figure 3-1: Schematic depiction of the automated power-dependent time-resolved spectroscopy setup. Excitation is provided by a tunable Titanium:Sapphire laser (green highlighted section) and is routed through motorized optics to the sample (blue highlighted section). The photoluminescence signal is collected and directed towards an avalanche photodiode connected to time-correlated single photon counting (TCSPC) electronics (yellow highlighted sections).

3.3 Linear Absorption Spectroscopy

Linear absorption measurements were performed using a combination of transmittance and reflectance experiments. The absorption coefficient was obtained from the relative change in transmission of light provided by a wide spectrum Thorlabs white light source collected in an integrating sphere and spectrally resolved with an Ocean Optics USB spectrometer. A reference measurement for the sample was obtained by first measuring the light transmitted by the substrate on which the perovskite film was successively deposited. Figure 3-2 shows the light beam of intensity I_0 that from the light source goes through the sample.

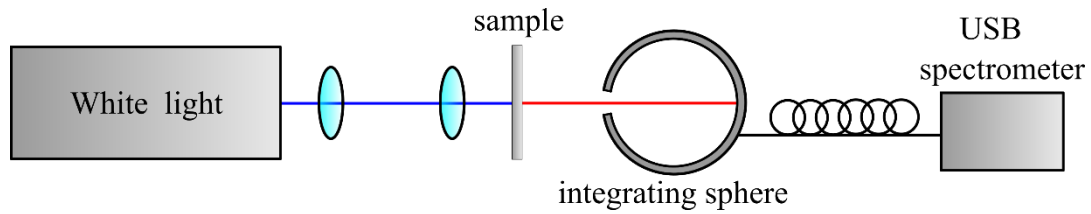


Figure 3-2: Schematics representing the setup for transmittance measurements.

Hereby, the intensity will be reduced to a value I accordingly to the Beer-Lambert law. Given that the sample thickness l is sufficiently large to provide a detectable change in the spectral transmission but yet sufficiently low to permit enough transmission, it's possible to neglect the scattered component of the transmitted signal. A further correction comes from the consideration of the reflectance spectrum. The percentage of light reflected by the sample was measured using the experimental configuration depicted in Figure 3-3.

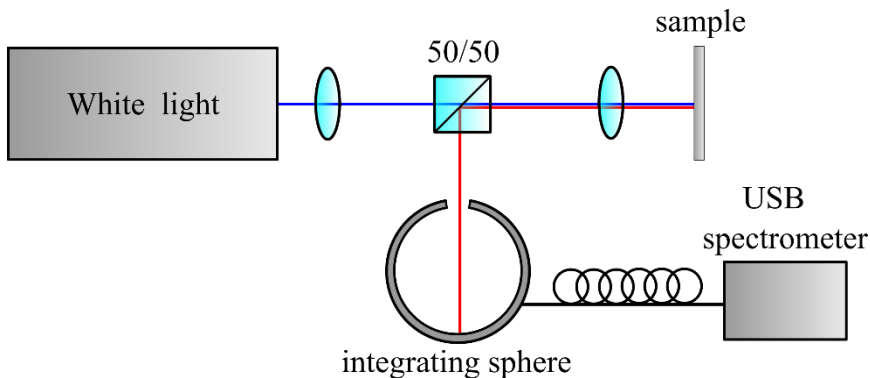


Figure 3-3: Schematics representing the setup for reflectance measurements.

A reference measurement was again performed in the substrate only. After correcting the transmittance with this last measurement, the absorption coefficient α was calculated using the following expression [20]:

$$\alpha = \frac{OD}{0.434 \cdot l} \quad 3-1$$

where OD represents the optical density, obtained by calculating the base-10 logarithm of the transmittance. Temperature dependence of the absorption was measured by placing the sample inside a close-loop He cryostat.

3.4 Sample Preparation

Hybrid organic-inorganic lead halide perovskites films can be prepared by deposition of a solution containing the precursors salts. This deposition leads to the perovskite crystallization on the surface of the substrate.

The preparation of the solution involved a series of steps. First commercially available methylammonium iodide (MAI):PbI₂:PbCl₂ salts were weighted in a molar ratio 4:1:1. Then these salts were diluted on a vial by the addition of dimethylformamide (DMF) with a weight ratio of 45 wt %. Subsequently, this solution was heated at 70°C for an hour and stirred with magnetic bars to facilitate dilution. DMF was additionally added until a reduction of the original solution to 40 % wt is obtained.

Substrates were prepared before the deposition procedure. Glass slides were cut into opportune dimensions and cleaned by 10 minutes sonication in a solution of deionised water and Hellmanex III from Hellma Analytics. A second sonication was performed for an additional 10 minutes in isopropanol, after the substrates have been rinsed with deionised water for two times. Finally, the substrates are dried and transferred on a hotplate at 120 °C for 30 minutes in a nitrogen atmosphere, ensuring all the remaining water to be evaporated before letting the substrates cool down to room temperature.

The final solution obtained as described above was then deposited on the clean substrates by spin coating in a nitrogen atmosphere. The “one step” dynamic casting method was used. This consists in the dynamical dispensation of the solution containing the precursor materials on the glass substrate spinning at 4000 RPM for 30 s. Since the final thickness l of the film, given the solution concentration c , its viscosity η and the angular speed ω , can be evaluated as [21]:

$$l = \frac{c\eta}{\sqrt{\omega}}. \quad 3-2$$

This allowed us to control the film thickness to ~ 300 nm. Finally, upon evaporation of the solvents, the solid precursors precipitate to form a bulk polycrystalline film. The films are finally annealed on a hotplate at 80 °C in nitrogen atmosphere for 2

hours. Conversion between the perovskite tetragonal and cubic phases can occur during the formation or the annealing of the film, leading to the formation of intermediate phases [22]. As we reported in Section 2.3 methylammonium lead iodide perovskites present three crystalline phases depending on the temperature. This conversion between the two phases occurs because in the annealing process the film is heated above the phase transition temperature between tetragonal and orthorhombic phase corresponding to approximately 315K.

3.5 Numerical integration of differential equations

Let's consider a system of N-coupled ordinary differential equations (ODEs) of the form:

$$\frac{d\vec{x}}{dt} = f(\vec{x}, t) \quad (3-3)$$

where $\vec{x}(t) = (x_1(t), x_2(t), \dots, x_N(t))$ and $f(\vec{x}, t) = (f_1(\vec{x}, t), f_2(\vec{x}, t), \dots, f_N(\vec{x}, t))$ with initial condition $\vec{x}(t_0) = \vec{x}_0$. This system of equation has analytical solution only in particular cases, depending on the form of the equation, but can generally not be solved analytically, therefore requiring computational methods. Integrating both side of equation 3-1 gives

$$\vec{x}(t) = \vec{x}_0 + \int_{t_0}^t f(\vec{x}, t) dt \quad (3-4)$$

There exists a multitude of different algorithms to numerically evaluate the integral on the right-hand-sight of equation 3-2, but the general method is the same: the integral is split into many small steps of size ϵ ($\epsilon \ll 1$) and the dynamics of $\vec{x}(t)$ is evaluated iteratively, starting from the initial condition \vec{x}_0 . Hereby, the accumulated error due to discretization into a finite amount of time steps (t_0, t_1, \dots, t) scales with the step-size ϵ . A smaller step ϵ increases accuracy but increases the computation time as well. The simplest method is the *Euler method*, in which the discrete steps for $n > 0$ are explicitly given by

$$\vec{x}(t_n) = \vec{x}(t_{n-1}) + \epsilon \cdot f(\vec{x}(t_{n-1}), t_{n-1}), \quad t_n = t_{n-1} + \epsilon \quad (3-5)$$

However, there exists more complex techniques that generally have a smaller local truncation error (error evaluated in each step due to the finite step-size ϵ) than the Euler method. Coupled ODEs in this thesis have been solved using the *IntegrateODE*-function of the software tool IGOR Pro [23], which uses a 5th-order Runge-Kutta-Fehlberg method for numerical integration. The method does not use a fixed step-size ϵ in each iteration but reduces it if the local truncation error becomes too large. The continuous adaption of step size saves computation time as well as guarantees accuracy in numerical computation. The algorithm is presented in reference [24]

Chapter 4 **Exciton Binding Energy**

4.1 **Introduction**

Upon illumination, a light harvesting material exhibits excitation of electrons from the valence band to the conduction band, leaving unoccupied electronic states of opposite charge behind known as holes. This process, discovered in 1839 by Alexandre Becquerel, is known as photovoltaic effect. The overall process can be summarised in two steps. The first one is the absorption of an incident photon; the photon energy is hence transferred to an electron that is excited to a higher energy state. This is therefore correspondent to the conversion of the photon into an electron-hole pair or exciton. The second step is the separation of excitons into free electrons and holes. These excited electrons and holes, when subject to an electric field, can propagate through the periodic potential of the crystal lattice, and therefore can be collected at the electrodes of a solar cell and contribute to the photocurrent. Nevertheless, being charged particles, electron and hole interact via Coulomb interaction and can form a bound electron-hole state known as exciton. The exciton can then be considered as a neutral quasiparticle having a lower energy than its unbound constituents. The difference in energy between the unbound and bound states is defined as exciton binding energy, E_b , and corresponds to the ionization level of the lowest state of the quasi-particle. The nature of the excitons present in a material is related to the electronic properties of the material itself and can be described within two general frameworks. Bound states in organic molecular semiconductors are usually best described as Frenkel excitons, that are spatially localized and have high binding energies (hundreds of meV). On the other hand, excitations in typical inorganic semiconductors can be portrayed in the framework of the Wannier-Mott model, where hydrogen like species are more delocalised and have a lower binding energy, i.e. in the range of few meV. Since the exciton binding energy is related to the ionization energy of the quasi-particle, materials with larger binding energy will have a higher tendency to form excitons (bound electron-hole states) rather than free charges upon photoexcitation. The opposite holds true for materials with smaller binding energies. Low exciton binding energy is therefore a

Exciton Binding Energy

well desired property for photovoltaic devices since in operational conditions thermal energies at room or higher temperatures (>25.7 meV) may be sufficient to dissociate the excitons into free charges that can be collected. As described in detail in Section 4.4, the relative densities of bound and unbound charges as a function of temperature and binding energy generated after photoexcitation are dictated by the Saha law.

The value for the exciton binding energy in lead-halide perovskites has been widely explored. To date it seem that it lays in a range comprised between few meV and >60 meV [25], and therefore excitons in MAPI perovskites could be described in the Wannier-Mott model. The wide range of values obtained depends on several different aspects. First the exciton binding energy has been found to present a dependence on the temperature [26]. The temperature also influences the crystal phase of the material as well as the dielectric function. Additionally, a multitude of morphological and material variations have been investigated by multiple groups resulting in the observation of a plethora of different optical properties. Various techniques have been used to study the value of the exciton binding energy. Magnetoabsorption spectroscopy at low temperature (4-2K) was applied to obtain the values of 37 meV [27] and 50 meV [28] for the orthorhombic phase, but later studies suggested variations on the magnitude of the predicted values of the dielectric function used in the calculations, resulting in a binding energy E_b of 2 meV [29], showing the need for different approaches. Another series of studies were conducted on the temperature dependence of the emitted luminescence. In these works the observed decrease of PL intensity with increasing temperature was associated to exciton dissociation, and resulting in binding energies of 19 meV [30], 32 meV [31] and 62 meV [32]. The relation between exciton dissociation and PL quenching it has however been debated, especially because the complexity of the radiative efficiency does not seem to be fully described with such models. A third group of studies focused on the analysis of the absorption spectra near the band edge. These resulted again in different values for different temperatures ranges, and are comprised between 5 and 25 meV for the tetragonal phase and 15 and 30 meV for the lower temperature phase [33]–[37]. One of the advantages of this method

derives from the possibility to extract a function of E_b over the temperature T while still accounting for phase transitions.

From the considerations above we can understand how knowing the nature of the electron-hole interaction, and in particular the value of the exciton binding energy as a function of temperature, plays a very important role in the determination of the nature and the number of particles generated in MAPI films upon photoexcitation. This knowledge is then a necessary foundation for building a kinetic model for recombination dynamics that takes into consideration both exciton and electron-hole pair recombination processes. Therefore, in this chapter we will first introduce the Elliott theory of near band edge absorption, then we will use this model to determine the value of the exciton binding energy as a function of temperature from absorption measurements. In the second part of the chapter we will use the extracted values of E_b together with the Saha equation in order to calculate the densities of free and bound charges as a function of temperature and incident excitation fluence.

4.2 Exciton Binding Energy from Absorption Measurements

As seen in the introduction to this chapter, one method used to extract the exciton binding energy is to study the optical absorption near the material's band gap energy. As mentioned in section 2.4, the band structure of methylammonium lead iodide perovskite presents a direct band-gap between the CB and the VB, leading to direct recombination between electrons and holes. To do this analysis we will be using Elliott's theory of band onset absorption in direct bandgap semiconductors to model the near band-edge optical absorbance data over the experimental temperature range [38]. By fitting this description to absorption data, one can extract the exciton binding energy and electronic bandgap.

4.2.1 Elliott's Theory

Elliott's theory describes the intensity of optical absorption of semiconductors near the band-edge. According to the model, the absorption coefficient is given by

Exciton Binding Energy

$$\alpha(E) = \frac{A}{E} \left(\sum_{n=1}^{\infty} \frac{4\pi E_B^{\frac{3}{2}}}{n^3} \delta\left(E - \left(E_G - \frac{E_B}{n^2}\right)\right) + \frac{2\pi \sqrt{\frac{E_B}{E-E_G}}}{1 - \exp(-2\pi \sqrt{\frac{E_B}{E-E_G}})} \theta(\sqrt{E-E_G}) \right) \quad (4-1)$$

where E is the photon energy, A is a scaling factor that accounts for the transition dipole moment $\langle \psi_v | q\mathbf{r} | \psi_c \rangle^2$, E_b is the exciton binding energy and E_g is the bandgap energy. The theory encompasses the contribution of absorption of photons by both exciton states within the bandgap, and also via band-to-band transitions. The former is characterised by a series of delta functions due to the discrete nature of exciton transitions. The band-to-band (free-carrier) absorption is described by a step function, proportional the square root of the photon energy for all real values of $\sqrt{E - E_g}$ and zero elsewhere.

The scaling factor A is chosen as a constant for all temperatures. E_B and E_G are varied with temperature, where necessary. Equation 4-1 is convolved with a lognormal distribution centred at the origin, i. e.

$$f(E, \sigma, \theta, \mu) = \frac{1}{\sigma \sqrt{2\pi}} \frac{1}{E-\theta} \exp\left(\frac{-\left(\ln\left(\frac{E-\theta}{\mu}\right)\right)^2}{2\sigma^2}\right) \quad (4-2)$$

where σ is the shape parameter that accounts for the low energy tail introduced by structural disorder and μ is the broadening parameter, representing temperature-dependent electron-phonon coupling. Hence, σ is chosen as a constant for the range of temperatures for the tetragonal phase and μ is varied for each temperature.

The data were initially modelled for temperatures above the phase transition (> 140 K), where the material is assumed to be relatively phase pure, in order to have a more precise fit of the scaling factor, that is then used across the whole temperature range.

4.2.2 Results and discussion

Transmission and reflectance spectra are measured for $\text{CH}_3\text{NH}_3\text{PbI}_3$ thin-films. The films were fabricated following the method described in Section 3.4 and the reflectance and transmittance measurements were performed according to the procedures described in Section 3.3.

In Figure 4-1 we show the temperature dependence of the spectra measured transmission geometry. The shapes of the transmission spectra are similar to the ones previously observed for this material [39], [40]. The absorption edge exhibits a redshift with decreasing temperature in the range between room temperature and 140 K. We identified this range to correspond to the tetragonal phase of MAPI. Around $T = 136$ K it is possible to observe a discontinuity in the absorption edge leading to a strong blueshift. We identify this discontinuity as the phase transition between the tetragonal and orthorhombic crystal structure. In the lower part of the temperature range we observed a broader absorption edge and the presence of a more visible shoulder at higher energy (corresponding to shorter wavelength). We additionally show in Figure 4-1 the integrated PL emission as a function of the temperature. We notice at this point the fact that the temperature dependence of the centre of the emission peak appears to follow the same behaviour as the band edge.

Exciton Binding Energy

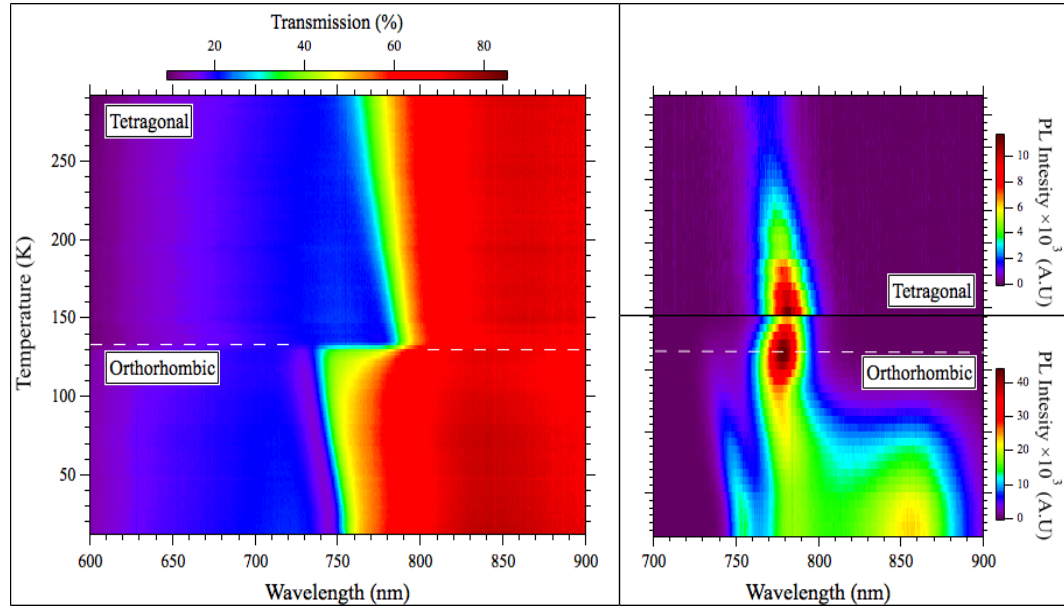


Figure 4-1: Transmission of the MAPI thin-film versus temperature. Steady-state PL of the tetragonal phase a) and orthorhombic phase b) MAPI versus temperature. The white dashed line indicates the phase transition. The maximum PL observed across the whole temperature range corresponds to the phase transition.

This data, along with the thickness of the film is used to calculate the absorption coefficient using the relation:

$$\alpha(E) = \frac{1}{d} \log_{10} \left(\frac{(1-R(E))^2}{T(E)} \right), \quad (4-3)$$

where d is the thickness of the film, and $R(E)$ and $T(E)$ are the reflectance and transmission spectra respectively.

The data obtained at 290 K display a smooth absorption onset around 1.55-1.65 eV, which is the expected optical bandgap for $\text{CH}_3\text{NH}_3\text{PbI}_3$ (Figure 4-2 a). At this temperature, the absorption reduces exponentially with decreasing photon energy. A long tail at lower energies compared to the band edge is attributed to the electron-phonon coupling term that introduces a broadening of the band edge inset and the exciton transitions as well. In the model this is represented by the log normal distribution in Eq. 4-2. As the temperature is reduced, a peak in absorption close to the band-edge emerges, indicative of exciton transitions (Figure 4-2 b). The peak

becomes narrower and more intense relative to the free-carrier absorption, following a decrease homogenous broadening caused by electron-phonon coupling. In the model, this is characterised by the broadening parameter μ , which increases with temperature.

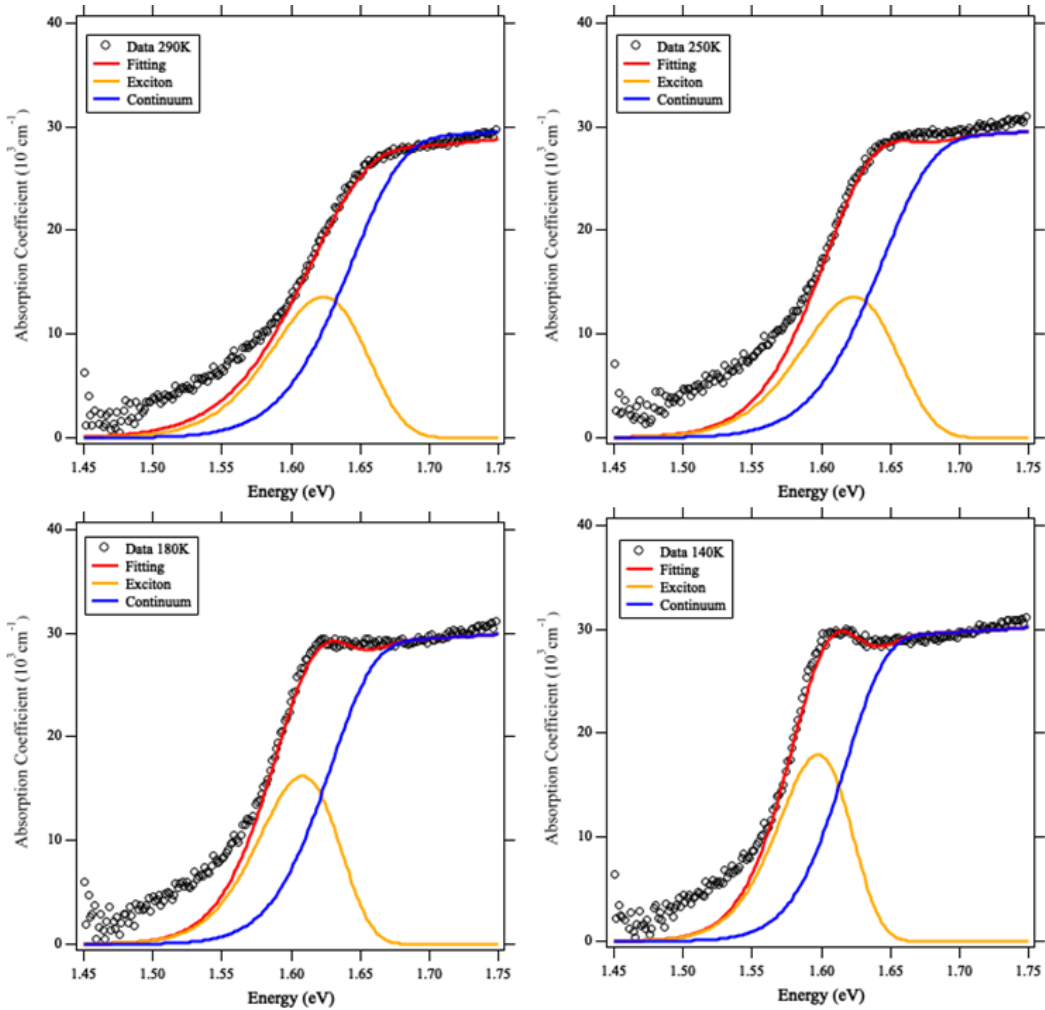


Figure 4-2: Absorption coefficient versus photon energy obtained for MAPI thin films at different temperatures for the tetragonal phase. Results from the model follow the data closely at energies close to the band-edge. The total absorption is the sum of the contribution from both exciton transitions and excitations of free carriers in to the conduction band.

Exciton Binding Energy

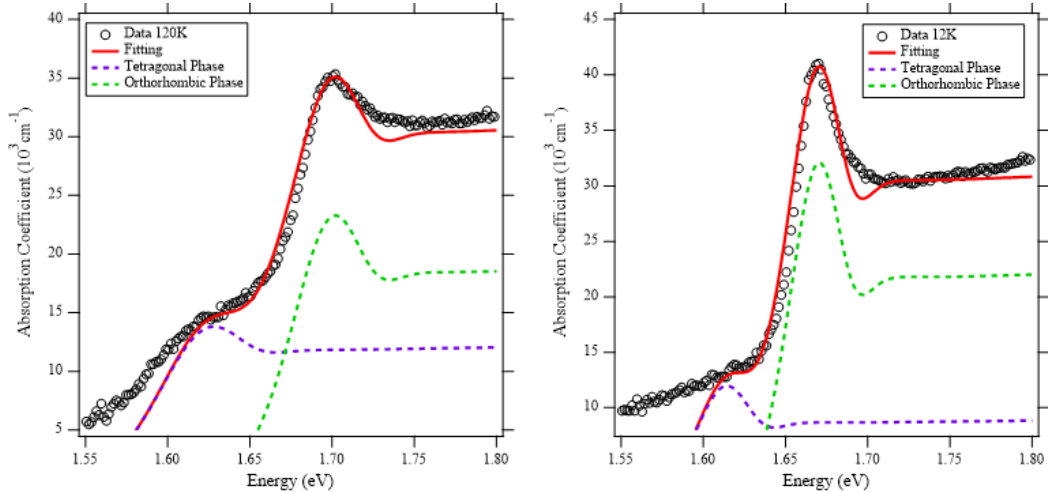


Figure 4-3: Absorption coefficient versus photon energy obtained for MAPI thin films at different temperatures for the orthorhombic phase. Results from the model follow the data closely at energies close to the band-edge. The total absorption is the sum of the contribution from both exciton transitions and excitations of free carriers into the conduction band from both the tetragonal and orthorhombic phase, that coexist for $T < 140\text{K}$.

The bandgap is found to increase linearly with temperature, also in agreement with prior work [40], [41]. This is not typical of commonly studied semiconductors (Ge, Si, GaAs) that follow the opposite trend [26]. Previous theoretical work has indicated that this is due to the stabilisation of band-edge states, following thermal expansion of the lattice [42]. A value of 20 meV is obtained for exciton binding energy across the whole tetragonal phase, which is consistent with several values previously found from the fitting of Elliott theory to absorption data [35], [36]. This value is constant across the temperature range of the tetragonal phase, except for 290 K where it is found to decrease slightly. Regardless of the use of a lognormal distribution to account for the inhomogeneity of the broadening, the low energy tail is not completely reproduced across the temperature range of the tetragonal phase. This may due to a temperature dependence of the disorder or the presence of deep intra-gap states. Below the phase transition the orthorhombic phase is observed, which exhibits a constant binding energy of 23.3 meV. The results of the Elliott's fit are reported in Figure 4-4

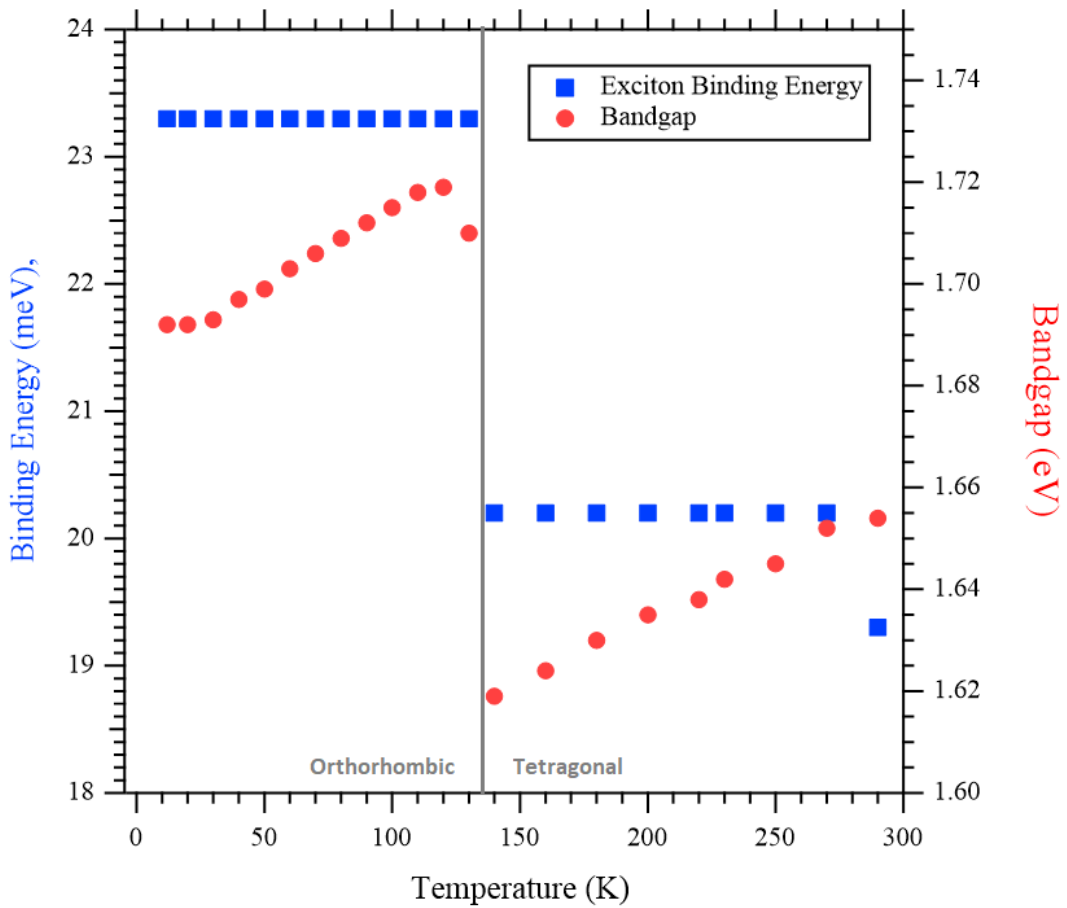


Figure 4-4: Temperature dependent results for band gap and exciton binding energy from the Elliott's theory modelling. The bandgap and broadening parameter increase with temperature, whereas the binding energy is almost constant. The discontinuity in the band gap values and exciton energies at T=140K are a result of the transition between orthorhombic and tetragonal phase.

4.3 Urbach Energy

An exponentially decreasing absorption with decreasing photon energy is typical of materials that display temperature-induced disorder or strong internal fields, caused by ionised defects for example [43]. To characterise the exponential tail, the following equation is fitted in the exponential region of the data:

Exciton Binding Energy

$$\alpha(E) = \alpha_0 \exp\left(\frac{E-E_0}{E_U}\right) \quad (4-4)$$

where E_U is termed the bandtail width or Urbach energy [44]. Figure 4-5 displays the absorption coefficient α on a logarithmic scale versus photon energy for various temperatures. The absorption quite clearly follows an exponential trend, as shown by the linear fitting for $\ln(\alpha)$. The Urbach energy is found to be 70.5 meV at 290 K, which is approximately $3k_B T$. This value is relatively high compared to previously reported results, in which an Urbach energy as low as 15 meV was obtained for the same material [45]. The Urbach energy decreases with temperature as expected and remains close to $3k_b T$. Below 200 K, the absorption begins to deviate from an exponential behaviour.

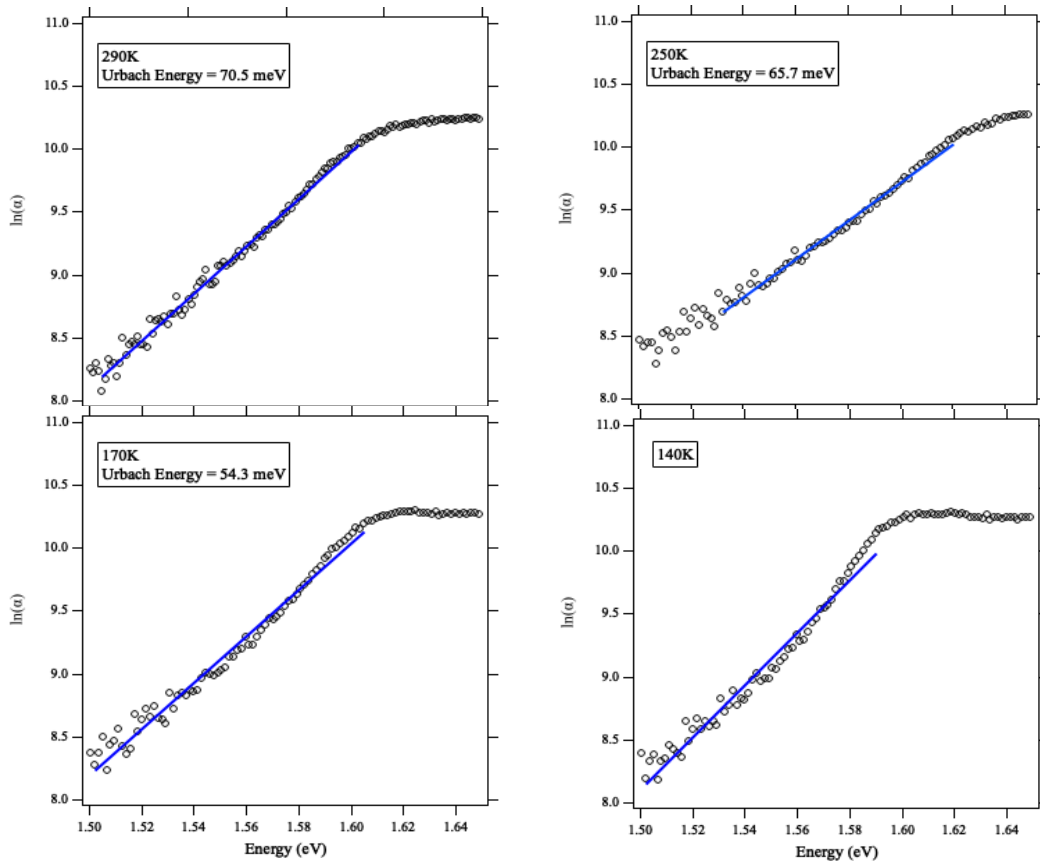


Figure 4-5: $\ln(\alpha)$ versus photon energies less than the bandgap for different temperatures. The absorption shows an exponential behaviour for temperatures above 200K, below which it begins to deviate from exponential. The value obtained for the Urbach energy is approximately $3k_b T$.

4.4 Excitons vs Free carriers

Since the early stages of research on the optoelectronic properties of MAPbX_3 perovskites, many investigations have aimed to establish whether the dominant photogenerated species are excitons or free carriers [28], [32], [33], [46], [47]. This is of particular importance for the design and functionality of devices like photovoltaic cells because of the Coulomb correlation that exists between electrons and holes. This relationship results in a bound state (exciton) with binding energy E_b and this represents an additional barrier before the electrons and holes can contribute to the photocurrent [25]. Initial studies explained the observed properties in terms of excitons, with these models corroborated by the observation of a very strong absorption that was close to the band-edge and with evident excitonic features and emission occurring near to the excitonic resonance [32]. However, more recent works on solution processed perovskites thin films have radically overturned initial interpretations [48]–[51]. Consequently, free electron-hole dynamics have been successfully used to describe absorption and emission processes, especially at room temperatures [33].

4.4.1 Saha equation theory

Photoexcitation in a semiconductor results in the promotion of a density of N photo-generated electrons per cubic centimetre into the conduction band which results in the consequent creation of an equal density of holes in the valence band. This scenario can be considered as a gas of electrons and holes at a certain temperature T where charges interact to form a thermodynamic equilibrium between bound excitons having binding energy E_b and unbound electron-hole pairs, resulting in balanced final concentrations for electrons, holes and excitons respectively denoted as n , h and x . Due to the nature of the photo-generation, the total density N determines the densities n and x as

$$N = n + x. \quad (4-5)$$

The entropy S of this system can be written as:

Exciton Binding Energy

$$S = k_B \cdot \left\{ - \left[n \cdot \ln \left(\frac{n}{M_e} \right) \right] - \left[n_h \cdot \ln \left(\frac{h}{M_h} \right) \right] - \left[n_x \cdot \ln \left(\frac{x}{M_x} \right) \right] + n + h + x \right\}, \quad (4-6)$$

where M_e , M_h and M_x are the concentrations of available states for electrons holes and excitons respectively. The volume v occupied by each particle is proportional to M^{-1} and also to λ^3 , where λ is the thermal wavelength defined as $\frac{h}{\sqrt{2\pi m k_B T}}$. Then, we can write the total free energy G as:

$$G = nE_g + [x \cdot (E_g - E_b)] + [k_B T \cdot x \cdot \ln(x \cdot v_x)] + [k_B T \cdot x \cdot \ln(n \cdot v_e)] + [k_B T \cdot h \cdot \ln(h \cdot v_h)] - [k_B T \cdot (n + h + x)]. \quad (4-7)$$

Intraband trap states can cause the presence of a doped hole concentration n_T that sums with the photo-generated holes, so that it is possible to express the hole density as a function of the total excitation density and the trap states density:

$$h = n_T + n = N - x + n_T \quad (4-8)$$

$$G = (N - x)E_g + x \cdot (E_g - E_b) + k_B T \cdot x \cdot \ln(x \cdot v_x) + k_B T \cdot (N - x) \cdot \ln((N - x) \cdot v_e) + k_B T \cdot (N - x + n_T) \cdot \ln((N - x + n_T) \cdot v_h) - k_B T \cdot (2N - x + n_T). \quad (4-9)$$

By finding the minimum for G as a function of the exciton concentration as required by thermal equilibrium, it is possible to obtain an implicit equation for x :

$$-\frac{E_b}{k_B T} + \ln \left[\frac{x \cdot v_x}{(N - x + n_T) \cdot (N - x) \cdot v_h v_e} \right] = 0, \quad (4-10)$$

Solving for x and defining:

$$A = \frac{v_x}{v_e v_h} e^{\left(-\frac{E_b}{k_B T} \right)}, \quad (4-11)$$

the equation takes the form:

$$(N - x + n_T) \cdot (N - n_x) - An_x = 0 . \quad (4-12)$$

And using the expression for the total photo-generated carriers N it is finally possible to write the generalization of the Saha equation of p-doped semiconductors [52], [53]:

$$(n + n_T) \cdot n = Ax . \quad (4-13)$$

If the density of trap states is zero, this expression reduces to the canonical form of the Saha equation:

$$A \cdot x = n^2 . \quad (4-14)$$

4.4.2 Exciton and free-carriers as a function of N, E_b, T and trap density

Concentrations of holes, electrons and excitons were calculated using the Saha equation across a temperature range from 0 to 290K and applying different exciton binding energies and different initial excitation and traps densities.

The first experiment used an initial trap density equal to zero, corresponding to the simpler formulation of the Saha equation. In this scenario the concentrations of holes and electrons are always equal. For this first calculation an exciton binding energy of 10meV has been assumed to determine electron and exciton densities across the temperature range previously stated for three different excitation densities: $1 \cdot 10^{14}$, $1 \cdot 10^{15}$ and $1 \cdot 10^{16} \text{ cm}^{-3}$.

Exciton Binding Energy

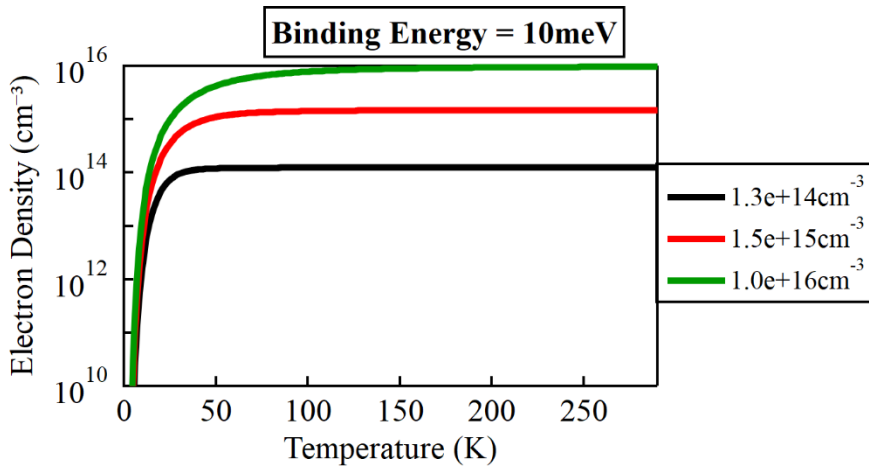


Figure 4-6: Electron densities as a function of T for different excitation densities at fixed exciton binding energy.

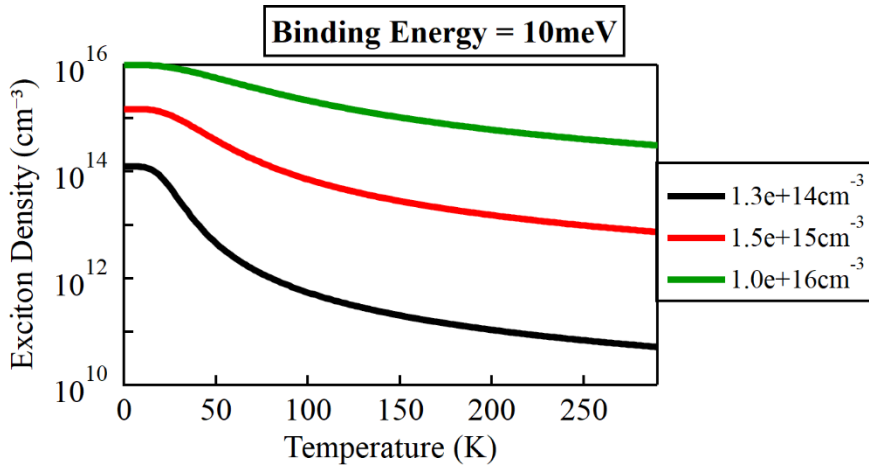


Figure 4-7: Excitons densities as a function of T for different excitation densities at fixed exciton binding energy.

Figure 4-6 shows how the electron density is a monotonically increasing function of temperature, which tends to the value of the initial excitation density at high temperature when the thermal energy is high enough to efficiently dissociate all the excitons. On the other hand, as shown in Figure 4-7, the concentration of the excitons at low temperature is very close to the excitation density as the binding energy is much higher than the thermal energy. As the temperature is increased, as expected, their density decreases monotonically.

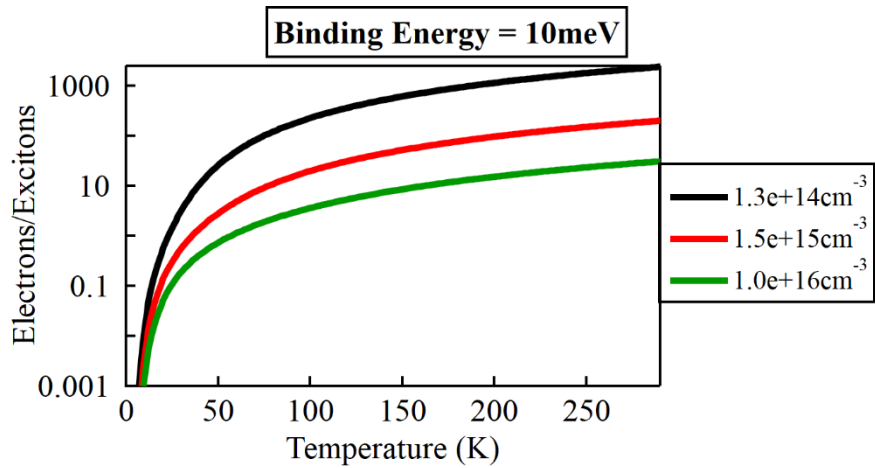


Figure 4-8: Ratio between electron and exciton densities as a function of T for different excitation density at fixed exciton binding energy.

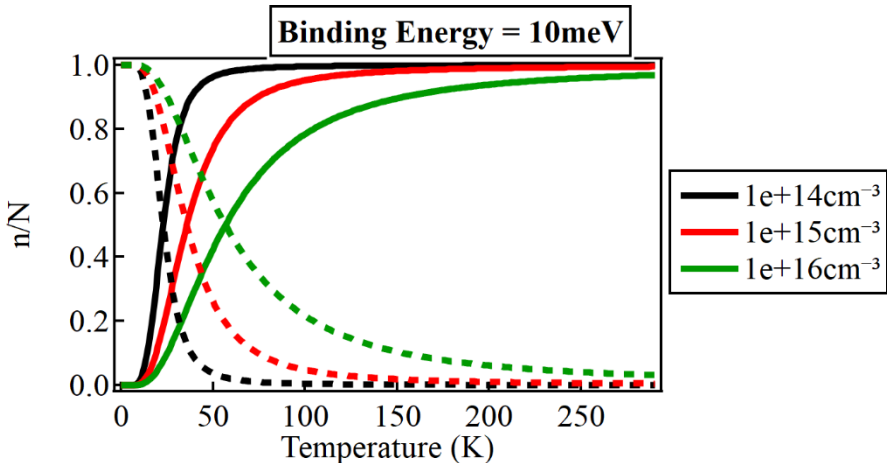


Figure 4-9: Fraction of electrons and excitons over the total photo-generated charges as a function of T for different excitation density at fixed exciton binding energy. Solid (dashed) lines represent the electron (exciton) population over the total population.

The ratio between free electrons and excitons trivially increases with temperature for any given excitation density. One remarkable aspect is that this ratio is heavily dependent on the initial excitation density. As shown in Figure 4-8, the lower excitation density (black curve) presents a relatively higher number of electrons compared to the higher densities (red and green respectively). This simple fact implies that the dominant species observed during a photoluminescence experiment depends on the injected carrier density rather than just on the temperature of the

Exciton Binding Energy

sample. In the example in Figure 4-8, assuming $E_b=10$ meV and $T = 50$ K, it is possible to observe how for $N = 1 \cdot 10^{14} cm^{-3}$ the ratio between electrons and excitons is above 10, indicating that free carriers dominate the decay. Given the same E_b and T but $N = 1 \cdot 10^{16} cm^{-3}$ the ratio is close to 0.1 indicating that the dominant species become excitons and that the observed decay will be exciton driven. This is of particular importance in these temperature ranges where the concentrations of the two species are closer. In these conditions one can expect the observed dynamic to be equally influenced by both free charges and excitons, therefore no species is dominant. Plotting the percentage of free electrons and excitons over N (Figure 4-9) highlights how it's possible to distinguish between three ranges. At low temperature the decay is always exciton driven and at temperature close to room temperature it's possible to see the abundance of dissociated free electron-hole pairs. For intermediate temperatures there is a third range where the proportion of the two species is comparable, giving decay dynamics influenced by both species in a similar fashion. Figure 4-9 also emphasizes the effect of the injected carrier density on the appearance of each subsequent regime as the temperature of the sample is increased. It is possible to observe how a higher value of N pushes the influence of the excitonic component of the decay dynamics to higher temperatures.

A second set of solutions for the Saha equation has then been compared for a variation in the exciton binding energy over three orders of magnitude, from 1 to 100 meV, while keeping constant $N = 1 \cdot 10^{14} cm^{-3}$ and again for no initial hole doping.

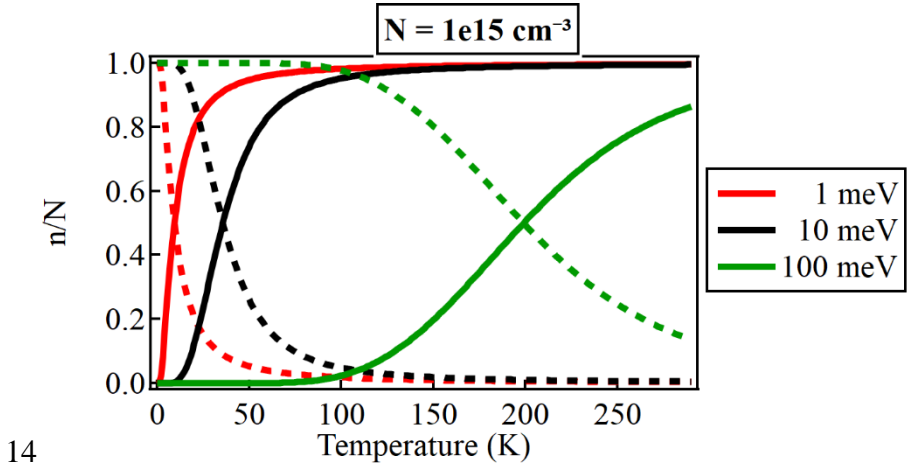


Figure 4-10: Fraction of electrons and excitons over the total photo-generated charges as a function of T for different exciton binding energy at fixed excitation density. Solid (dashed) lines represent the electrons (exciton) population over the total population.

Figure 4-10 once again shows the number of free charges and excitons normalised to N for 1, 10 and 100 meV. These particular values for E_b have been chosen in order to cover the spectrum of the reported binding energies typically found in the literature [25]. The effect of an increasing E_b is similar to the effect described above for the injected carrier density. As discussed in the introduction to this chapter, this has been a well understood fact ever since early studies of the decay dynamics in methylammonium perovskites. Nevertheless, we believe it is important to stress that a reliable estimation of the temperature dependence of exciton binding energy is a necessary base for building a correct model to describe the photoluminescence properties of these materials.

A final set of solutions to the equation has then been calculated by varying the doping level of the hole density, keeping E_b and N constant.

Exciton Binding Energy

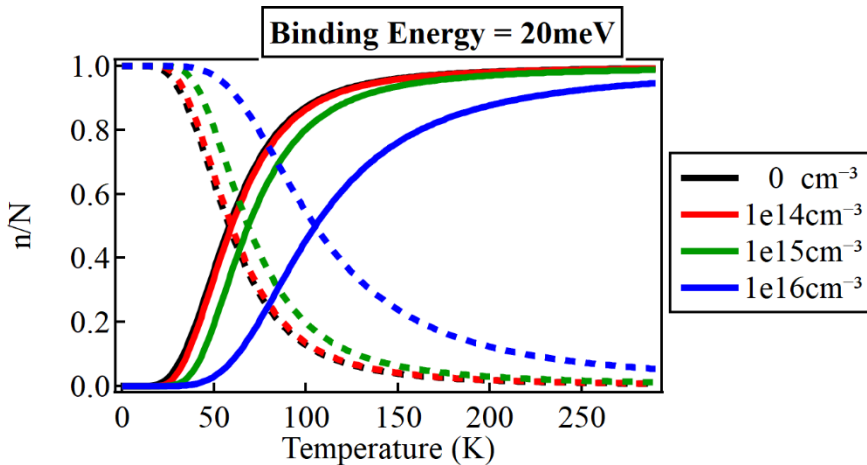


Figure 4-11: Fraction of electrons and excitons over the total photo-generated charges as a function of T for different doping densities at fixed exciton binding energy and excitation power. Solid (dashed) lines represent the electrons (exciton) population over the total population.

Again, the percentage of the two photogenerated species as a function of temperature shows a strong dependence on the level of the parameter examined (Figure 4-11). Increasing the doping density acts in a very similar way to increasing the total photogenerated carrier density. This means that, at any given fixed temperature, samples that have a higher trap state concentration will exhibit less free electrons compared to samples with lower trap densities.

Chapter 5 Steady State PL analysis

5.1 Introduction

In this chapter we will present the main features obtained by analysis of time integrated photoluminescence emitted by thin polycrystalline films of MAPI perovskites. In particular, in Section 5.2 we will analyse the temperature dependence of the PL spectra, showing how it is possible to extract the energy of the phonons involved in scattering processes with the charge carriers. Successively, in Section 5.3, some of the properties of the near band edge photoluminescence as a function of the incident excitation power will reveal themselves to be useful in determining the nature of the mechanisms responsible for charge carrier recombination.

5.2 PL vs Temperature

5.2.1 Tetragonal and Orthorhombic phases

Steady-state PL spectra of a MAPbI_3 thin-films were obtained for a range of temperatures and fluences, following above-bandgap excitation. The spectra were recorded using the setup described in section 3.2. We excited the sample using a pulsed laser source having a wavelength of 400 nm and repetition rate of 80 MHz. The sample, kept inside a cryostat, was progressively cooled down from room temperature with steps of 2 K, allowing sufficient time for the film to achieve thermal equilibrium before acquiring each spectrum.

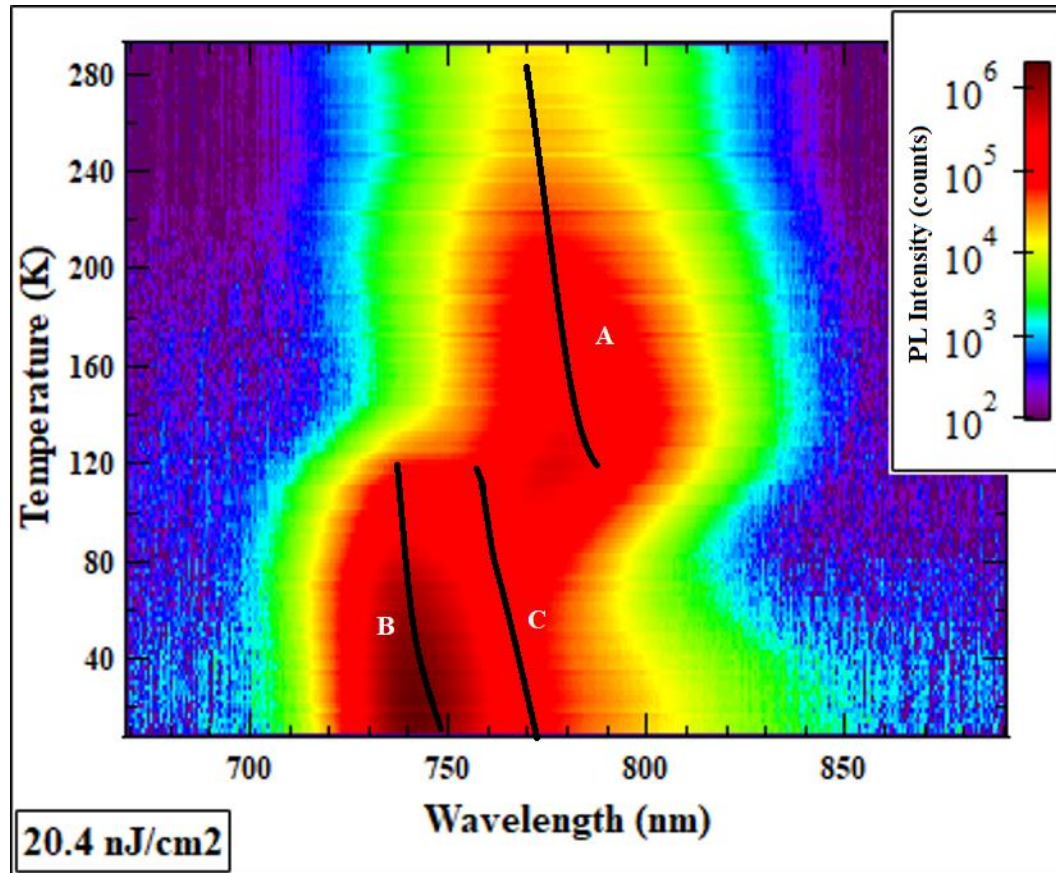


Figure 5-1: Temperature map of time integrated PL of MAPI thin film. The image is obtained from steady state PL spectra recorded at fixed excitation density every 2 K. The black lines serve as guide for the eye and represent the maxima for PL emission related to the tetragonal phase at high temperature (A), the orthorhombic phase (B) and the tetragonal phase (C) in the low temperature range.

The temperature dependence of the PL at a constant fluence is shown in Figure 5-1. The shape of the PL and position as a function of temperature is similar to that previously reported [54]–[56]. Within each phase the peak of the PL redshifts with decreasing temperature, following the trend of the absorption due to the non-Varshni behaviour of the bandgap described in the previous section (Figure 4-1 a). Below the temperature of the phase transition (< 140 K) the orthorhombic phase PL peak begins to emerge, and dual emission is observed even at temperatures below 100 K. This has been attributed to phase coexistence by many authors but remains a topic of debate [57]–[59]. At low temperatures, a similar trend of the bandgap

dependence on temperature is found for the orthorhombic phase (redshifting with decreasing temperature). We attribute the single peak appearing in the highest temperature range of the experiment to the near band edge luminescence of the perovskite lead iodide MAPbI_3 corresponding to its tetragonal crystalline structure. As the temperature is decreased a new peak emerges at shorter wavelengths. We attribute this second peak to the orthorhombic phase, and the higher wavelength peak again to the tetragonal phase. We therefore postulate the coexistence of the two phases.

5.2.2 Temperature-Dependent Linewidth Broadening

Electron-phonon coupling in perovskites such as MAPbI_3 has been previously studied, with differing conclusions drawn about the nature of the interactions [37], [55], [60]. There is interests in this topic since it provides information about the fundamental limitations of the material for optoelectronic applications. Namely, the mobility of charge-carriers is limited by scattering from phonons that will be present at non-zero temperatures which devices operate at. Additionally, for photovoltaic applications, photoexcitation is above-bandgap and carriers thermalize to the band-edge via phonon interactions. Photoluminescence results provide information pertaining to the nature of phonons, since electron-phonon interactions change the shape of the photoluminescence spectrum that is obtained. Such interactions broaden the PL, which is then needed to be described by a broadening function.

The linewidth of the PL (full-width at half-maximum), increases with temperature for the MAPbI_3 as shown in Figure 5-2. The broadening for the room temperature phase appears to be homogenous due to the scattering of charge-carriers by phonons that increases the linewidth of the PL. It has been shown that due to the polar nature of lead-halide perovskites such as MAPbI_3 , the dominant mode is the longitudinal optical (LO) phonon via Fröhlich interactions [61]. As a result, the linewidth broadening as a function of temperature $\Gamma(T)$ can be fitted with:

$$\Gamma(T) = \Gamma_0 + \frac{\gamma}{\left(e^{\frac{E_{LO}}{k_B T}} - 1 \right)}, \quad (5-1)$$

where Γ_0 is the linewidth at 0 K, γ is the strength of the Fröhlich coupling and E_{LO} is the energy of the longitudinal optical phonon. However, since MAPbI_3 undergoes a phase transition around 140 K, we see dual emission around this temperature. Hence, we are unable to determine the linewidth for the tetragonal peak below temperatures of 140 K. However, at low temperatures we can consider the value of the linewidth of the orthorhombic phase PL peak, assuming that the same phonon mode is dominant in both phases. The expected trend with temperature for the linewidth broadening via Fröhlich interactions is observed, as shown in Figure 5-2 yielding a value of 10 meV for E_{LO} , which is similar to those previously found experimentally and from the results of calculations [56], [60], [61]. The inhomogeneous broadening Γ_0 is found to be 37 meV, which again is similar to previously reported values. The Fröhlich coupling strength γ is found to be 22 meV, which is slightly lower than typically stated values for MAPbI_3 , indicative of weaker electron-phonon coupling in our sample.

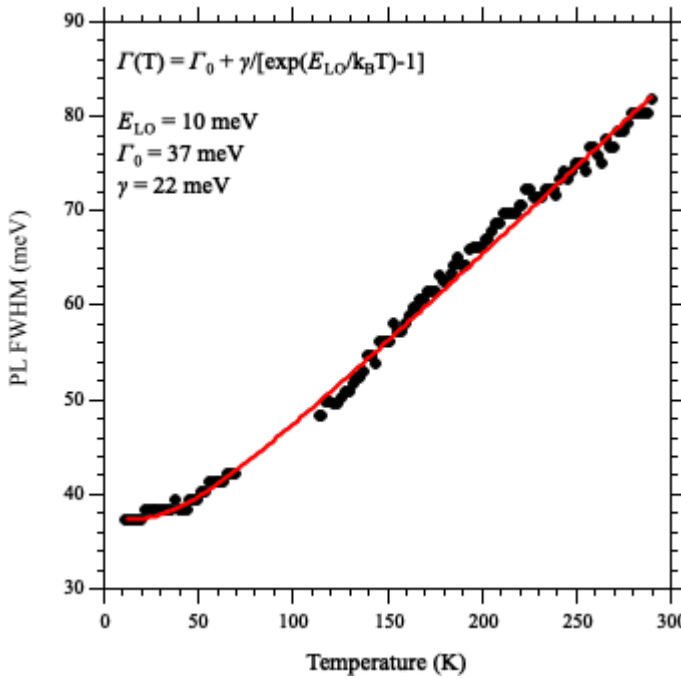


Figure 5-2: Experimental and fitted values of FWHM of the PL emission corresponding to the tetragonal phase of MAPI. The markers

correspond to the experimental values extracted for the time integrated PL. The red line represents the fitting of equation 5-1. The fitting parameters are reported as inset in the figure.

5.3 PL vs Excitation Density

Near band edge photoluminescence (NBEPL) represents the main emission mechanism in many direct semiconductors, whether the emitted photons come from direct electron-hole or exciton recombination or if it originates from a transition involving bound states close to the band edge. It has initially been suggested that the nature of the process involved in recombination dynamics can be inferred from the dependence of the emitted PL intensity (I) as the excitation density is varied [62]. Further studies pointed out the existence of a power law of the form $I \propto L^k$, where L is the exciting radiation power and the exponent k depends on the transition involved. This early calculation estimated $1 < k < 2$ for exciton like transitions and $k < 1$ for free-to-bound or bound-to-bound transitions [63], [64]. Even earlier models used sets of rate equations to explain the superlinearity of the effect observed in experimental data [65]. Nevertheless, discrepancies were found between these models and experiments due to the effect of non-uniform distributions of photo-excited carriers or because of the presence of competitive non-linear or non-radiative effects [66]. Therefore, a more comprehensive model was proposed in order to take into account the effects of free carriers recombination as well as the effects of free to bound states recombination [18].

5.3.1 Dependence of NBEPL on Excitation Power

Due to the complexity of the problem a few initial assumptions are made. First, we again consider only above band gap excitation. Second, we assume charge neutrality by having the electron concentration in the conduction band, n , to be equal to the hole concentration in the valence band, h . Third, the doping or trap concentration is much smaller than the photo-generated electron density, so that it is possible to apply to the exciton density x the simple form of the Saha equation $n^2 = Ax$. Fourth, we deal only with donor bound excitons and electron traps, since

we expect the analogous process for acceptors and hole traps to be symmetric. Finally, we take into account just a set of transitions to describe the excitation-relaxation process, as schematically illustrated in Figure 5-3.

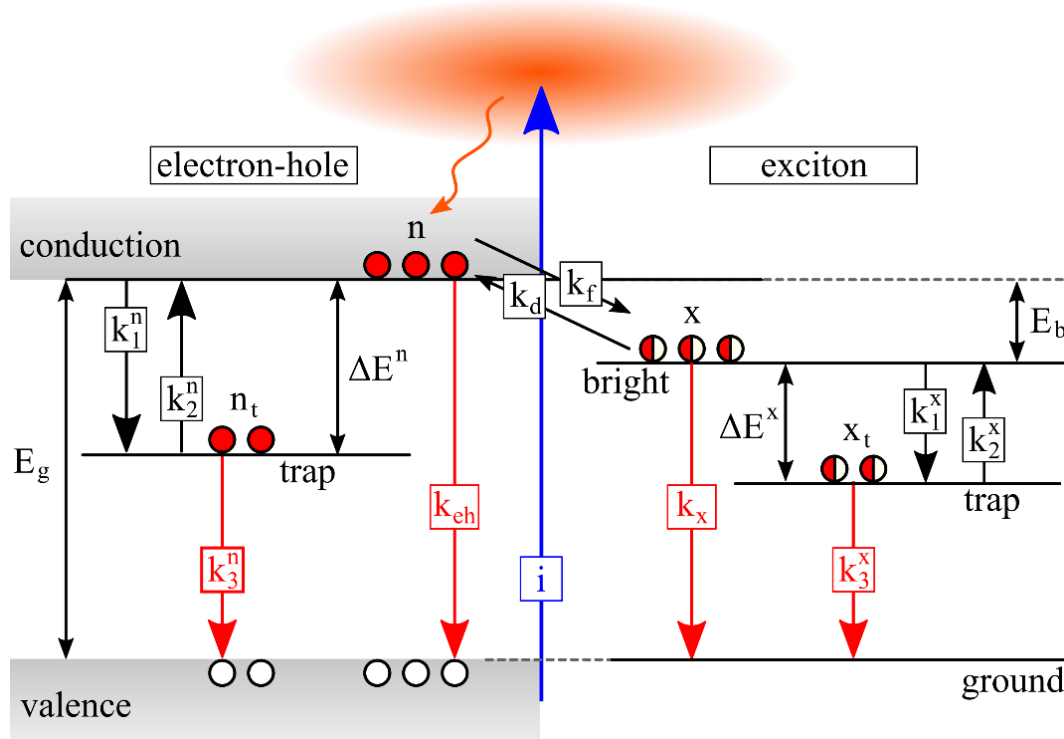


Figure 5-3: Radiative and non-radiative transitions included in the model for NBEPL. This schematic considers a set of possible recombination channels for excited electron-hole pairs (left side) and excitons (right side). Radiative transitions are indicated by red arrows, and non-radiative by black arrows.

We consider a model similar to the band structure for methylammonium lead iodide perovskites described in section 2.4, consisting in a conduction and a valence band separated by a band gap energy E_g . We assume for simplicity a single energy state for electrons and excitons traps instead of a distribution of different energies. The excitation process is the promotion of a free electron to the conduction band (i) and it is proportional to the laser excitation power L and it is described by the rate $i \cdot L$. The processes that involve the electrons are depicted on the left side of Figure 5-3. Hereby the rate of electron-hole pair recombination is described by the term $k_{eh}n^2$. Considering an electron trap density N^e , the transitions involving these states can

be (k_1^n) non-radiative capture of a free electron from the conduction band to the trap state, (k_2^n) non-radiative promotion of a bound electron to the conduction band and radiative recombination of a bound electron and a free hole (k_3^n) , having respectively rates $k_1^n(N^e - n_T)n$, $k_2^n \cdot n_T$ and $k_3^n n_T n$, where n_T is the occupancy of these trap states. The second group of transitions involve excitons, that are summarized in the left part of the schematics in Figure 5-3. Recombination of free excitons is proportional to $k_x x$. Furthermore excitons show transitions between the excitonic bright state and exciton trap states of density N^x . Non-radiative decay (k_1^x) of a free exciton into a bound state, its inverse process (k_2^x) of non-radiative re-emission and finally the radiative recombination of bound excitons (k_3^x) are depicted, where the products $k_1^x(N^x - x_T)n$, $k_2^x \cdot x_T$ and $k_3^x x_T$ represent the respective rates. In summary these processes can be described by a set of coupled ordinary differential equations:

$$\frac{dn}{dt} = iL - k_{eh}n^2 - k_f n^2 - k_1^n(N^e - n_T)n + k_2^n n_T \quad (5-2)$$

$$\frac{dn_T}{dt} = k_1^n(N^e - n_T)n - k_2^n n_T - k_3^n n_T n \quad (5-3)$$

$$\frac{dx}{dt} = k_f n^2 - k_x x - k_1^x(N^x - x_T)x + k_2^x x_T \quad (5-4)$$

$$\frac{dx_T}{dt} = k_1^x(N^x - x_T)x - k_2^x x_T - k_3^x x_T \quad (5-5)$$

In the steady state, the above set of equations have vanishing time derivatives. The luminescence intensities of the radiative recombination are respectively:

$$I_n = k_{eh}n^2 \quad (5-6)$$

$$I_{n_T} = k_3^n n_T n \quad (5-7)$$

$$I_x = k_x x \quad (5-8)$$

$$I_{x_T} = k_3^x x_T \quad (5-9)$$

We consider three separated cases.

(i) In the first case bimolecular and exciton recombination are the dominant process. Therefore, only a small portion of charges recombine via trap states. In this case we can consider only the quadratic terms in equation 5-2 to describe the electron

Steady State PL Analysis

density n . We analyse separately the dependence of the emissions of each one of the radiative transitions considered in the model.

- *Free charges:*

$$\frac{dn}{dt} \approx iL - k_{eh}n^2 - k_f n^2 = 0. \quad (5-2b)$$

If $\alpha = k_{eh} + k_f$ and recalling the expression for the intensity of the bimolecular recombination, we obtain:

$$n^2 \approx \frac{i}{\alpha} L \xrightarrow{\text{yields}} I_n \approx \frac{ai}{\alpha} L. \quad (5-6b)$$

The emission is linear with the excitation power, which describes a power exponent equal to unity, i.e. $k = 1$.

- *Trapped electrons:*

If bimolecular recombination is dominating then we can assume $n, N^e \gg n_T$, which implies $(N^e - n_T) \approx N^e$, where the steady state condition for rate equation (5-3) becomes:

$$\frac{dn_T}{dt} \approx k_1^n N^e n - k_2^n n_T n = 0. \quad (5-3b)$$

Once again, combining with the intensity $I_{n_T} = k_3^n n_T n$ allows us to derive the dependence on the excitation density:

$$n_T \approx \frac{k_1^n N^e}{k_3^n} \xrightarrow{\text{yields}} I_{n_T} \approx k_1^n N^e \sqrt{\frac{i}{\alpha} L}, \quad (5-2b)$$

where we used equation (5-6b).

- *Free excitons:*

$$\frac{dx}{dt} \approx k_f n^2 - k_x x = 0. \quad (5-4b)$$

The intensity of free exciton decay being $I_x = k_x x$, and substituting the expression for n as a function of the laser power L (5-2b) yields to

$$x \approx \frac{k_f}{k_x} n^2 \xrightarrow{yields} I_x \approx k_f i L \quad (5-8b)$$

Likewise the intensity of the emission from free excitons is linear with the excitation power.

- *Trapped excitons:*

if bimolecular recombination is dominating then we can assume $x, N^x \gg x_T$, which implies $(N^x - x_T) \approx N^x$, with the steady state condition for rate equation (5-9) becoming:

$$\frac{dx_T}{dt} \approx k_1^x N^x x - k_2^x x_T - k_3^x x_T = 0 \quad (5-3)$$

Defining $\gamma = \frac{k_1^x N^x}{k_2^x + k_3^x}$ we can simplify to $x_T = \gamma x$ and after substitution of equation (5-2b) to $I_{x_T} = k_3^x \gamma \frac{k_f}{k_x} n^2$. Recalling the dependence of n to the laser power we can further write:

$$x_T \approx \frac{k_1^x N^x}{k_2^x + k_3^x} x \xrightarrow{yields} I_{x_T} \approx k_3^x \gamma \frac{k_f}{k_x} \frac{i}{\alpha} L, \quad (5-9b)$$

which leads to $k = 1$.

(ii) In the second case we consider that most of the photogenerated charges undergo through recombination pathways that involve bound states. In this case the we can describe dominating trap assisted recombination, and therefore neglect the term n^2 :

- *Free charges:*

$$\frac{dn}{dt} \approx iL - k_1^n N_0^e n + k_3^n n_T = 0 \quad (5-4)$$

Since the recombination processes are trap assisted, the traps will be saturated so that we can replace $(N^e - n_T) \approx N_0^e$ in the equation above. The excitation of electrons back to the conduction band is a weak transition so we can ignore the first term in the expression for n . Then, using (5-6), the relation between the emitted intensity and the excitation power becomes:

Steady State PL Analysis

$$n \approx \frac{k_2^n n_T}{k_1^n N_0^e} + \frac{i}{k_1^n N_0^e} L \xrightarrow{\text{yields}} I_n \approx k_{eh} \left(\frac{i}{k_1^n N_0^e} \right)^2 L^2 \quad (5-6c)$$

- *Trapped electrons:*

We again use the approximation $(N^e - n_T) \approx N_0^e$ to write:

$$\frac{dn_T}{dt} \approx k_1^n N_0^e n - k_2^n n_T - k_3^n n_T n = 0 \quad (5-3c)$$

$$n_T \approx \frac{k_1^n N_0^e}{k_2^n + k_3^n} n \xrightarrow{\text{yields}} I_{n_T} \approx k_3^n \frac{i}{k_2^n + k_3^n} L \quad (5-8c)$$

- *Free exciton:*

As for the free electron case, the trap saturation leads to $(N^x - x_T) \approx N_0^x$.

Considering the steady state condition, we can rewrite eq. (5-4) as

$$\frac{dx}{dt} \approx k_f n^2 - k_x x - k_1^x N_0^x x + k_2^x x_T = 0. \quad (5-4c)$$

We consider again the direct transition to be weak so that the second term of the expression for x can be neglected. If we define $\beta = \frac{k_f}{k_x + k_1^x N_0^x}$, then $x = \beta n^2$ and using equation (5-6c) to replace n the intensity becomes:

$$x \approx \beta n^2 \xrightarrow{\text{yields}} I_x \approx k_x i L^2 \quad (5-8c)$$

- *Trapped excitons:*

$$\frac{dx_T}{dt} \approx k_1^x N_0^x x - k_2^x x_T - k_3^x x_T = 0 \quad (5-5c)$$

Using equation (5-8c) for x and equation (5-9) for I_{x_T} yields to

$$x_T \approx \frac{k_1^x N_0^x}{k_2^x + k_3^x} x \xrightarrow{\text{yields}} I_{x_T} \approx \frac{\beta}{k_2^x + k_3^x} \frac{i^2}{k_1^n N_0^e} L^2 \quad (5-9c)$$

(iii) If again above band-gap excitation is considered it is possible to have a third and most common configuration where neither free carriers or trap assisted recombination dominates, then the quadratic terms and the linear terms in the rate equation for the electrons are of the same order of magnitude. In this case it is not possible to introduce any obvious simplification and the expression of the PL

intensity as a function of the laser power could still be described by a power law, but the coefficient k will be dependent on the interplay between free and trapped charges. Similar studies reporting on the comparable models to calculate the coefficient k predicted for this case values of k between 1 and 2 [66].

We summarise the obtained values of k in the following table:

	I_{eh}	I_{n_T}	I_x	I_{x_T}
<i>Non trap assisted</i>	1	0.5	1	1
<i>Trap assisted</i>	2	1	2	2

Table 5-1: Values of the power exponent k for different radiative recombination routes.

5.3.2 Results and discussion

The fluence dependence of the PL at room temperature is shown in Figure 5-4a between $\sim 1\text{nJcm}^{-1}$ and 200nJcm^{-1} . The PL increases with increasing photoexcitation density, as expected and follows an over-linear power-law dependence. The PL is found to be proportional to $L^{1.7}$, as expected for emission from a mixture of both exciton and free-carrier recombination. This value is also obtained for temperatures in the phase transition region as well as lower temperatures. At 140 K, two distinct peaks belonging to the two structural phases have similar intensities. The fluence dependence of the total intensity is again found to be proportional to $L^{1.7}$. However, the PL spectra at 140 K can be deconvolved into two separate emissions and the corresponding dependence for each peak can be extracted. It is found that the tetragonal phase peak remains proportional to $L^{1.7}$, whereas the higher energy orthorhombic peak is proportional to L^2 . We did not observe any considerable shift in the PL peak energy with increasing fluence for any temperature.

Steady State PL Analysis

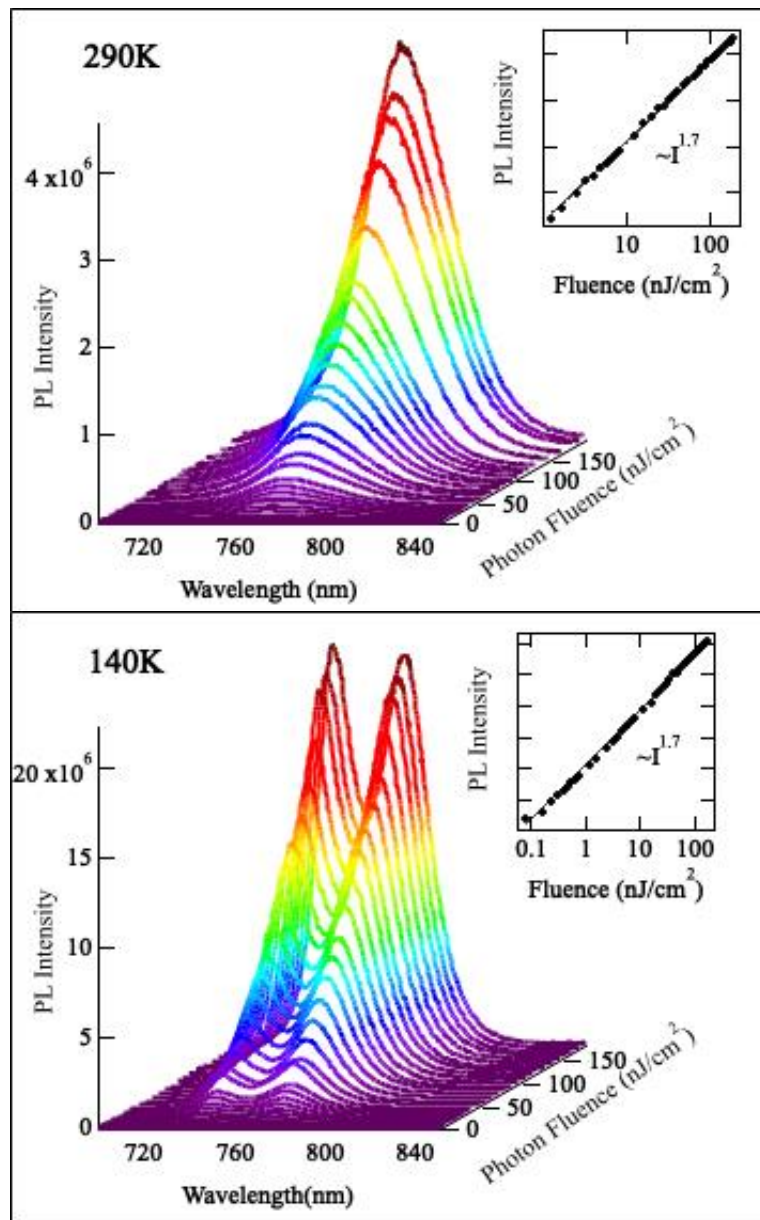


Figure 5-4: PL vs Excitation Fluence at 290 (a) K and 140 K (b). Spectra recorded at fixed temperature are shown as a function of the relative photon fluence. The inset of the two graphs shows the values of the PL intensity obtained by Gaussian fit of the spectra. The PL Intensity vs Excitation Fluence curves are fitted with a power law with exponent k .

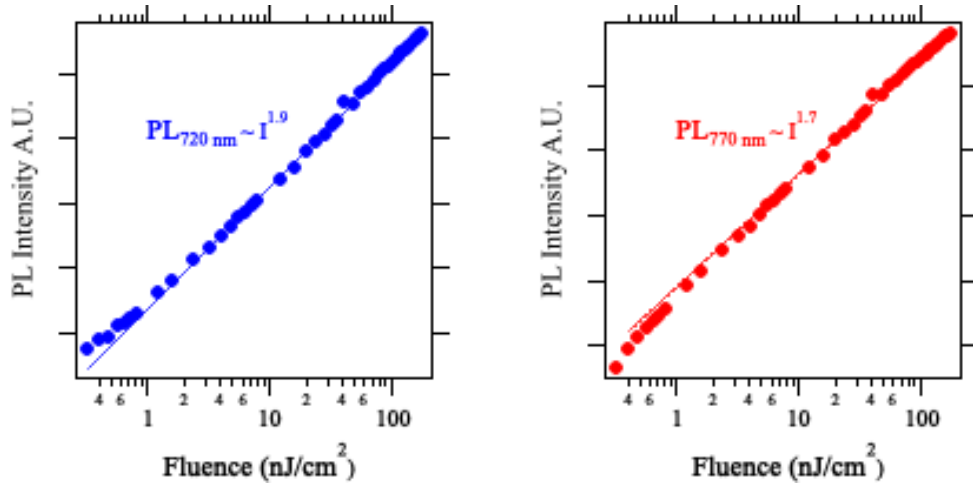


Figure 5-5: Fit PL vs Intensity for the tetragonal peak (red) and orthorhombic (blue). The two panels show the power law fit of the two peak found for $T = 140$ K, where the PL intensities are obtained by deconvolution of each spectrum into two Gaussian peaks.

The fitted values for the exponent at different temperatures can be compared with theoretical calculation presented in Section 5.3.1. This gives us an indication into the nature of the processes involved in the emission of the NBEPL observed upon steady state laser excitation of the MAPI films. The values obtained for the tetragonal peak centred around 770 nm are consistent across the whole temperature range, showing a constant value equal to 1.7. This corroborates the assumption that the emitted luminescence is due to electron-hole and exciton recombination processes. Furthermore, since the value is in between 1 and 2, we conclude that the recombination in MAPI films occurs via a combination of direct and trap assisted channels. Regarding the orthorhombic peak, a value closer to 2 can be interpreted as an indication that the recombination occurs mostly through trap assisted excitonic channels. This could further suggest that the orthorhombic phase presents a higher spatial density of intraband trap states.

Chapter 6 Recombination Processes in Methylammonium Lead Trihalide Perovskites

6.1 Introduction

As introduced in Chapter 2, one of the most relevant properties of perovskites for optoelectronic applications is their high charge-carrier mobility ($8\text{-}33\text{ cm}^2\text{ (Vs)}^{-1}$) leading to diffusion lengths that exceed hundreds of nanometres[49], [54]. The observed long lifetimes of charge-carriers are additionally significant. Understanding of charge-carrier recombination mechanisms therefore represents a fundamental component in the design of class efficient devices, minimizing all the possible losses due to competing recombination pathways.

Since early studies [25] the temporal evolution of carrier density $n(t)$ has been interpreted as the sum of different contributing mechanisms that are associated with monomolecular, bimolecular and Auger recombination. The first one contains excitonic and trap-assisted recombination, as both relay on individual carrier density. The second contribution reflects the intrinsic band-to-band recombination and is due to the product of electron and hole densities $nh = n^2$, reflecting the fact that for photo-generated electron-hole couples $n = h$. Auger recombination is typically a three bodies process involving the recombination of an electron with a hole in the presence of a third electron or hole, leading to a dependence proportional to n^3 . The complete picture can be summarized in the rate equation for the charge density:

$$\frac{dn}{dt} = -R_3 n^3 - R_2 n^2 - R_1 n,$$

where R_1 , R_2 and R_3 are the rate constant associated with monomolecular, bimolecular, and Auger recombination [19].

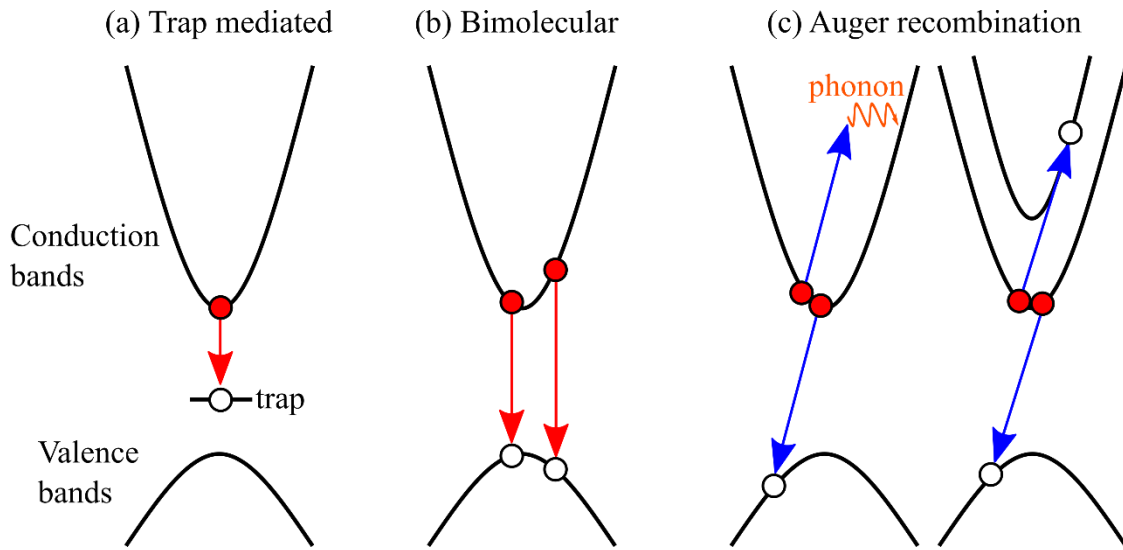


Figure 6-1: Schematic diagram of recombination processes in a semiconductor material.

In order to describe carrier recombination, a range of different models have been proposed that take into account trap-assisted recombination [50], [67], [68], the presence of an indirect band-gap [69], donor-acceptor-pair recombination [5], reverse intersystem crossing [70] and other mechanisms. Due to the number of existing models, there remains a lack of agreement concerning the origin of the long recombination lifetimes. Furthermore, most of the studies published thus far have investigated either the high temperature tetragonal phase or focused on a limited excitation density range.

In light of existing studies, we believe that a more comprehensive analysis of the charge dynamics in organic-inorganic halide perovskites is necessary. We conducted a series of TRPL experiments on MAPI films over a wide range of temperature and photo excited carrier densities in order to gain insight to the recombination processes involved in the luminescence emission of this kind of perovskite. In particular, we aimed to propose a kinetic model for carrier recombination that can explain the decay dynamics observed in the temperature range between 290 and 12 K and for laser powers resulting in photo-generated charges densities between $1 \cdot 10^{14}$ and $1 \cdot 10^{17} \text{ cm}^{-3}$. The results of the experiments presented in chapter 4 and chapter 5 have been incorporated to the analysis of the TRPL data.

6.2 Recombination Processes Model

In this thesis we propose a complete model able to effectively describe the full extent of decay dynamics observed. The model is presented in Figure 6-2. We consider the methylammonium lead iodide perovskite material as a direct band gap semiconductor having a band gap that varies as a function of the temperature of the sample, $E_g(T)$. The dependence of the band gap on the temperature has been calculated in chapter 4. Under a laser excitation of intensity L a density $N(0)$ of photo-generated species is produced. This total concentration of species consists of the sum of free electrons in the conduction band, having density n , and free excitons, with density x , so that the relation 6-1

$$N(0) = n + x \quad (6-1)$$

holds for the densities of the two species.

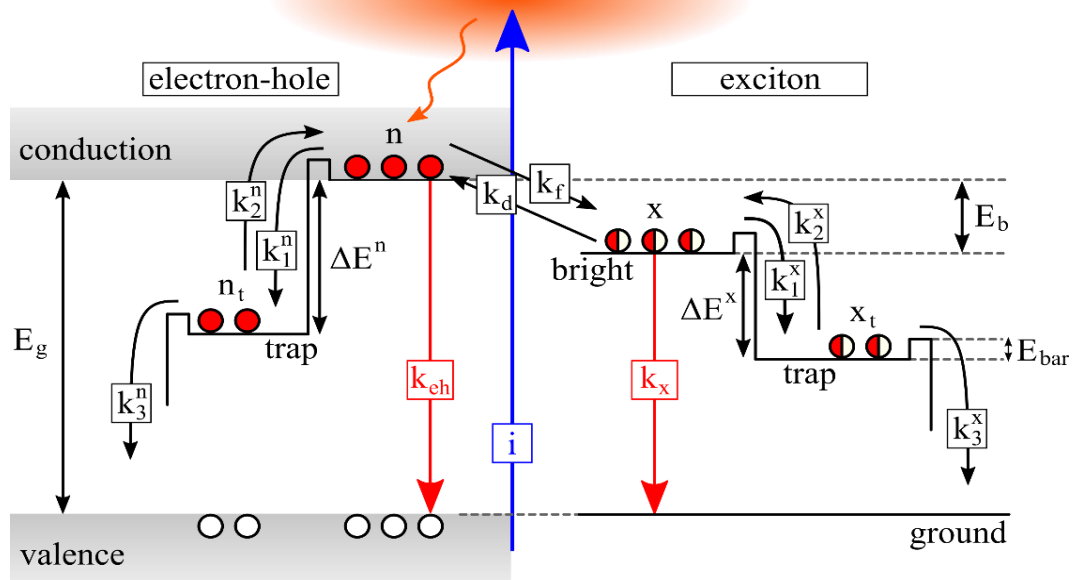


Figure 6-2: Radiative and nonradiative transitions included in the model for carrier recombination dynamics in MAPI thin films. This schematic considers a set of possible recombination channels for excited electron-hole pairs (left side) and excitons (right side). Radiative transitions are indicated by red arrows, and nonradiative by black arrows. Laser excitation (blue arrow) promotes e^- from VB to CB.

We postulate the presence of an intraband trap state at energy $E_{Traps} = E_g - \Delta E^n$.

There are N^e electronic traps per cubic centimetre. In this model we consider only electronic traps, but it is possible to demonstrate that the same results can be obtained considering hole traps [67]. An electron in the conduction band can then be trapped into this state, contributing to the total concentration of trapped electrons that we will indicate by n_T . Since charge neutrality must be conserved, the number of total photo-generated holes in the valence band will be at any time given by the sum of electrons in the conduction band and those being trapped, i.e:

$$h = n + n_T. \quad (6-2)$$

Furthermore, a density N^x of trap states for excitons is introduced. The energy splitting between these two stages is ΔE^x and the density of trapped excitons is denoted as x_T .

6.2.1 Rate Equations for the Recombination Processes

A detailed kinetic model accounts for all the processes that govern the recombination of the carrier species in methylammonium lead iodide perovskite. We describe such a model with the series of rate equation presented below.

Free Electrons:

$$\frac{dn}{dt} = iL - k_f n^2 + k_d x - k_{eh} nh - k_1^n (N^e - n_T) n + k_2^n n_T \quad (6-4)$$

Trapped Electrons:

$$\frac{dn_T}{dt} = k_1^n (N^e - n_T) n - k_2^n n_T - k_3^n n_T n \quad (6-5)$$

Free excitons:

$$\frac{dx}{dt} = k_f n^2 - k_d x - k_x x - k_1^x (N^x - x_T) x + k_2^x x_T \quad (6-6)$$

Trapped electrons:

$$\frac{dx_T}{dt} = k_1^x (N^x - x_T)x - k_2^x x_T - k_3^x x_T \quad (6-7)$$

The first equation describes the processes involving free electrons in the conduction band, the second one electrons in the trap state, the third one free excitons and the last one finally the trapped excitons. The term iL in equation (6-4) presents the generation of free electrons due to the laser excitation, which is set to zero since we are considering decay dynamics only. The electron-hole recombination rate is described by $k_{eh}nh$, where k_{eh} is the bimolecular recombination rate coefficient, while the exciton recombination rate is described by k_x . These two decay channels are the only radiative recombination processes that are considered in this model. The terms $k_f n^2$ and $k_d x$ are the rates of exciton formation and dissociation, respectively, and they appear in both the first and in the equation for the free excitons. The parameters k_1^n , k_2^n and k_3^n determine the electron trapping and detrapping rates into the conduction band as well as deexcitation of trapped electrons into the valence band. Likewise, the values k_1^x , k_2^x and k_3^x represent the analogous trapping, detrapping and recombination rates for the trapped excitons x_T .

In order to describe the observed PL emission, it is necessary to introduce one additional rate equation for the emitted photons. This will have the form:

$$\frac{dp}{dt} = k_{eh}nh + k_x x \quad (6-8)$$

This simply states that the emitted photon density p will be the sum of the radiative processes in the recombination dynamics.

6.3 Preliminary Considerations on the Recombination Processes

6.3.1 Exciton Formation and Dissociation

The values for the rates describing the formation of excitons from electron-hole pairs and dissociation of the former into free charges can be calculated considering the interactions between the two species and with the thermal bath of phonons in the material [71]. This approach, even if more rigorous, would require detailed

analysis on the structural properties of MAPI and on the decay dynamics on a picosecond time scale, which exceeds the scope of this thesis. We decided instead to take into consideration the effect of these two terms on the time-resolved PL in order to estimate their order of magnitude. For these calculations we used numerical methods to solve sets of ODEs, as described in Section 3.4. As we reported in Chapter 4 the equilibrium values of the exciton and free electron-hole pair densities, x , n and h , depend on the thermodynamic equilibrium conditions dictated by the Saha equation (4-13). This is the result of two competitive mechanisms of formation and ionization of excitons from and into electron-hole pairs. In the series of rate equations in the previous section, as mentioned above, these two mechanisms are represented by the term $k_f n^2$ for the combination of free carriers into excitons and $k_d x$ for their dissociation [53], [72], [73]. It has been proven [53] that the static solution of equations 6-4 and 6-6 combined are the equilibrium values given by the Saha equation itself. For simplicity we consider the trap densities for our system to be zero, leading to a simplified version of the rate equations:

$$\frac{dn}{dt} = -k_f n^2 + k_d x - k_{eh} n^2, \quad (6-4b)$$

$$\frac{dx}{dt} = k_f n^2 - k_d x - k_x x. \quad (6-6b)$$

It is possible to write the equilibrium condition in this case as:

$$(n + n_T) \cdot n = Ax \xrightarrow{\text{yields}} \frac{n_{eq}^2}{x_{eq}} = A \quad (6-9)$$

where we used the condition $n_T = 0$ and the subscript indicates that the concentrations of electrons and holes reached the thermodynamic equilibrium. This will allow us to further simplify the rate equations as [53]:

$$\frac{dn}{dt} = -r^0 n^2 + r^0 Ax - k_{eh} n^2 \quad (6-4c)$$

$$\frac{dx}{dt} = r^0 n^2 - r^0 Ax - k_x x \quad (6-6c)$$

We are then finally able to describe the formation and ionization of excitons via a single rate r^0 . The equilibrium condition is satisfied as long as the values for n and x given by the solution of the system of two rate equations satisfy the equation for

n_{eq} and x_{eq} at any given time. This means that we can simply solve this system of two rate equations for different values of r^0 and then find the appropriate value of r^0 that accounts for the condition that the solutions for n and x satisfy equation 6-9.

We considered a temperature $T = 140K$ and an electron binding energy $E_b = 20.2\text{ meV}$ and calculated the value of $A = \frac{v_x}{v_h v_e} e^{\left(\frac{E_b}{k_B T}\right)}$ accordingly, obtaining $\frac{n_{eq}^2}{x_{eq}} = A = 1.15 \cdot 10^{16}\text{ cm}^{-3}$. We considered an initial photo-generated total carrier density $N(0) = n + x = 1 \cdot 10^{16}\text{ cm}^{-3}$, solving the Saha equation for this initial density gives $n_{eq} = 6.425 \cdot 10^{15}\text{ cm}^{-3}$ and $x_{eq} = 3.575 \cdot 10^{15}\text{ cm}^{-3}$. We then solved the system of differential equations 6.4c and 6.6c using the numerical method described in Section 3.4 via the analysis software Igor [23]. We integrated the differential equations over a time range of 100 ns for different values of r^0 while keeping the bimolecular and exciton recombination rates equal to zero, meaning that the particles involved do not decay radiatively. For this calculation we set the initial density of electrons to be equal to $N(0)$ and the initial density of excitons to be zero. In figure 6-3 we show the temporal evolution of the densities of the two particle system as a function of time for three different values of r^0 .

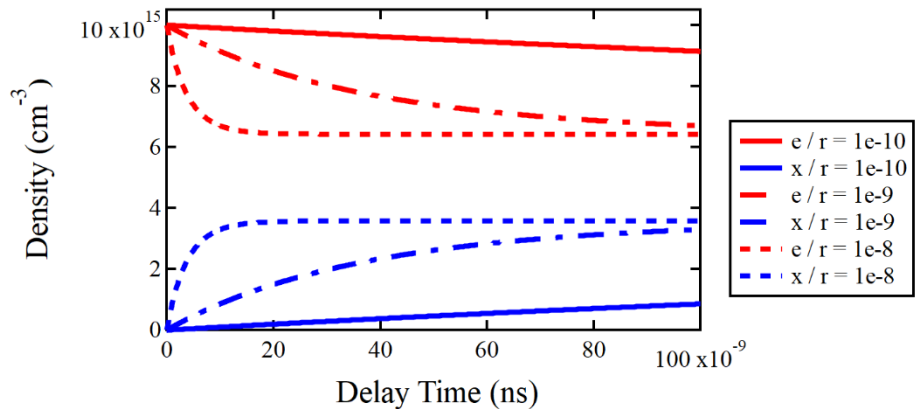


Figure 6-3: Electron and exciton density as function of the rate r^0 .

The first value of r^0 is set to be the smallest, $1 \cdot 10^{-10}\text{ s}^{-1}$, corresponding to the solid lines. We can observe how at time $t = 0$ the exciton and electron densities are equal to the set values. As the system is allowed to evolve in time the electrons start combining (with holes) into excitons, so that n decreases and x increases. Due to

the very small value of r^0 , though, this process is very slow, and the two concentration do not reach their equilibrium value. As r^0 is increased by just an order of magnitude, the process become faster and as it is further increased by another order of magnitude n and x reach their equilibrium values in the timescale of tens of nanoseconds. Typical values for the timescale of exciton ionization and formation for direct bandgap semiconductors are in the order of 10-100 ps [53], [71]. We then resolved the rate equation system in a time interval of 1 ns, with a resolution of 1 ps, and increased the value of r^0 . *Figure 6-4* shows the ratio n^2/x of the solutions of the rate equations as a function of time for r^0 equal to $1 \cdot 10^{-8} s^{-1}$ (red line), $1 \cdot 10^{-6} s^{-1}$ (blue line) and $1 \cdot 10^{-4} s^{-1}$ (green line).

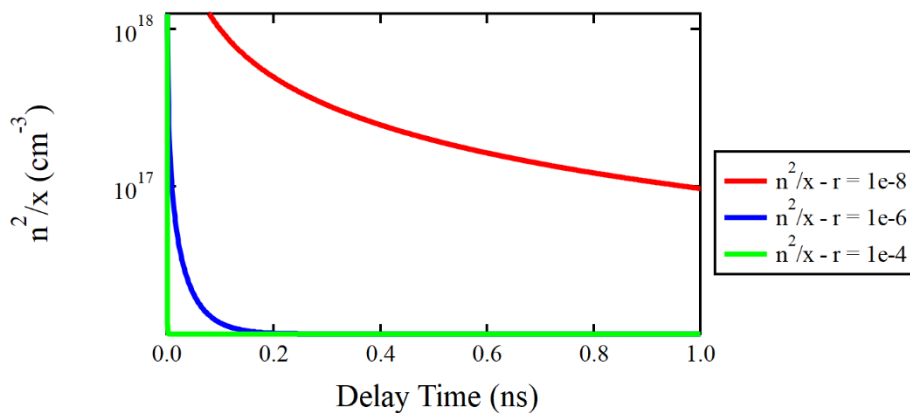


Figure 6-4: Equilibrium densities as a function of delay time for different values of r^0 .

Fixing r^0 to $1 \cdot 10^{-8} s^{-1}$ results on the ratio n^2/x not reaching its equilibrium value of A in the time range considered. The case where value of r^0 is equal to $1 \cdot 10^{-6} s^{-1}$ shows how the equilibrium between the two species is reached after approximately 200 ps and finally the last value of r^0 allow the achievement of the condition imposed by the Saha equation in the first few picoseconds.

Finally, we show the effect of the recombination-ionization terms on the dynamics of the decays for excitons and free carrier. We impose $k_{eh} = 1 \cdot 10^{-8} cm^3 s^{-1}$ and $k_x = 1 \cdot 10^7 s^{-1}$ and study the case for $r^0 = 0$ and $r^0 = 1 \cdot 10^{-4} s^{-1}$. We also applied the Saha law to set the initial conditions for the two densities to be equal to the equilibrium values. In the first case both free carriers and excitons decay following their on typical decay, so we expect a power law for the bimolecular recombination

and a monoexponential decay for the exciton recombination, as showed in Figure 6-4 by the dashed lines for n (red) and x (blue). In this case the curve (dashed green) representing n^2/x shows how the two concentrations diverge from the equilibrium condition.

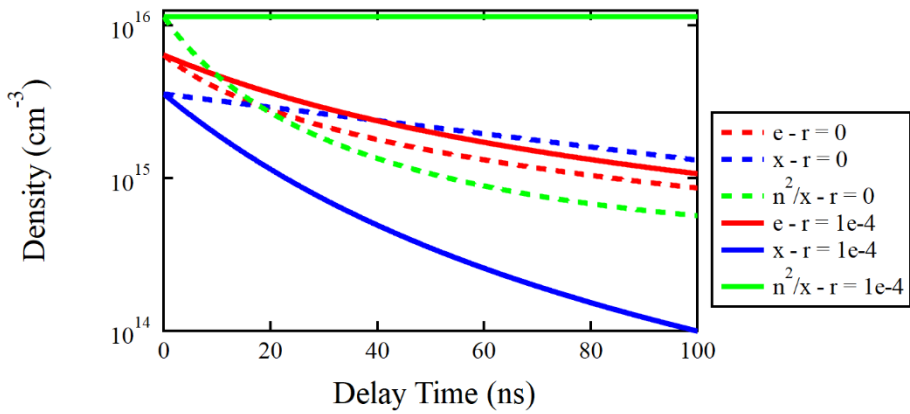


Figure 6-5: Free electrons, free excitons and equilibrium densities as a function of delay time for different values of r^0 .

In the second case, when $r^0 = 1 \cdot 10^{-4} s^{-1}$ the solid green line has a constant value equal to A calculated for the appropriate T and E_b , indicating that the thermodynamic condition between the two species is satisfied at any point in time. The effect on the temporal decay of the particles can be seen on the solid red and blue lines. At any point during the decay, the continuous formation and dissociation of excitons forces the populations of the two species to instantly adjust in order to satisfy the Saha equation, resulting in a significant diversion from the usual decay dynamics that each of the two species would follow separately.

In conclusion, we used the correlation between the Saha equation (4-13) and the processes of exciton formation and dissociation in order to simplify, in our model, the rate equations (6-4 and 6-6) describing the decay dynamics of the free charges and free excitons dynamics. We therefore found an alternative expression for the rates k_f and k_d as a function of a rate r^0 and the Saha parameter A . Finally, we estimated the minimum value of r^0 that allows the thermodynamic condition between free and bound electron-hole pairs to be considered satisfied at any instance within the temporal range of our analysis and within the temporal resolution of the system. This value has been estimated to be $r^0 = 1 \cdot 10^{-4} s^{-1}$.

6.3.2 Phonon Assisted Rates

In addition to radiative decays rates, our model presents a series of non-radiative decay channels. In order to represent the temperature dependence of the transitions between free and trap states it is imperative to take into account phonon assisted rates. We then use a model that takes into account absorption and emission of photons from electrons and excitons, now indicated generically as particles.

Particles in an excited state can non-radiatively relax to trapped states by phonon emission [74], [75]. This is described by decay rate k_1 as follows:

$$k_1 = r_1 \cdot \left(e^{\left(\frac{E_{ph}}{k_B T} \right)} - 1 \right)^{-\frac{E_{barr}}{E_{ph}}} \cdot \left(\frac{e^{\left(\frac{E_{ph}}{k_B T} \right)}}{e^{\left(\frac{E_{ph}}{k_B T} \right)} - 1} \right)^{\frac{E_{barr} + \Delta E}{E_{ph}}}, \quad (6-10)$$

where k_B is the Boltzmann constant r_1 is a rate constant that relates to the efficiency of the process, $\left(e^{\left(\frac{E_{ph}}{k_B T} \right)} - 1 \right)^n$ is the probability of a particle to absorb n phonons of energy E_{ph} and overcome the barrier and finally $\left(\frac{e^{\left(\frac{E_{ph}}{k_B T} \right)}}{e^{\left(\frac{E_{ph}}{k_B T} \right)} - 1} \right)^m$ gives the probability of an particle to emit m phonons of energy E_{ph} and non-radiatively relax into the trap state.

Furthermore, non-radiative processes also take place from the trap state to excited state, where the absorption of a phonon results in the promotion of a trapped particle to the higher energy level, with a rate given by:

$$k_2 = r_2 \cdot \left(e^{\left(\frac{E_{ph}}{k_B T} \right)} - 1 \right)^{-\frac{E_{barr} + \Delta E}{E_{ph}}} \cdot \left(\frac{e^{\left(\frac{E_{ph}}{k_B T} \right)}}{e^{\left(\frac{E_{ph}}{k_B T} \right)} - 1} \right)^{\frac{E_{barr}}{E_{ph}}}, \quad (6-11)$$

where r_2 is the rate constant that characterizes the efficiency of the process and where we have a gain the relevant terms for the probability of particles in the trap to absorb phonons of enough energy to reach the higher energy state.

Finally, we also take into account non-radiative relaxation from the dark trapped states to the ground state with decay rate:

$$k_3 = r_3 \cdot \left(e^{\left(\frac{E_{ph}}{k_B T} \right)} - 1 \right)^{-\frac{E_{esc}}{E_{ph}}} \quad (6-12)$$

Here, again r_3 is the relative efficiency of the process, the term $\left(e^{\left(\frac{E_{ph}}{k_B T} \right)} - 1 \right)^{-\frac{E_{esc}}{E_{ph}}}$

is the probability to absorb a phonon of energy E_{ph} and escape the trapped state and E_{esc} is the energy required for a particle to escape from the trap state [74].

6.3.3 Dependence of k_{eh} on T and E_g .

For direct-bandgap semiconductors it is possible to write a proportionality relation between the value of the recombination rate k_{eh} , the band-gap energy E_g and the temperature T in the form:

$$k_{eh} = k_{eh}^0 \cdot \frac{E_g^2}{(k_B T^{3/2})} \quad (6-13)$$

where k_{eh}^0 is the proportionality factor [76].

6.3.4 Charges accumulation

Time-Resolved Photo-Luminescence measurement on semiconductor materials are performed using a periodic laser input that promotes electrons from the valence band into one or more excited states. The intensity of the luminescence recorded has a temporal dependence that can be studied to gain precious information on the decay dynamics. Usually, the time interval between two subsequent laser pulses is chosen to be long enough to permit all the photo-excited charges to decay to their ground state. Nevertheless, depending on the nature of the processes involved, a laser pulse can excite the sample before all the charges could relax. This is the case of our experiment where we decided to choose a higher repetition rate in order to be able to efficiently collect enough photoluminescence signal even at the lowest excitation densities and therefore have a better signa to noise ratio. The drawback

of a second excitation on the charges before their complete relaxations is that this process results in a pile-up of charges generated by the last laser pulse with the charges that are still in an excited state at the moment that the laser pulse hits the sample. This effect is particularly relevant when considering naturally slow dynamics, typically this is the case of trap assisted recombination. In order to take into account the possibility of this happening in the system studied, we introduced an iterative loop into the calculation on the ODE solution that is used to fit the experimental data. Hereby, in each iteration we sum the newly photo-generated charges to any charges left of the previous iteration in each energetic level considered in our model (Figure 6-2). This mean that, being T the time interval between two laser pulse, the ODE considered in their solution for each one of the rate equations 6-4 to 6-8 the value of these charges at time t , plus the charges at time $t-T$ for each previous iteration. This loop system allows for a direct calculation of the densities on each energetic level without the need to find any approximated analytical expression for the solution of the rate equations.

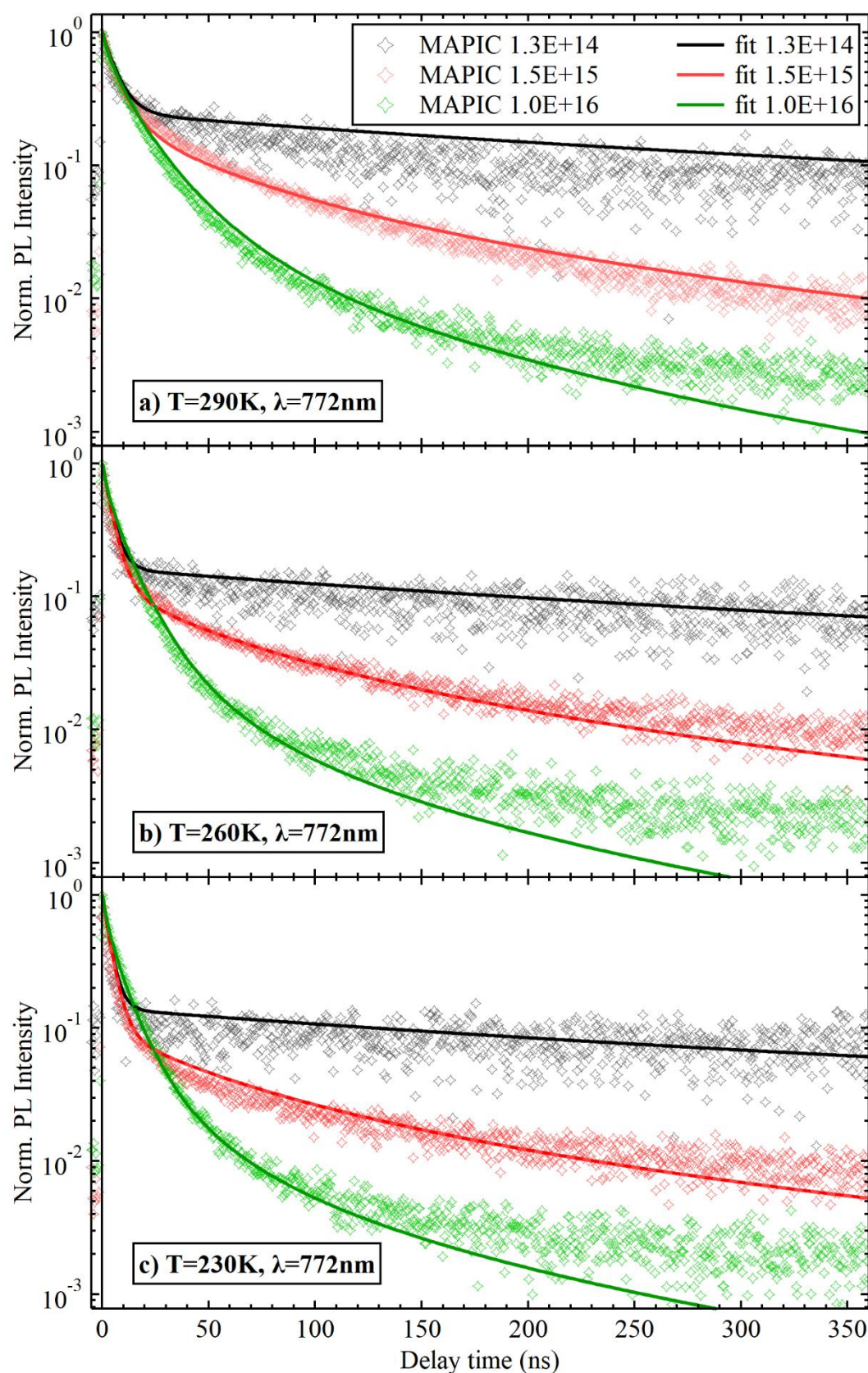
6.4 Results and discussion

A complete set of TRPL decays were acquired on freshly prepared MAPI thin films. The samples, placed in a cryostat, were illuminated by a laser pulsed light at 400 nm and with a repetition rate of 2 MHz. The decays were recorded using the experimental configuration described in Section 3.2.1. The temperature of the sample was kept constant during each acquisition. The temperatures at which the PL was recorded started with room temperature (290 K) and were decreased in steps of 30 K until reaching the lower limit of the cryostat (approx. 12 K). For each temperature the laser power was varied in order to generate into the illuminated area excited carrier densities $N(0)$ of $1.3 \cdot 10^{14}$, $1.5 \cdot 10^{15}$ and $1.0 \cdot 10^{16} \text{ cm}^{-3}$. The emission of the sample was filtered with a monochromator in order to obtain a spectral width of only 20 nm around the peak of the ssPL emission. For the temperatures that showed multiple peaks in the PL spectra, the TRPL decays were recorded for each peak separately, and accordingly labelled.

We solved our set of differential equations using ODE numerical calculations as mentioned in Chapter 3. In order to match the recorded TRPL decays, the solution of the photon density as a function of time, $p(t)$ were differentiated. Finally, both TRPL intensity and the differential of $p(t)$ were normalised. The experimental parameters T and $N(0)$ were added to each solution of the ODE system. Our studies of the absorption spectrum using the Elliott theory model, as reported in Chapter 4, gave us the temperature dependence of E_b , and E_g . These were used to calculate the Saha parameter A (Sec. 6.3.1) and the dependence of k_{eh} over T and E_g (Sec. 6.3.3). The FWHM fit of the time integrated photoluminescence as a function of T (Chapter 5) allowed us to input the phonon energy to use in the expression for the phonon assisted rates, as modelled in Section 6.3.2. Additionally, for the formation and dissociation rates of the excitons we used the approximated value r^0 discussed in Section 6.3.1. Finally, the observations over the steady state PL we made in Chapter 5 were used to assign each observed peak to one of the crystallographic phases, according to the temperature of the sample. We then globally fit the normalised and differentiated emitted photon intensities obtained from equation 6.3-5 to the correspondent experimental normalised decays. The fact that in our model the fit of the differential equations is performed over the whole set of decays for different temperatures and excitation densities means that what is minimised is the total sum of the least squares for all the curves at the same time. This can result in some of the decay to appear not perfectly fitted by the correspondent curve. Nevertheless, it's important to fit the whole set of data globally in order to obtain fitting parameters consistently over the whole temperature and excitation density ranges.

6.4.1 Tetragonal Phase

First, we fitted the low energy peak across all the experimental temperature range. Figure 6-6 shows the time-resolved PL decays as a function of the three excitation fluencies in the temperature range where only one peak is present, nominally the pure tetragonal phase. This correspond to the temperature range before the phase transition. Figure 6-7 shows the time-resolved PL decays from the same peak in the temperature range where both peaks coexist, for temperatures below the phase transition.



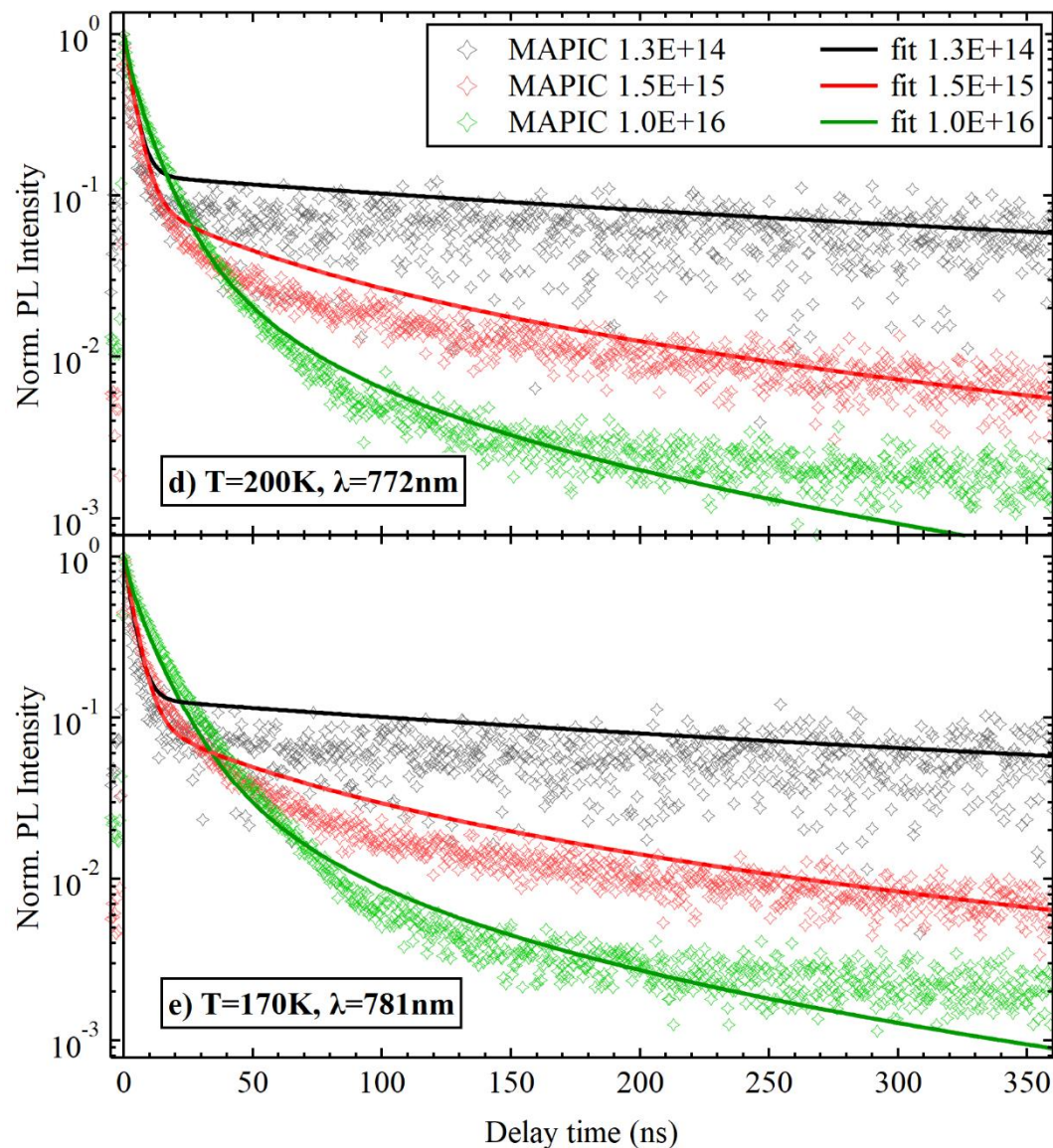
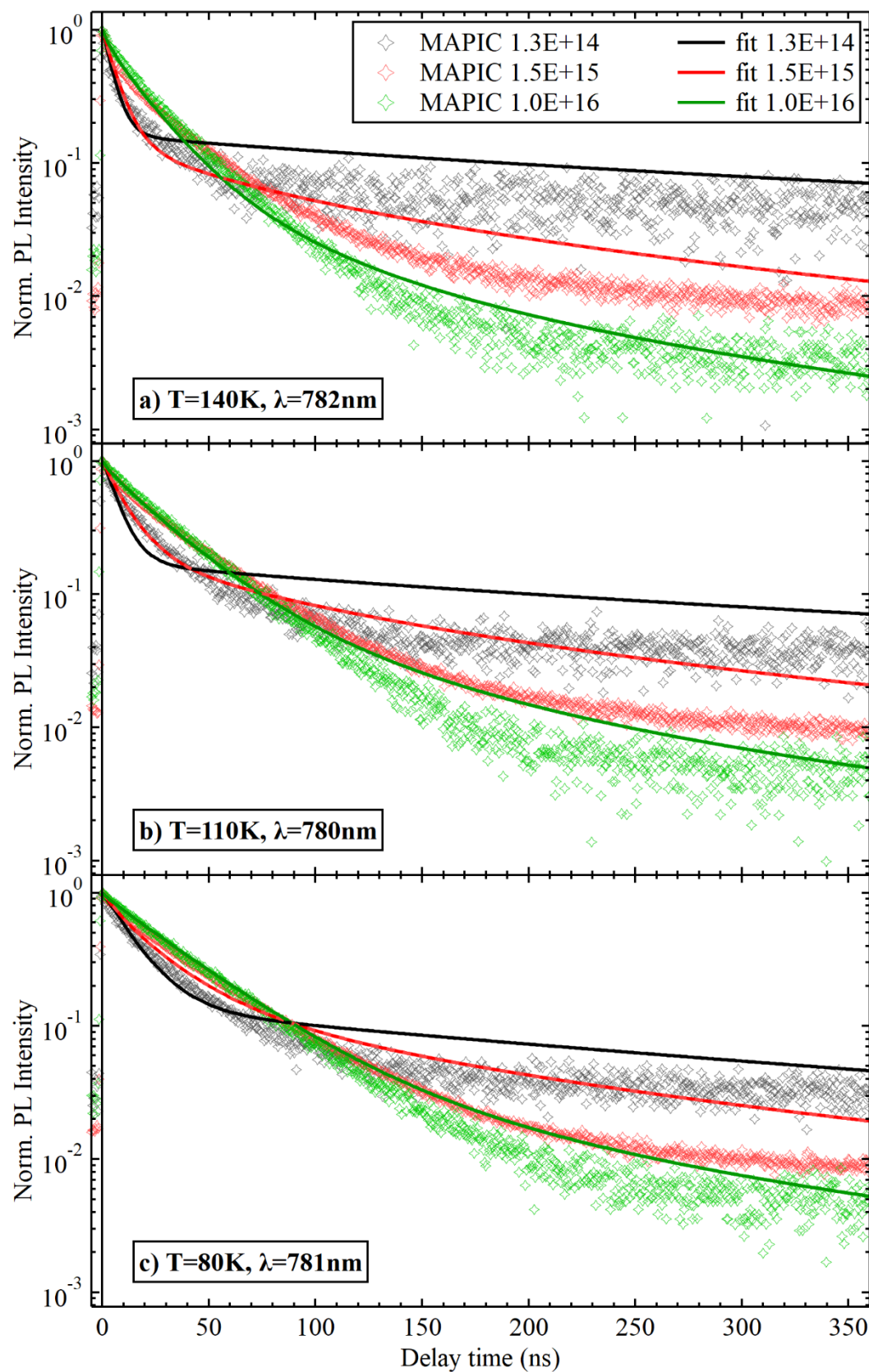


Figure 6-6: Normalised TRPL spectra of the tetragonal peak. High temperature phase range.



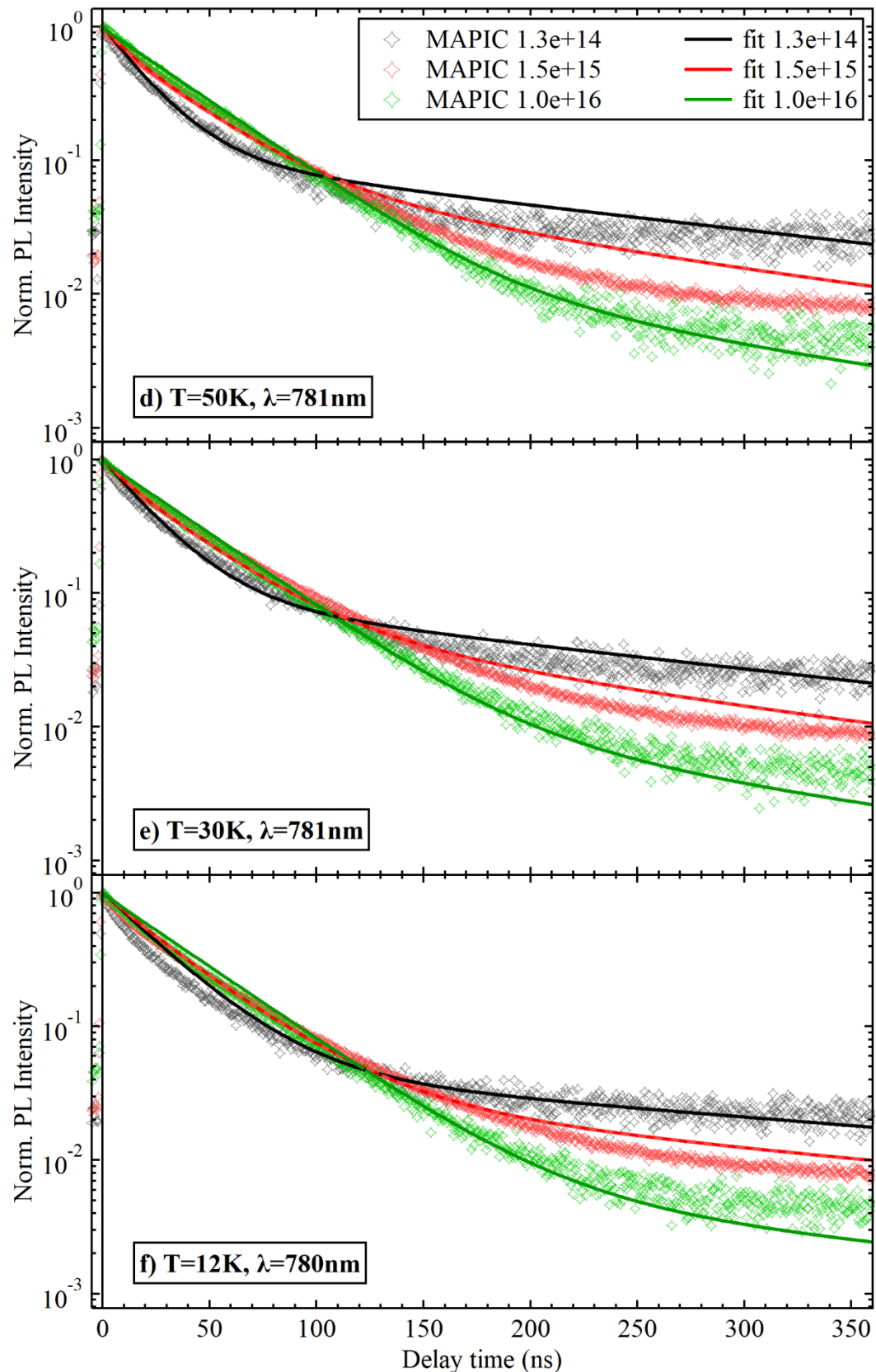


Figure 6-7: Normalised TRPL spectra of the tetragonal peak. Low temperature phase range.

Table 6-1 reports the results of the fitting for the low energy peak:

k_{eh}^0	$3.5 \cdot 10^{-7} \text{ cm}^3 \text{ s}^{-1}$	\mathbf{N}^x	see Figure6-9
k_x	$2.5 \cdot 10^7 \text{ s}^{-1}$	ΔE^x	22 meV
r^0	$1 \cdot 10^{-4} \text{ s}^{-1}$	E_{barr}^x	0.9 meV
\mathbf{N}^e	see Figure6-9	E_{esc}^x	0 meV
ΔE^n	42 meV	From the previous fitting:	
E_{barr}^n	0.9 meV	E_{ph}	10 meV
E_{esc}^n	2.6 meV	E_b	see Figure4-3

Table 6-1: Results of the global fit for the tetragonal peak.

As mentioned above the values for the phonon energy is used with the fitted values describing the trap levels depth and barrier in order to obtain the rates k_1^n , k_2^n and k_3^n for the electronic transitions and k_1^x , k_2^x and k_3^x for the exciton transitions. The temperature dependence of these rates is shown in Figure 6-8. The temperature dependence of k_{eh} was calculated from the fitting parameter k_{eh}^0 and is presented in Figure 6-8b.

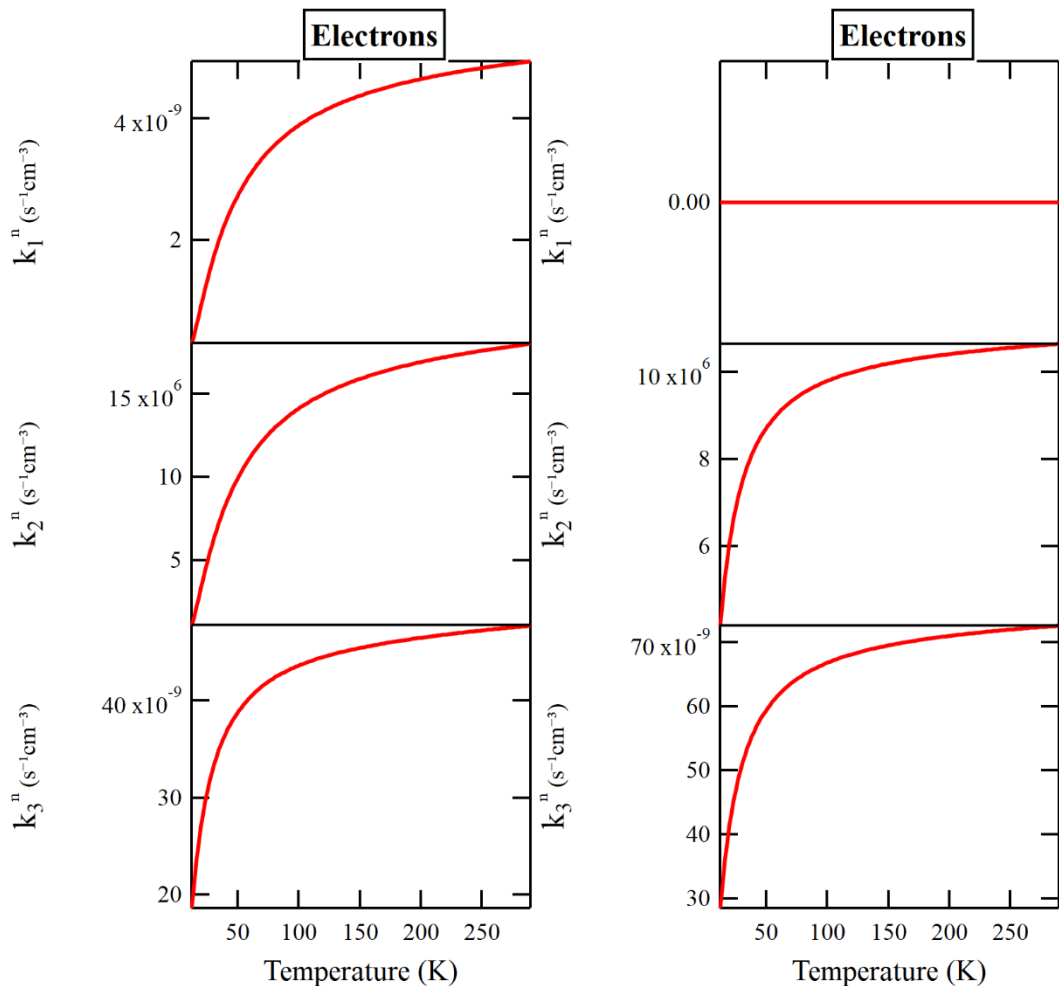


Figure 6-8: Fitted temperature dependence of trap capture rate, trap re-excitation and trap depopulation for electrons and excitons for the tetragonal phase.

The fitted values for the densities of electronic and excitonic traps are depicted in Figure 6-9. At room temperature the extracted values are $N_{290}^n = 3.12 \cdot 10^{15} \text{ cm}^{-3}$ and $N_{290}^x = 2.50 \cdot 10^{15} \text{ cm}^{-3}$. As the temperature is decreased the number of electronic traps increases until the temperature reaches 140K. As the temperature further decreases and the sample enters the range where both the tetragonal and orthorhombic phases coexist, the electronic density drops from $6.52 \cdot 10^{15} \text{ cm}^{-3}$ at 170 K to $3.12 \cdot 10^{15} \text{ cm}^{-3}$ at 140 K, and then linearly decreases to the value of $1.52 \cdot 10^{15} \text{ cm}^{-3}$ at 12 K. We interpret the behaviour of the electronic trap density as a consequence of the phase transition. On the other side the exciton density shows a monotonic decrease as the temperature of the sample is lowered

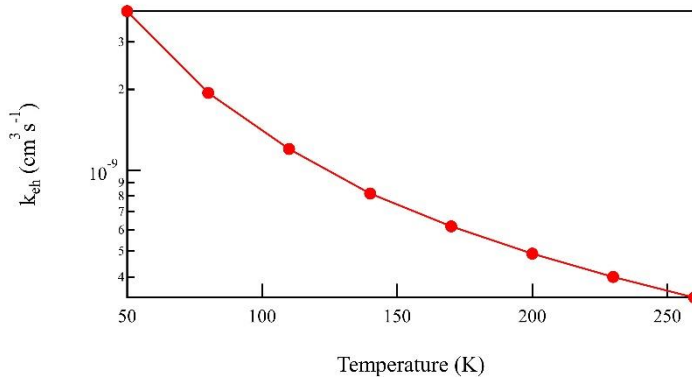


Figure 6-8b: Temperature dependence of the bimolecular recombination rate calculate using the fitted value k_{eh}^0 and equation 6-13.

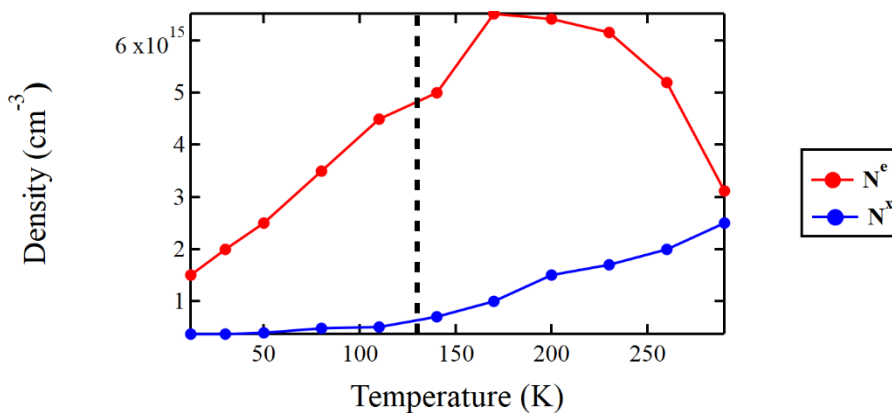
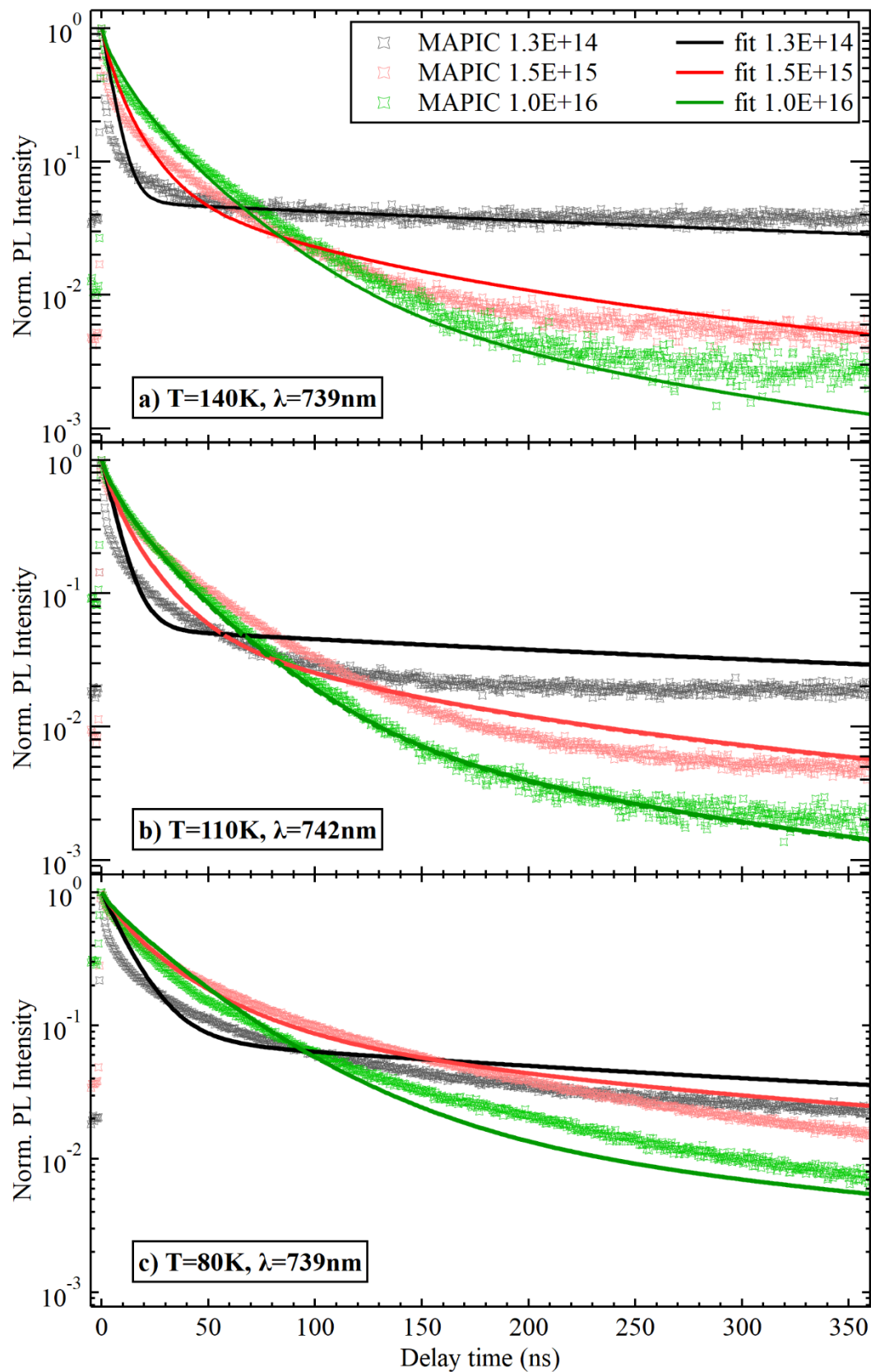


Figure 6-9: Fitted electrons (red) and excitons (blue) trap densities as a function of T for the tetragonal peak. It's clear the influence of the phase transition between orthorhombic and tetragonal on the densities for temperatures above 140K.

6.4.2 Orthorhombic phase

The high energy peak appearing for temperatures below the phase transitions has been attributed to the NBEPL of the orthorhombic crystal structure of MAPI. Figure 6-10 shows the time-resolved PL decays as a function of the three excitation fluencies in the low temperature range. The fitted values differ from the one obtained for the tetragonal peak. In particular, both electron and exciton trap levels have a smaller energy difference from their excited. At the same time the energy barriers that the particles have to overcome to fall into the traps have also smaller values.



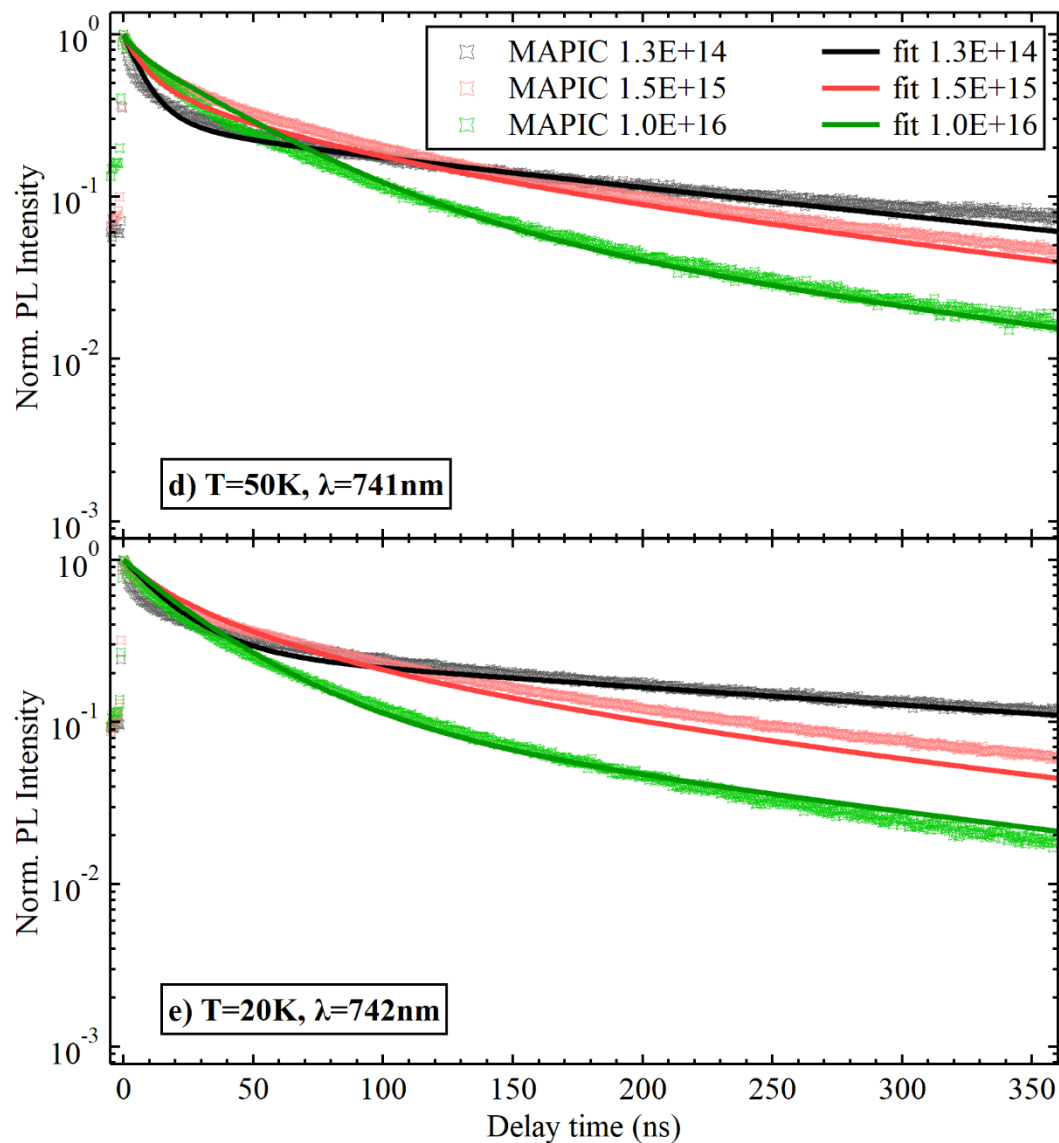


Figure 6-10: Normalised TRPL spectra of the orthorhombic peak.

Table 6-2 reports the results of the fitting for the high energy orthorhombic peak:

k_{eh}^0	$1.15 \cdot 10^{-7} \text{ cm}^3 \text{ s}^{-1}$	N^x	see Figure6-12
k_x	$2.5 \cdot 10^7 \text{ s}^{-1}$	ΔE^x	18 meV
r^0	$1 \cdot 10^{-4} \text{ s}^{-1}$	E_{barr}^x	0.2 meV
N^e	see Figure6-12	E_{esc}^x	0 meV
ΔE^n	23 meV	From the previous fittings	
E_{barr}^n	0.7 meV	E_{ph}	10 meV
E_{esc}^n	0.4 meV	E_b	see Figure4-3

Table 6-2: Results of the global fit for the orthorhombic peak.

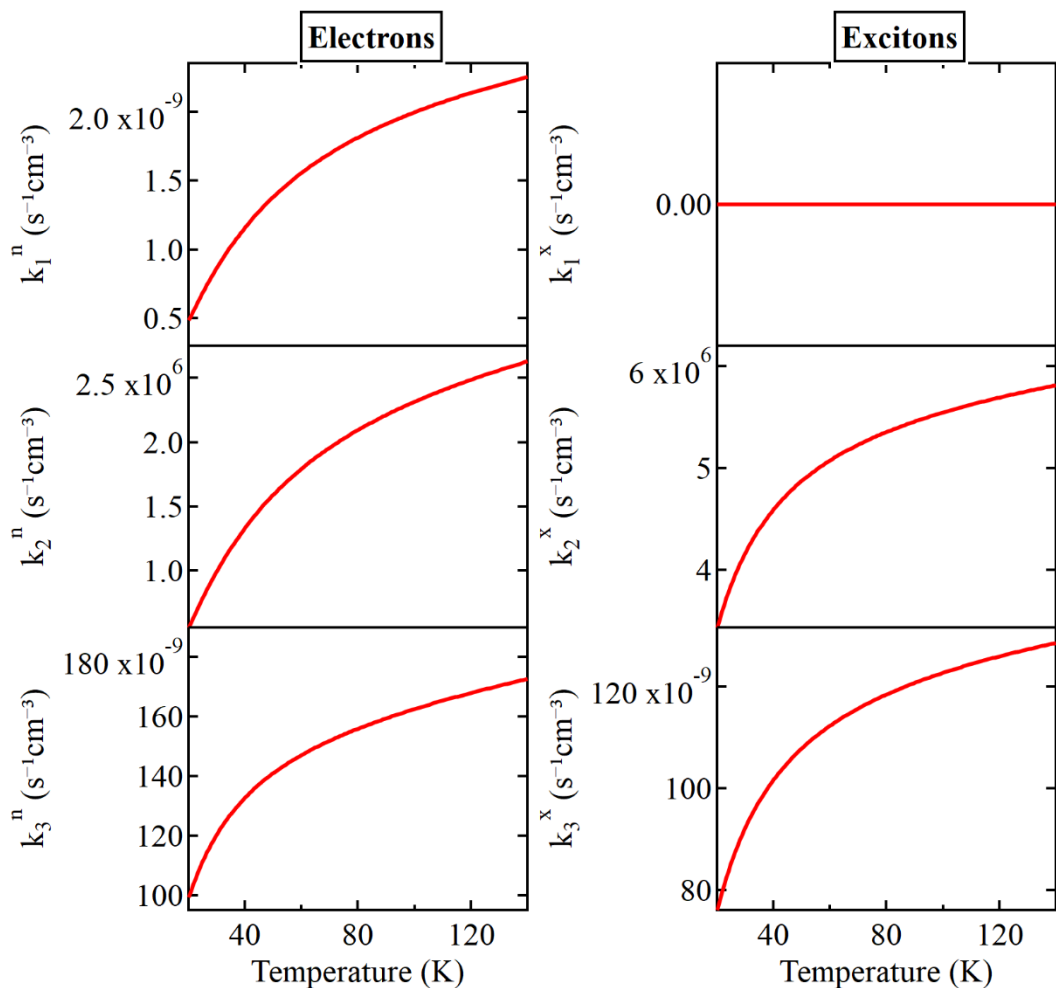


Figure 6-11: Fitted temperature dependence of trap capture rate, trap excitation and trap depopulation for electrons and excitons for the tetragonal phase.

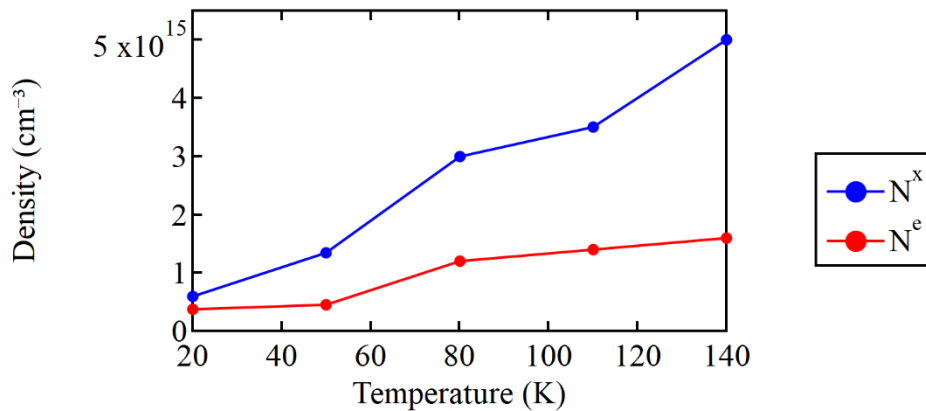


Figure 6-12: Fitted electrons (red) and excitons (blue) trap densities as a function of T for the orthorhombic peak.

6.4.3 Influence of T and $N(0)$ on the decay dynamics.

One of the advantages of our approach is that the solution of the ODE system allows us to examine at the same time the populations of the carrier species. This allows us to draw some deeper consideration into the dynamics involving the various species and energy levels.

The relative densities of electrons and holes are dictated by the Saha equation. The high temperature decays are dominated by electron dynamics. The effect of the presence of the traps on the TRPL spectra is substantially due to two competitive mechanisms, the trapping of the electrons from the conduction band and the detrapping of these trapped electrons into the conduction or the valence band. The result of the first mechanism on the time dependence of the spectra is the fast component of the dynamics dominating approximately the first 25-30 ns of the decay. The different dynamics observed as a function of the excitation fluence at high temperatures strongly depend on the occupation level of the trap states. At the lowest experimental excitation fluence ($N(0) \approx 1 \cdot 10^{14} \text{ cm}^{-3}$), at the maximum point the traps are only 1% filled. As the fluence is increased the traps start to be more efficiently filled, this can be seen in Figure 6-13 by comparison between the black red and green dashed curves.

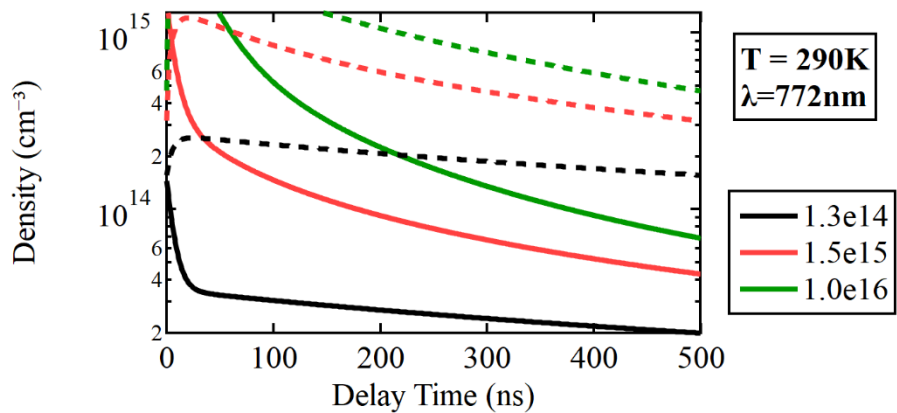


Figure 6-13: Delay time dependence of free and trapped electrons at room temperature for the tetragonal peak emission, for different excitation densities. Solid lines represent the free electron density in the conduction band and dashed lines represent the trapped electron density in the trap state.

The decay channel responsible for the trapping has a rate proportional to $(N^e - n_T)$, and therefore this value will decrease as the excitation power is increased, since n_T is smaller for lower excitations while N^e is constant. This explains how for higher excitation densities the initial fast component of the decay becomes less marked as a function of the laser power. The dynamics at later decay times (25-30 ns onward) can be described as an interplay between bimolecular recombination, excitation of the trapped electrons into the conduction band and recombination of trapped electrons with holes in the valence band. It is possible to see again how the variation of the excitation density influences the dynamics. Since detrapping into the conduction and recombination into the valence band are proportional to n_T , lower laser powers will lead to a slower decay compared to the one observed for higher powers. This effect is combined with the dependence of the bimolecular recombination on the product of the electron and hole densities, $n \cdot h$. To illustrate this, we plotted in Figure 6-14 the temporal evolution of the product $k_{eh}nh$ for the three experimental laser powers, as obtained when keeping the density of and exciton equal to zero.

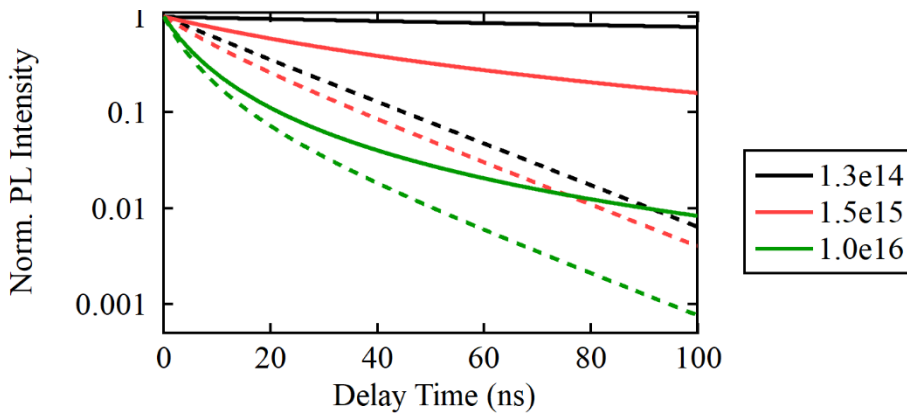


Figure 6-14: Bimolecular recombination for not doped and doped systems at different excitation densities. The effect of the photo-doping on the bimolecular recombination is showed by comparing the case of $n_T=0$ (solid lines) and $n_T=5e15\text{cm}^{-3}$ (dashed lines).

First, we imposed the additional condition that $n_T = 0$ leading to $n=h$ (solid lines in Figure 6-14), and successively we used a value of $n_T = 5 \cdot 10^{15}\text{cm}^{-3}$ (dashed lines in Figure 6-14). We point out how in the latter the tail of the decay shows a deviation from the “pure” bimolecular behaviour. The presence of trapped electrons results in an effective photodoping of the number of holes in the valence band, so that the trap rich samples will show a significant deviation, as the factor $k_{eh}nh = k_{eh} \cdot n \cdot (h + n_T) = k_{eh} \cdot (n^2 + n \cdot n_T) \gg n^2$. For temperatures down to 200 K, we found that the free carriers are still the dominant species ($n/N(0) > 80\%$). At the same time in this temperature range the rates k_1^n, k_2^n and k_3^n do not show a significant variation in magnitude, as shown in Figure 6-8a. We then conclude that the differences observed in the temporal evolution of the PL observed in this range are almost entirely due to the variation of the number of traps per unit volume. Figure 6-15 illustrates this for $N(0) = 1.3 \cdot 10^{14}\text{cm}^{-3}$, when the effect is more pronounced for the reasons explained above.

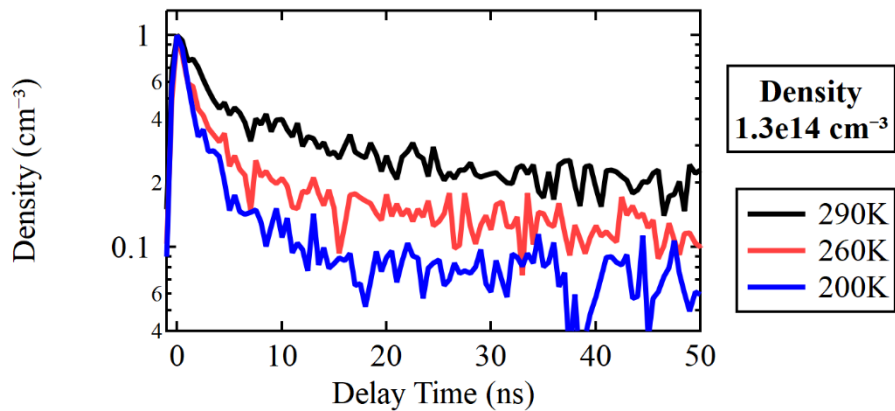


Figure 6-15: Time-Resolve PL spectra of MAPI recorded at 290, 260 and 200K showing the fast component of the decay. The component of the decay ascribed to electron trapping increase as the temperature of the film decrease, as a result of the variation of the electron trap density N^e .

It is evident how the initial fast component of the decay becomes faster as the temperature of the sample decreases. Since again the fast component can be ascribed to the product $k_1^n(N^e - n_T)$, the increasing value of the trap density N^e with decreasing temperature reported in Figure 6-9 determines the increase in the product above, and as a consequence the acceleration of the fast initial component of the decay.

Figure 4-10 shows how below $T = 140K$ there is not a clearly dominating charge species for the exciton binding energies calculated through Elliott's theory, as we demonstrated in Section 4.2. This results in a regime where the recorded temporal dependence of the decays depend on the interplay between free charges and exciton dynamics. As an example, we show in Figure 6-16 a comparison between n and x for $T = 140K$ for all three excitation carrier densities.

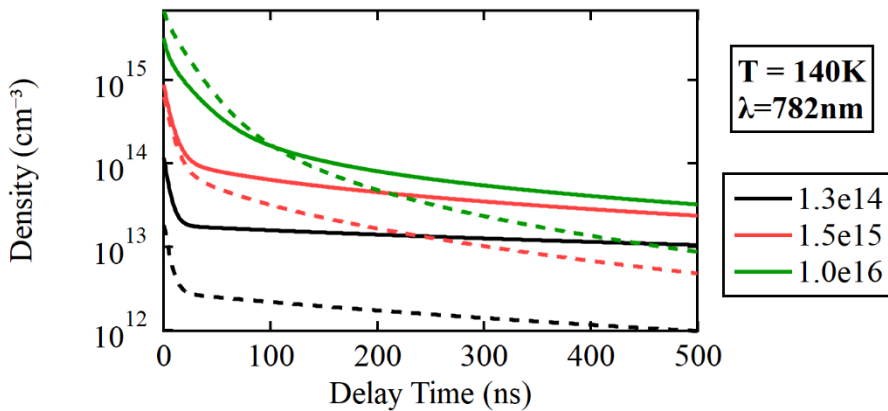


Figure 6-16: Electron and exciton densities as a function of the carrier excitation density for $T=140K$. Electron densities (solid lines) and exciton densities (dashed lines) are compared for the fitted results for the tetragonal emission as a function of the three experimental excitation densities.

This figure gives a good representation of the interplay between temperature and excitation density effects. For $N(0) \approx 10^{14} \text{ cm}^{-3}$ the free electron-hole pairs represent roughly 90% of the photogenerated charges but for higher laser intensities the concentration of electrons and excitons are of the same order of magnitude. Finally, the green curves, corresponding to $N(0) \approx 10^{16} \text{ cm}^{-3}$, show that at zero delay time the exciton density is approximately two times larger than the electron density. However, as the carriers recombine, due to the effect of the traps, the ratio between the two species is overturned. The decays dynamics for the temperatures of 170, 140 and 110 K can then only be described as a superposition of electron-holes pair and exciton dynamics.

For temperatures below 110 K, our analysis suggests that excitons are above 90% of N for any excitation density $N(0)$. Therefore, we expect the TRPL experimental spectra to strongly reflect this fact. The densities of free and trapped excitons as a function of delay time for the three laser powers and calculated for $T=30K$ are shown in Figure 6-17.

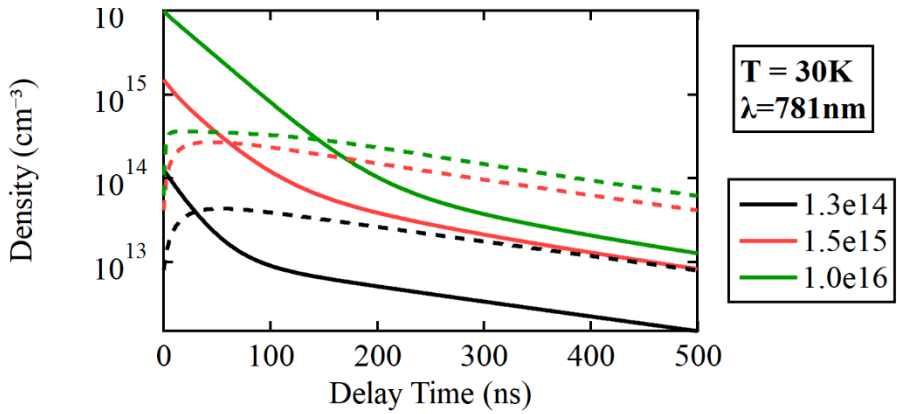


Figure 6-17: Delay time dependence of free and trapped excitons at room temperature for the tetragonal peak emission, for different excitation densities. Solid lines represent the free exciton density in the bright state and dashed lines represent the trapped exciton density in the trap state.

By observing at Figure 6-7 it is evident how in this low temperature regime the rates k_1^x and k_2^x decrease compared to their values in the high temperature regime, leading to a slower population and depopulation of the excitonic trap states and furthermore the depopulation rate vanishes, i.e. $k_3^x = 0$ according to our fit. This results in the fact that the depopulation of the traps will tend to be relevant at later delay times at lower temperatures compared to higher ones. In the example in Figure 6-17 the occupancy x_T relative to $N(0) \approx 10^{16} \text{ cm}^{-3}$ (green dashed line) appears to be almost constant up to 200 ns and then exhibits a slow decrease for delay times longer than 200ns. Comparing x_T with x for the same laser power, we observe also that immediately after the laser pulse the number of free excitons is higher than the corresponding number of trapped ones. Let us consider the competition between the respective terms $k_x x$, $k_1^x (N^x - x_T) x$ and $k_2^x x_T$, describing recombination, trapping and re-emission of excitons between bright, trap and ground states. When the traps are filled, $k_1^x (N^x - x_T) x \ll k_x x$, and the dominant term will be the exciton recombination, in perfect agreement with the mono-exponential decay of the TRPL for high fluences at low temperatures, resulting in a straight line on the semi-logarithmic plot (green lines in Figure 6-6 c-f). At later decay times the exciton population in the bright state drops below the value of x_T . This results in a slow net flow of trapped excitons into the upper energy

level, because in this regime $k_2^x x_T > k_1^x (N^x - x_T)x$. The excitons that are then re-excited into the bright state can recombine radiatively or again become trapped into the trap state. The latter will then again be re-excited giving origin to a cyclic process. Since the rate at which the excitons are promoted from the trap state into the bright one is slower than the recombination rate k_x , the first process will limit the overall decay. This is the origin of the effect of delayed luminescence that can be observed as a slow component in the time-resolved decay, for delay times longer than approximately 200 ns.

6.5 Conclusions

The results presented in the previous section show that the temperature and fluence dependence on the observed decay dynamics can be modelled by the system presented at the beginning of this Chapter (Figure 6-2). The low energy peak observed in the temperature map of MAPI polycrystalline thin film can be assigned to the NBEPL of the material in its crystalline tetragonal phase. One single set of fitting parameters has been calculated allowing us to describe the observed TRPL spectra over the full experimental temperature range. The model took into account for each parameter it is temperature and excitation density dependence, so that the variation of the parameters was expressed as a function of T and N . The only exception to this was found to be the density of the trap states, which does not seem to follow any clear dependence with temperature.

Similarly, the high energy peak visible for $T < 140\text{K}$ was attributed to the NBEPL of the orthorhombic phase. A different set of fitting parameters was necessary to fit the whole decay dynamics.

Chapter 7 **Low-dimensional emissive states in non-stoichiometric methylammonium lead halide perovskites**

7.1 **Introduction**

Most of the possible compounds belonging to the class of materials of hybrid organic-inorganic perovskites share a very wide range of desirable properties for a variety of optoelectronic applications, from light emitting devices [77] to photodetectors [78], and solar cells [79]. These properties include high absorption, long carrier diffusion length, ease and low cost of fabrication, mass-production scalability and independence from scarcely available materials. On the other hand, a large portion of these perovskites also share characteristics that limit their impact as a reliable active medium in the optoelectronic applications mentioned above. In particular one of the most known problems is degradation when perovskites are exposed to combinations of environmental factors like ultraviolet light, heat, oxygen and moisture [21], [80]–[82]. Therefore, a significant proportion of the actual research is addressing this series of limitations. If one route is perfecting the encapsulation system to isolate the perovskite active material from degrading agents, another approach has been to find alternative perovskites compositions and structures that are less sensitive to aging. Using this second approach, various groups demonstrated how the incorporation of 2D layers into 3D perovskite materials results in photovoltaic devices that retain their performance efficiency even after one year of operation [83]–[85]. Furthermore, quasi-2D perovskite crystal structure showed improved stability and moisture tolerance when used in solar cells [86].

The terms 2D and quasi 2D perovskite refer to a system where the crystal structure of a 3D-parent perovskite of the form ABX_3 is interrupted along one of the crystallographic axes by a spacer layer that substitutes one or more crystallographic planes [87]. If n defines the number of stacked octahedral perovskite layers that are

confined between two spacers planes, then for $n=1$, the structure is called pure 2D and quasi-2D if n is greater than 1. The case in which $n \rightarrow \infty$ will produce a bulk 3D perovskite. Additionally, the intercalating layers can act as insulating barriers resulting in the natural formation of quantum wells [88], [89] that allow the formation of stable excitons with binding energies around 200 meV [90]. The electronic band gap reduces as a function of increasing n and it has been attributed to reduction in quantum confinement [91], [92]. The pure 2D perovskites therefore exhibit the widest band gap [93]. This class of compounds take the name of low dimensionality perovskites (LDPs).

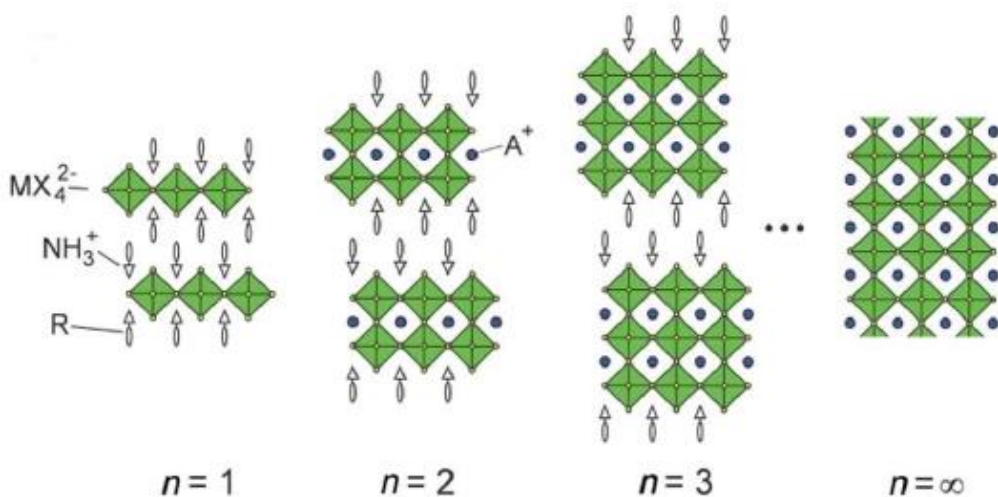


Figure 7-1: Crystal structure for $n=1,2,3$ and ∞ perovskites from a parent ABX_3 structure (from reference 84).

These structures can be obtained by replacing the cation in crystallographic position A with another cation (C) having a larger ionic radius. This substitution can result into a structure that exceeds the Goldschmidt's tolerance factor and therefore the interruption of the continuous lattice [94], [95]. Depending on the number of larger cations that lie in the insulating region the stoichiometry and the electronic properties of the LDP change. When only one cation is present the structure is described by the formula $CA_{n-1}B_nX_{3n+1}$ and takes the name of Dion-Jacobson perovskite. A second class is characterised by the presence of two cations in the spacing layer, therefore having formula $C_2A_{n-1}B_nX_{3n+1}$ and is called Ruddlesden-Popper perovskite. LDPs perovskites can easily be prepared by partial or complete

substitution of the A cation, usually methylammonium (CH_3NH_3^+), with larger organic cations in the precursor solution [88], [96]. Typical examples of the substituting cation are phenethylammonium ($\text{C}_8\text{H}_9\text{NH}_3^+$), butylammonium ($\text{CH}_3(\text{CH}_2)_3\text{NH}_3^+$) [93] hydrophilic amphiphiles ($\text{R}-\text{NH}_3^+$) [97] and 3-(aminomethyl)piperidinium [98]. The spatial separation and the number n of the perovskite layer can be adjusted by simply controlling the ratios of the cations A and C in the precursors solution. Furthermore, it has been found that a mixture of two alternating cations A and A' exhibit a LDP structure with $n = 0, 1, 2$ and 3 [99]. In these compounds the two different cations alternate in the interlayer space and result in cation ordering leading to LDPs having properties being a blend of the chemical formula of Ruddlesden-Popper perovskites with the structural features of Dion-Jacobson perovskites.

Interestingly, previous reports indicated the presence of LPD formations in non-stoichiometric MAI:PbI₂ blends, together with the presence of other phases [100]. A series of works also highlighted the benefits of adding excess of PbI₂ and MAI on the device performance due to grain boundary passivation [101], enhancement of the short circuit current of solar cells [102] or moisture tolerance [103].

Lidzey and his co-workers carried on similar studies on non-stoichiometric perovskite films investigating on the cell performance, stability and overall photophysical properties. During these studies they found that excess-MAI films showed photoluminescence emission similar to the one observed from LDPs, leading to a deeper investigation into their crystallographic properties by grazing incidence wide-angle X-ray-scattering (GIWAXS). Together with this work of characterization, the photophysics of the system has been examined with a range of spectroscopic techniques that include optical absorption, photoluminescence emission (PLE) along with steady-state and time-resolved photoluminescence emission. In this chapter we will report on the emission photoluminescence properties of thin films of MAI:PbCl₂ with precursors molar ratios of 2.5:1, 3:1 and 3.5:1. These analyses are part of a collaboration with Dr Benjamin George Freestone and Prof David Lidzey from the University of Sheffield. In Section 7.2 we will briefly describe the preparation methods and the topographical and

structural analysis of these perovskites. In the following section photoluminescence excitation spectroscopy and photoluminescence mapping will be presented. The experimental data and their analyses in these sections have been carried out by our collaborators at the university on Sheffield. Finally, in Section 7.4, we will present the results of the steady state and time-resolved photoluminescence analysis.

7.2 Samples preparation, topographical and structural analysis

Thin films of non-stoichiometric MAPIC perovskites were prepared starting from different dry-ingredient molar ratios of their precursors MAI and PbCl_2 . A series of samples having an excess organic halide material was obtained with a MAI: PbCl_2 ratio of 2.5:1. Another series of samples were prepared with a 17% stoichiometric excess of MAI by mixing the precursors in a 3.5:1 proportion. Finally, a reference MAPIC perovskite film was obtained from the concentrations 3:1. All films were deposited on a PEDOT:PSS/ITO substrate using a hot-cast technique.

Figure 7.2 shows atomic force microscopy and scanning electron microscope images of the samples produced from the three different solutions.

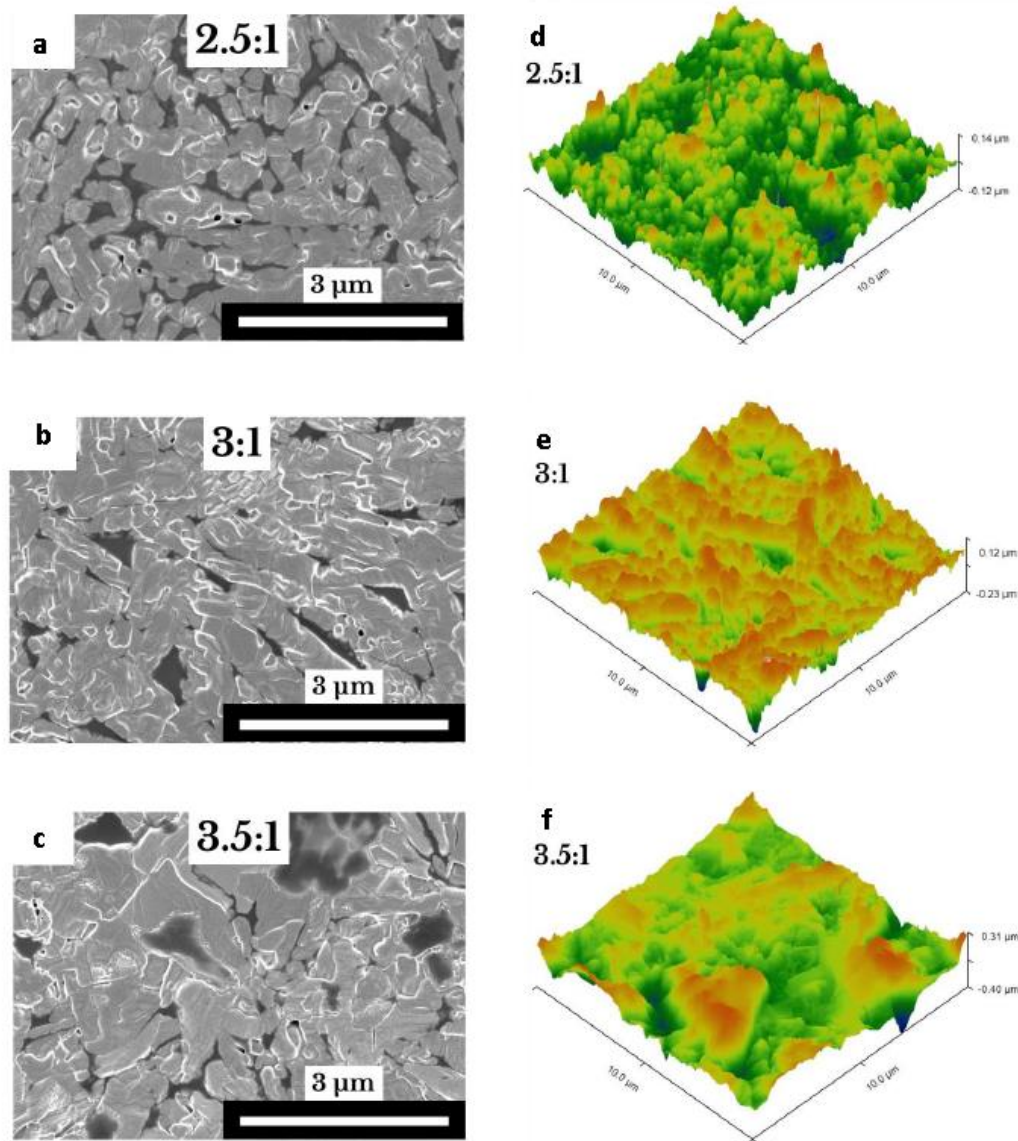


Figure 7-2: Scanning microscope images and atomic force microscopy images for the samples 2.5:1, 3:1 and 3.5:1 (Courtesy of Ben Freestone).

It can be seen that all the perovskites films formed are high polycrystalline in nature. The SEM images of the 2.5:1 film show how this ratio corresponds to the film with the smaller surface coverage and the highest density of -pinholes. From AFM images it is possible to extract a thickness of 260 nm on average and observe that this perovskite film is characterized by the smaller domain size. The reference film exhibits a superior surface coverage and crystallite size with fewer defect regions while the AFM images reflect a higher surface roughness and film thickness. Finally, the 3.5:1 perovskite presents good surface coverage and low densities of

defects, with flatter crystal zones having lengths in the order of 1 μm . The film roughness and thickness are further extended as the content of MAI in the solution is increased. An insufficient quantity of MAI can be responsible for unreacted precursors in the film, therefore resulting in large defect regions and formation of PbI_2 crystallizing in domains. As the content of MAI is increased the abundance of methylammonium and iodine results in a more homogeneous bulk MAPI perovskite with fewer defects and domains containing unreacted precursors. As the percentage of PbI_2 is further reduced in the 3.5:1 samples, regions containing a high percentage of organic material can be expected to appear in the film, and they can be identified with the dark areas in Figure 7.2 (c). The increase in grain size with increasing MAI concentration in the precursors is probably due to a more efficient growth of perovskite crystals during the annealing process (see Section 3.4).

A combination of crystallographic analysis techniques has been utilised to recognise the phases present in the films and determine their structures and purity. In particular films obtained from the 3.5:1 solution were prepared by annealing in air and inside a glove box filled with nitrogen. These analyses lead to the conclusion that a tetragonal MAPbI_3 phase, observed in the reference film, is also present in both the non-stoichiometric samples. Furthermore, in the 3.5:1 samples a LDP consistent of lead-halide octahedral planes with a d-spacing of 21.67 \AA was identified.

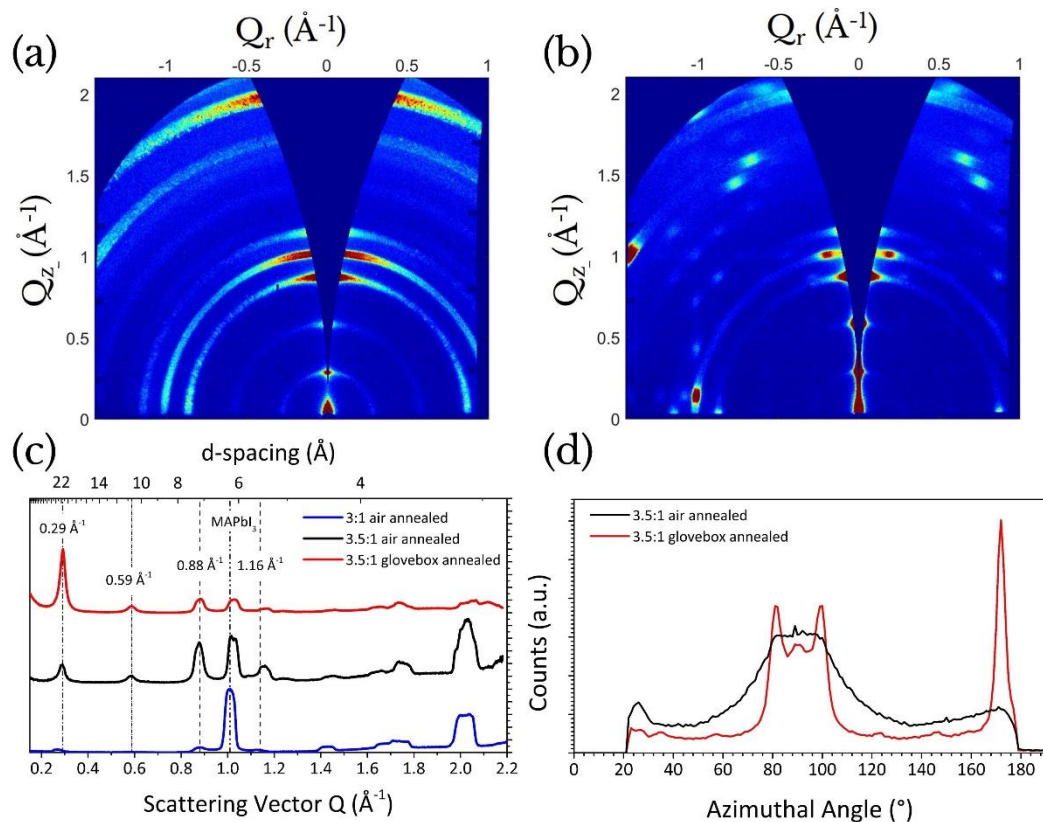


Figure 7-3: GIWAS detector patterns from air annealed (a) and nitrogen annealed (b) 3.5:1 samples. Radial integration of three 3.5:1 samples (c) and azimuthal integration around Q for glove box and air annealed 3.5:1 samples (d) (Courtesy of Ben Freestone)

Figure 7.3 highlights some of the main results obtained with GIWAS with incident wavelength of 0.134 nm at an angle of 0.3° , corresponding with a penetration depth of 150 nm and a Q-space range between 0.05 and 2.5\AA^{-1} [104]. The reflection at $Q \sim 1 \text{\AA}^{-1}$ was consistent with the (002)/(110) plane in the bulk perovskite phase. Its presence in the film formed in excess of MAI suggests the presence on a 3D bulk perovskite content. These features exhibited a shift to higher Q values for the 3.5:1 films, suggesting a compression of the perovskite lattice. From the comparison of the integrated curves in Figure 7.3 c it was possible to notice the appearance of additional reflections at 0.29 , 0.59 , 0.88 and 1.16\AA^{-1} . These features have been identified respectively as the first, second, third and fourth order reflection due to the above-mentioned d-spacing of 21.67\AA of the lead-halide octahedral planes of the LDP phase. The possibility of these reflections to be due to additional phases

due to monohydrate and dehydrate perovskites has been excluded by the annealing process, that has previously been found to be sufficient to remove such structures [105]. Figure 7.3 d shows the strong modulation in the azimuthal reflection intensity connected to a higher preferential alignment found in the glove box annealed sample, that has been interpreted as the indication of a more phase pure film in the case of annealing in nitrogen environment [106].

The possible crystal structure has been simulated by our collaborator Dr Benjamin George Freestone with density functional theory (DFT) calculations and compared with the radially integrated GIWAXS patterns. The superposition of the pattern for the 3.5:1 sample with a simulated pXRD pattern for a $\text{MA}_4\text{Pb}_3\text{I}_{10}$ structure is shown in Figure 7.4 b. The similarity shown with the calculated structure for $\text{GA}(\text{MA})_n\text{Pb}_n\text{I}_{3n+1}$ perovskite calculated by Soe et al. has been taken as a further indication that the fabricate thin films present the crystal structure similar in nature to the DJ/RPP hybrid class of perovskites having MA^+ cations placed in the spacer layer [99].

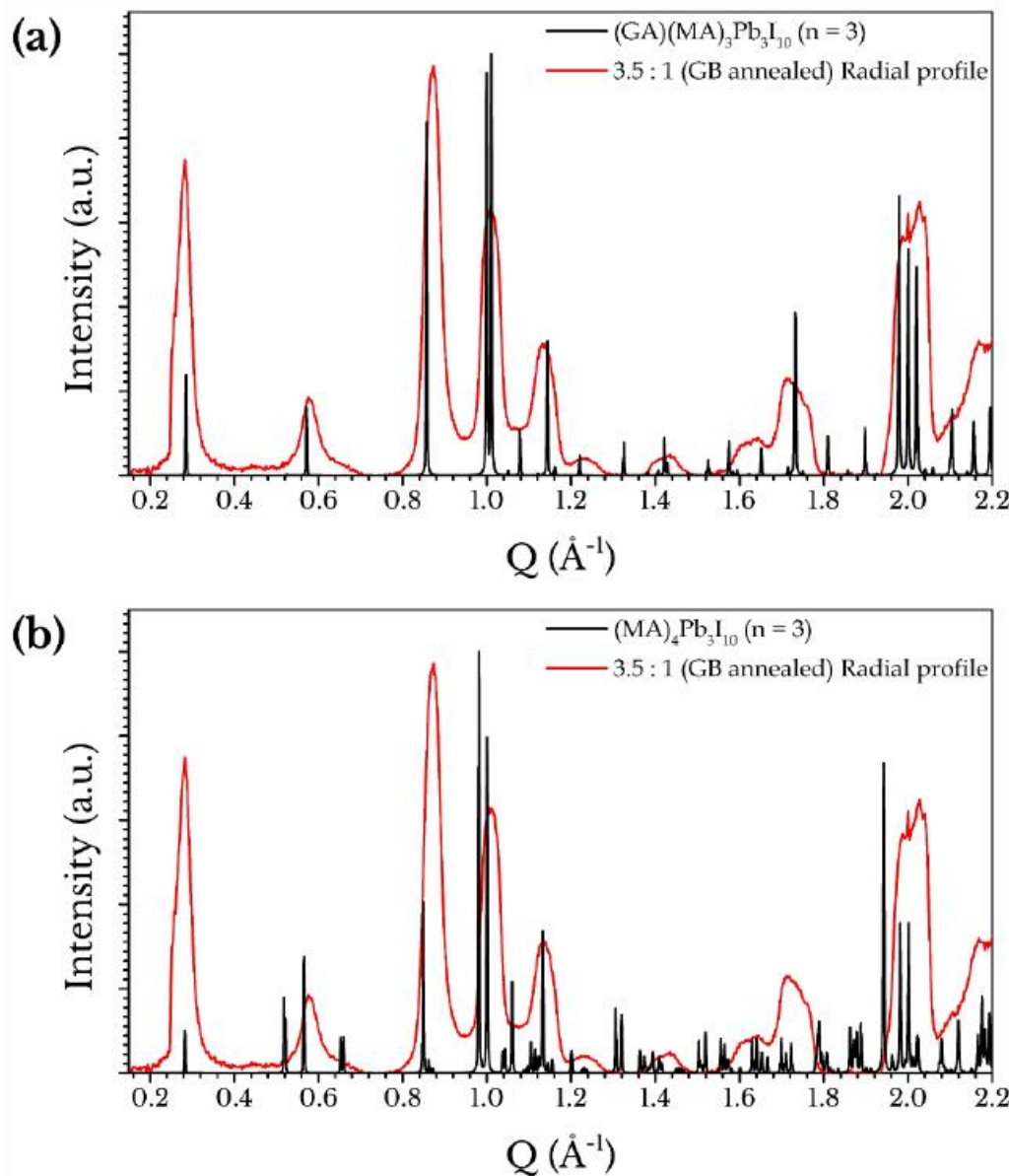


Figure 7-4: Simulated powder-XRD patterns and radially integrated GIWAS for 3.5:1 glove box annealed sample (Courtesy of Ben Freestone).

The resulting structure $\text{MA}_4\text{Pb}_3\text{I}_{10}$ is a $n = 3$ perovskite that adopts the triclinic P1 space group with unit cell parameters of $a = 6.47 \text{ \AA}$, $b = 12.56 \text{ \AA}$ and $c = 23.23 \text{ \AA}$, which it is schematically shown in Figure 7-5.

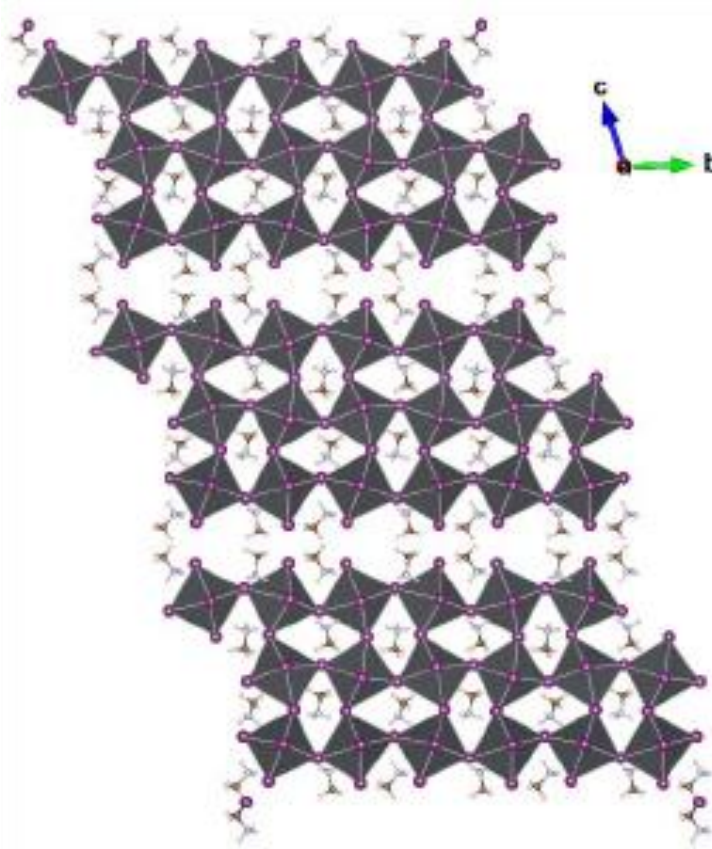


Figure 7-5: Model structure representation of the quasi 2D perovskite structure (Courtesy of Ben Freestone). The coordination octahedra formed by the iodine ions (purple spheres) around the Pb atom (inside the grey octahedra) are organised in layers with $n=3$. The large MA ion (represented by the organic chain) are present at the centre of the triclinic cell, in their classic position A, and they also form the separation layer that interrupts the bulk perovskite crystal, allowing the formation of the quasi-2D structure.

7.3 Steady-State Photoluminescence Properties

In order to validate the conclusion made by our collaborators and reported in the two previous paragraphs, we performed a series of spectroscopic measurements aiming to probe the coexistence of 3D and lower dimensionality methylammonium halide perovskite phases in the non-stoichiometric films. Thin films from precursor solutions having molar ratios 3:1 and 3.5:1 were prepared by Ben Freestone at the

University of Sheffield and we recorded steady state luminescence and time resolved luminescence as a function of temperature. An excitation of wavelength equal to 400 nm was used to excite the sample and the ssPL and TRPL spectra were recorded as described in the experimental section (Chapter 3).

At room temperature the PL emission from the reference perovskite film consist of two close emission peaks centred at 763 and 740 nm (Figure 7.5). The global maximum (763 nm) is consistent with the near band edge emission commonly observed for the tetragonal phase of $\text{MAPbI}_{3-x}\text{Cl}_x$ [107]. Interestingly, the PL emission spectrum at low temperature (12K) reported in Figure 7.6 a (dashed line) consists of a single emission peak red-shifted by 9 nm and therefore centred at 772nm, suggesting the absence of a low temperature emission associated with the orthorhombic crystalline phase, as observed in the samples fabricated and studied in Chapter 4, 5 and 6. We noted in the previously studied samples a blue-shift associated with the appearance of a second emission peak at the tetragonal to orthorhombic phase transition around 130 K. The second less intense peak is visible at room temperature and its origin is more uncertain. A similar emission peak has previously been ascribed to the presence of PAPbI_3 nanocrystals [10]. A progressive blue-shift has been observed upon reduction in dimensionality from bulk perovskites to nanometre sized perovskite nanoparticles, and therefore we suppose that this emission can be ascribed to very small regions of 3D perovskite that are unable to crystallize in micrometre size grains [10], [92], [108], [109]. The absorption spectrum measured at 290 K for the same film (red line in Figure 7.6 a) show a band-edge at 758 nm, corroborating the results found from the phase analysis of an almost pure bulk perovskite being fabricated from the non MAI-abundant solutions.

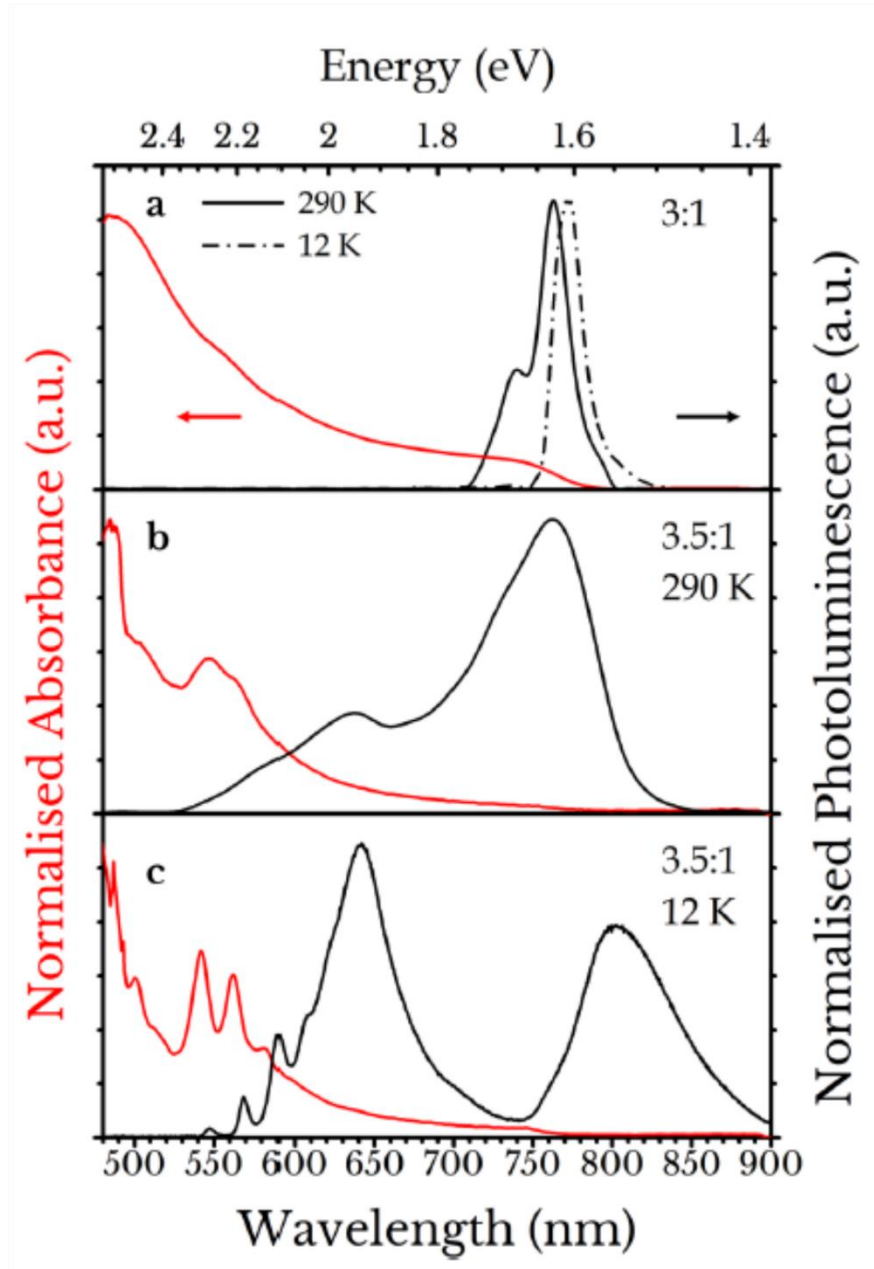


Figure 7-6: Absorption and ssPL spectra for reference and 3.5:1 sample at room temperature and 12 K.

Figure 7.6 highlights how the spectral emission features of the non-stoichiometric perovskites are characterised by a superimposition of emissive states associated with the bulk perovskite phase and other emissive states of higher energy. In panel b in Figure 7-6 it is possible to see the plot of the normalised PL emission and normalised optical absorption of a 3.5:1 air annealed perovskite sample, recorded at 290 K. The PL spectrum, when compared to the reference film, demonstrates the

appearance of broad emissions at shorter wavelengths. At the lowest temperature measured (Figure 7-6 c), the emission in the wavelength range below 750 nm appears spectrally resolved in five or six different maxima. In a similar way, the absorption spectra consist of a broad unresolved band centred around 550 nm together with a band edge at 760 nm for the high temperature measurement. As the temperature is reduced, the broad absorption appears to be the sum of contribution from peaks centred at 582, 562, 542, 515 and 500 nm, and they seem to mirror the emission peaks in the same spectral region. We note that the band edge blue-shifted to approximately 750 nm. Overall, the observed absorption and emission spectra for the 3.5:1 perovskite resembles those observed in quasi-2D and mixed quasi-2D/3D system, therefore being a further proof of the formation of lower dimension phases in the studied perovskites [87], [110]–[112].

In order to have a better understanding of the emission properties of the mixed bulk-2D perovskites, a set of PL spectra were recorded for each of the non-stoichiometric samples and compared with the 3:1 reference film. The samples were prepared as previously described on a ITO/PEDOT:PSS substrate. The spectrally resolved emission for the reference and the 2.5:1 perovskites for different temperatures in the range 12–290 K are plotted in Figure 7-7. As previously mentioned, an emission peak attributed to MAPI nanocrystals is visible at room temperature (peak labelled as *a* in Figure 7-7), and its relative intensity compared to the main tetragonal NBEPL emission is reduced as the temperature is decreased. Below the tetragonal to orthorhombic transition (120 K in Figure 7-7) a second emission maximum centred at 740 nm appears (peak labelled as *b*). We associate this feature with photoluminescence emission from the orthorhombic crystalline phase, in accordance with the results for similar MAPI polycrystalline films studied in Chapter 4, 5 and 6 and observed in other studies [32]. As the temperature is further reduced, the relative intensities of the emission from tetragonal and orthorhombic phases become less and more intense respectively, due to the reduction of the percentage of perovskite that adopts the tetragonal crystal system (see also Chapter 4). For temperatures at the bottom of the investigated range (< 50 K), the high temperature emission cannot be observed anymore. The orthorhombic

photoluminescence peak exhibits a red-shift up to 770 nm, again showing analogies with the previously studied MAPI.

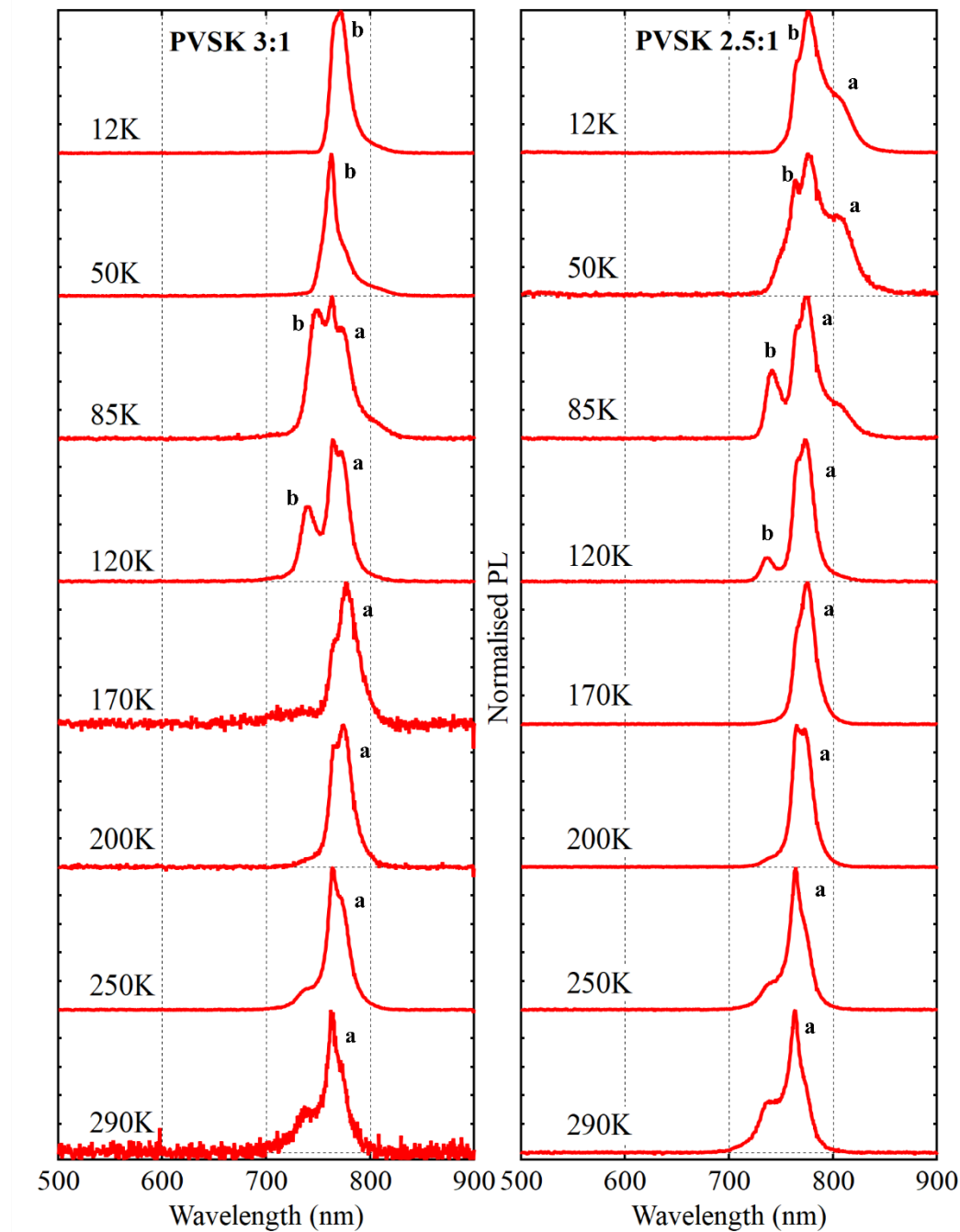


Figure 7-7: Temperature dependent normalized steady state PL from a 2.5:1 and 3:1 film.

The photoluminescence emitted upon excitation at 400 nm from the 2.5:1 sample is shown in Figure 7-7 on the right panel. The emission pattern as a function of

temperature closely resembles the one observed for the reference sample. This further corroborates the analysis reported in the previous section and suggests that a halide rich precursor solution leads to the formation of an emissive bulk 3D perovskite and non-emissive unreacted precursors. A notable difference is the presence of a broad low energy emission peak that appears below the tetragonal to orthorhombic transition temperature. This kind of luminescence has previously been attributed to distributions of emissive sub band-gap states appearing in samples having different concentration of iodine precursors [113]. We observed similar emission peaks at low temperature in MAPIC samples. We conducted a preliminary analysis on the dependence of the emission intensity from the excitation power showing a power law with exponent $k = 1$. Recalling what we reported in Chapter 5, this is consistent with recombination from trapped electrons (see Table 5-1)

Two different LDP samples obtained from MAI excess solution were spin coated with the same hot cast technique on two different substrates, ITO/PEDOT:PSS and bare quartz. The results of the steady state photoluminescence analysis as a function of temperature are visible in Figure 7-8. Both series are characterised by the presence of a sequence of higher energy emissive states and one or more lower energy peaks that we associate with the 3D perovskite near band edge emission. On the other hand, a particularly different behaviour is evident between the emission from the films deposited on the different substrates.

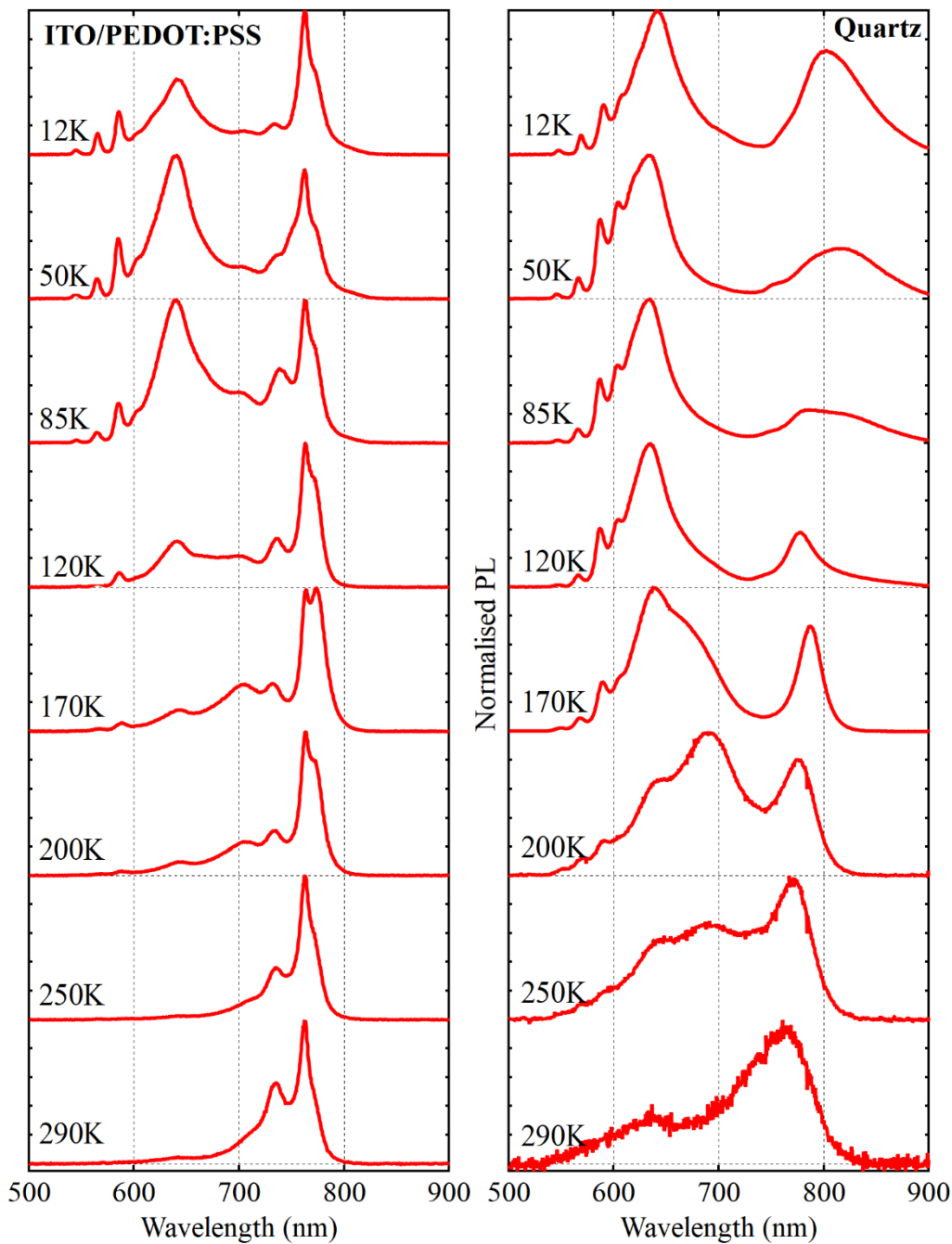


Figure 7-8: Temperature dependent normalised steady state PL from a 3.5:1 film deposited on PEDOT:PSS and deposited on quartz.

We first consider the long wavelength part of the spectra, corresponding to the near band edge emission from 3D MAPI. In the case of the ITO/PEDOT:PSS substrate (left panel in Figure 7-8) the spectral shape of the photoluminescence seems to match the one observed for the reference sample. It is possible to observe, at room temperature, that the tetragonal emission is centred around the same wavelength

(762 nm) and undergoes the same red-shift as the temperature is decreased. The higher energy maximum appears at slightly lower wavelength, 732 nm versus 737 nm, suggesting the formation of smaller nanoparticles compared to the reference solution. Additionally, the relative intensity of the two peaks suggests the presence of a higher quantity of nanoparticles in the MAI abundant sample. As the temperature is reduced below the phase transition, the low temperature phase PL is observable at 737 nm, but the presence of the LDP states makes the identification of this peak more problematic. When the 3:1 solution is deposited on a quartz substrate instead, the low-energy part of the spectra appears to be dominated by a very broad peak, presumably from the bulk perovskite crystals. At room temperature the maximum of the PL is positioned at 762 nm, consistent with all the other samples. We suppose that this corresponds to an overlap of the bulk perovskite with the MAPI nanocrystals discussed above [109]. Furthermore, it red-shifts by 24 nm in total as the temperature approaches the tetragonal to orthorhombic transition. Below the phase transition temperature ($T \leq 120$ K in Figure 7-8) it is not possible to clearly distinguish two separate maxima corresponding to the tetragonal and orthorhombic NBEPL, but instead it presents a single broad emission peak initially blue-shifted to 776 nm. As the temperature is further reduced it is red-shifted and considerably broadened. We again suppose that the observed broad maximum is due to the overlapping of the narrower peaks observed in the reference and in the ITO deposited samples. The broadening of the emissions can be explained with a larger presence of sub-band states in the latter sample. We infer that the deposition on the quartz substrate leads to a more defect-rich film compared to the ITO/PEDOT:PSS, and as consequence, to the observed broadening of the characteristic NBEPLs [113]. This observation is also consistent with the presence of the long tail observable between 800 and 900 nm at low temperatures, likely to be ascribed to emissive sub band gap states.

Finally, we consider the series of emission characteristics present in the higher energy part of the spectra. The first observation we make on the normalised spectra is that the relative intensities show how the low dimensionality emissive states dominate the emission of the sample spin coated on quartz, while they represent a much smaller component in the sample deposited on PEDOT:PSS. The

photoluminescence across the whole temperature range is dominated by a strong emission peak centred between 635 and 640 nm. This emission seems to be quite consistent across the entire temperature range. We speculate that this can be the result of a process of charge transfer between the perovskite MAPI phase and surface states that exists at the interface between 3D and 2D domains. A further confirmation of this assumption comes from the comparison between films cast from 3.5:1 solution annealed in air (red line), 3.5:1 annealed in nitrogen (black line) and a 4:1 ratio film annealed in air (blue line) are shown in Figure 7-9.

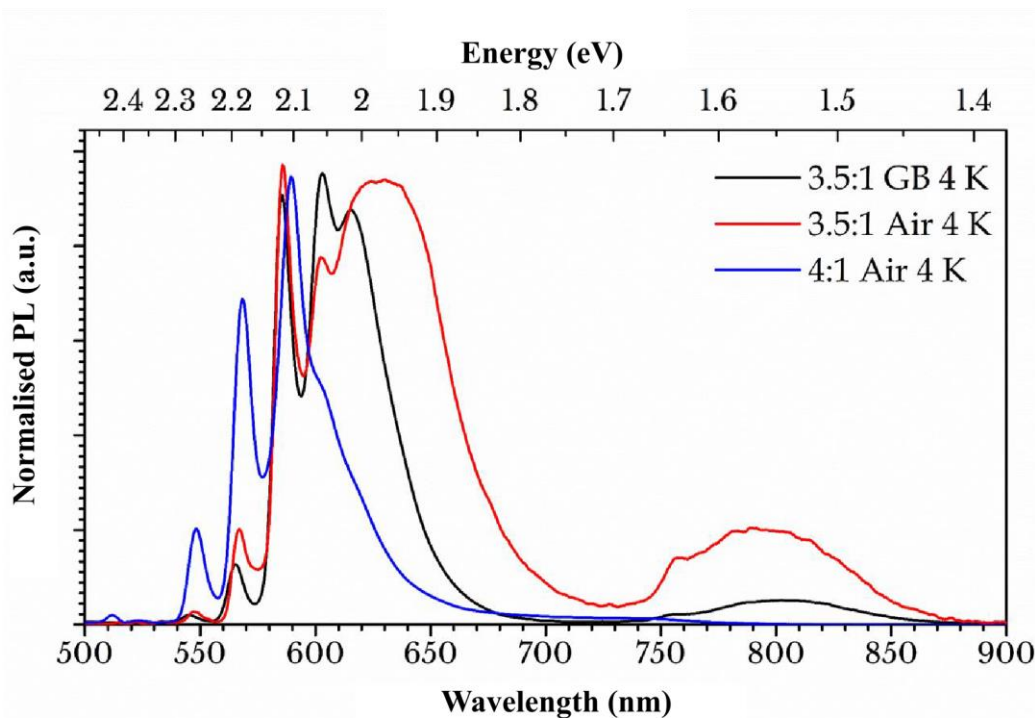


Figure 7-9: Normalised steady state PL from 3.5:1 films deposited on PEDOT:PSS annealed on nitrogen, air and from a 4:1 film.

Comparing the three samples, it is possible to see how the emission at 640 nm is drastically quenched in the sample annealed in the glove box compared to the sample annealed in air, and even more in the film deposited from the solution having higher MAI concentration. At the same time this quenching effect can be observed on the peak attributed to the near band edge photoluminescence of the bulk phase. This reduction in PL intensity of the lower energy peak indicates that both the annealing in nitrogen atmosphere and higher concentrations of MAI inhibit

the formation of the 3D MAPI material in the film. The reasons behind the suppression of the bulk phase in the 4:1 sample it is still unclear, but the data in Figure 7-9 seem to suggest that the formation of 2D or quasi-2D states is enhanced by the excess of MA^+ cations, despite the formation energies of these LPDs is higher compared to the ones relative to the formation of the bulk phase [114], [115]. The effect of the different annealing atmosphere, however, could be explained with the influence of water vapour on MAI mobility. It has been postulated that the mobility of MAI increases in the presence of water vapour [116]. Higher mobility of MAI could lead to a better redistribution of the ionic constituent across the film and therefore to the formation of bulk MAPI domains. On the other hand, a reduced mobility would result in larger portions of the sample with high MA^+ densities, where the formation of LDPs phases would be facilitated. Furthermore, in the topological and GIWAXS analysis, we observed how nitrogen annealed samples appear to be more phase-pure. This would additionally result in a decrease of the surface states at the boundaries between bulk and lower dimensionality phases, consequently explaining the reduced emission attributed to charge carrier effects.

Another series of features that emerge in Figure 7-8 is represented by a sequence of narrower emission peak comprised between approximately 500 nm and 620 nm. We suggest that these maxima correspond to a series of independent and localised excitonic states. The first reason is the correspondence of these emission peak with maxima in the absorption spectrum (Figure 7-6), presenting the same energetic distance between the peaks. Another observation is that the strong temperature dependence could be proof of the existence of a thermally activated process that result in the dissociation of localised excitons in the 2D and quasi-2D states.

7.4 Time-Resolved Photoluminescence properties

Additional information on the nature of the observed emissive states can be obtained from the study of the decay dynamics of the photoluminescence. We recorded the time resolved photoluminescence spectra in the temperature range between 290 K and 12 K for the 3.5:1 sample. For every temperature considered,

we monochromated the emitted PL in order to resolve the emission of each maximum observed in the correspondent steady state photoluminescence spectrum.

First we consider the time dependence of the emission maxima at lower energy that have been associated with the NBEPL of the bulk perovskite phase, as shown in Figure 7-10. In this figure it is possible to see, for different temperatures across the 12 - 290 K range, the emitted photoluminescence as a function of time for the reference bulk 3:1 sample (left column) and the two 3.5:1 samples deposited on the two different substrates: ITO/PEDOT:PSS (central column) and quartz (right column). It can be seen, comparing the curves in Figure 7-10 to those studied in the previous chapter, that the temperature dependence of the decays for the non-stoichiometric samples closely resembles the one characteristic of the bulk perovskite. This is a further indication of the presence of a bulk perovskite phase in the films prepared from the halide abundant solutions. Due to time constraints, we were not able to perform the same type of global ODE fit performed on the stoichiometric polycrystalline films studied in Chapter 6. This analysis has therefore postponed as future work, as we think that it would be of great interest to observe how the preparation of the perovskite films from non-stoichiometric solutions would impact the charge carriers dynamics in the framework of model we presented in this thesis.

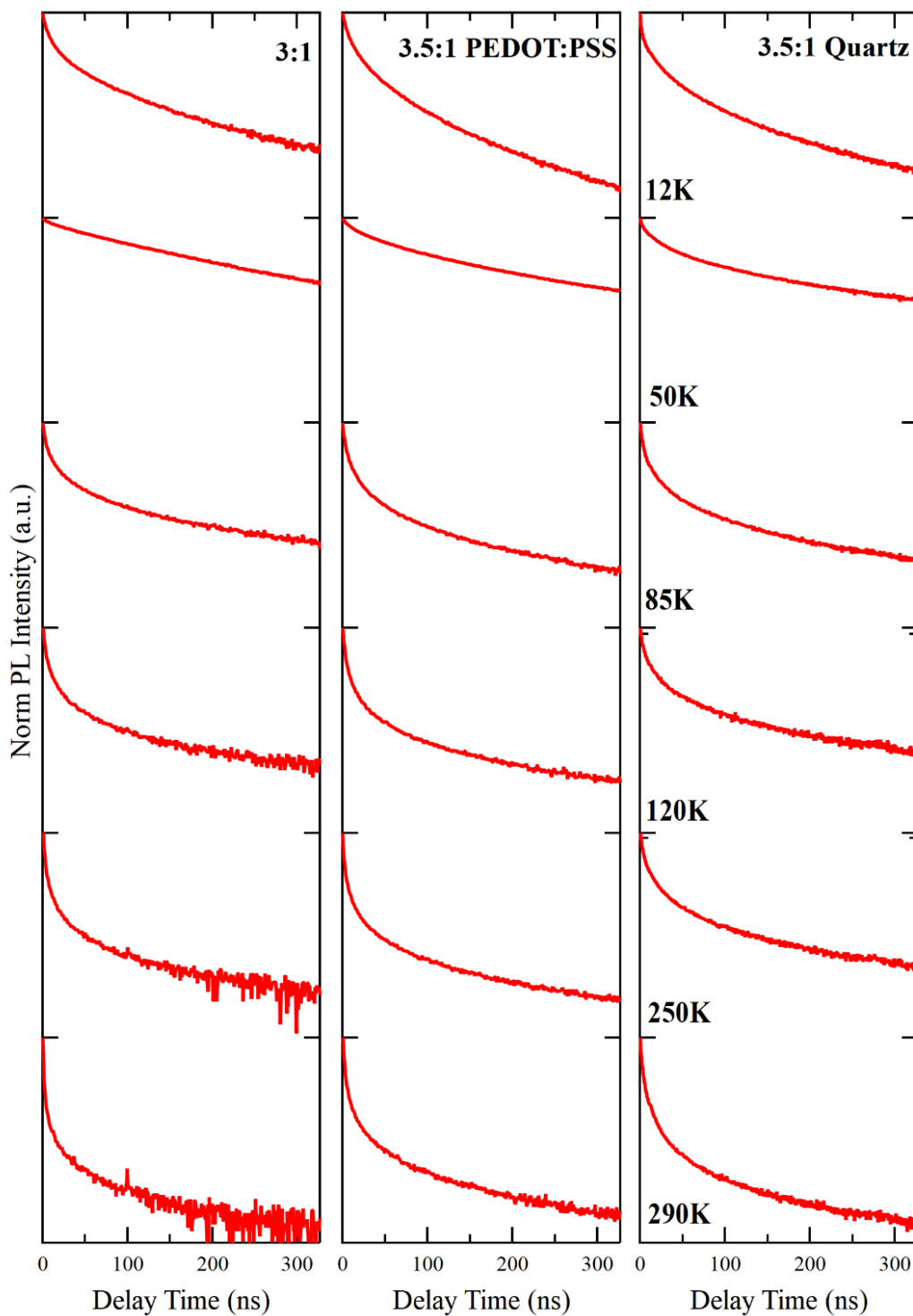
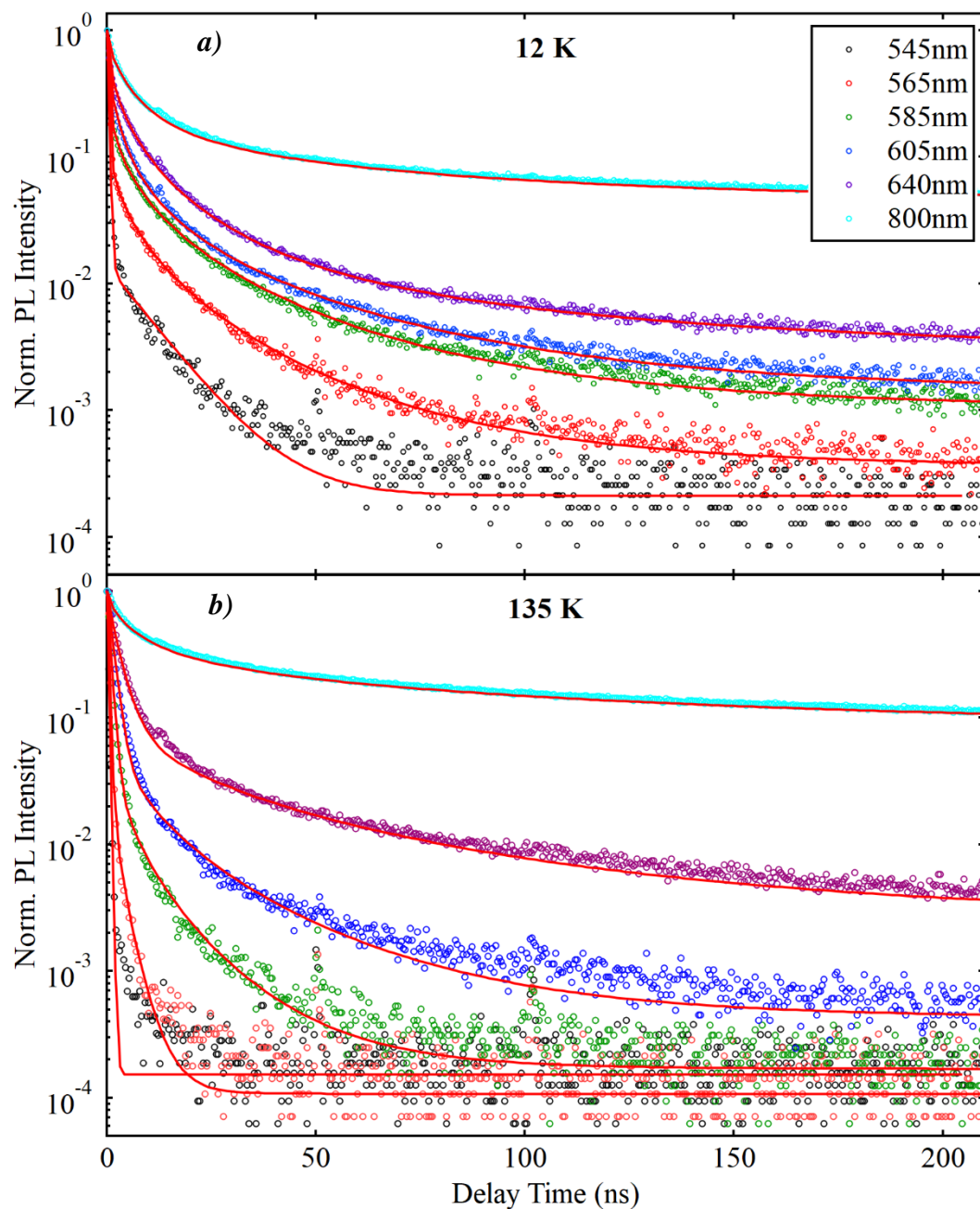


Figure 7-10: Comparison of the TRPL spectra at different temperatures for the lower energy emission of films obtained from non-stoichiometric precursors. Samples were deposited by hot casting on an ITO/PEDOT:PSS (central panel) and a quartz (right panel) substrate. As comparison is reported (left panel) the reference 3D perovskite sample

We consider now the higher energy emission features that we previously attributed to the low dimensionality phases. Figure 7-11 shows an example of the normalised PL decays corresponding to the LDP states, recorded for the 3.5:1 sample on quartz. In the left panels are plotted the emission intensities at function of time, recorded at each wavelength corresponding to the local maxima observed in the steady state spectra, and for the temperatures of 12 and 135 K. A distinctive dependence on the emission wavelengths is evident from the reported example. The same dependence has been observed for each explored temperature. The overall decay time appears to be a monotonically increasing function of the emission wavelength. On the right panel, instead, we plotted the dependence of the decays on the temperature of the sample, for two different emission wavelengths. For each recorded emission the decay time decreases as the temperature of the sample is increased.



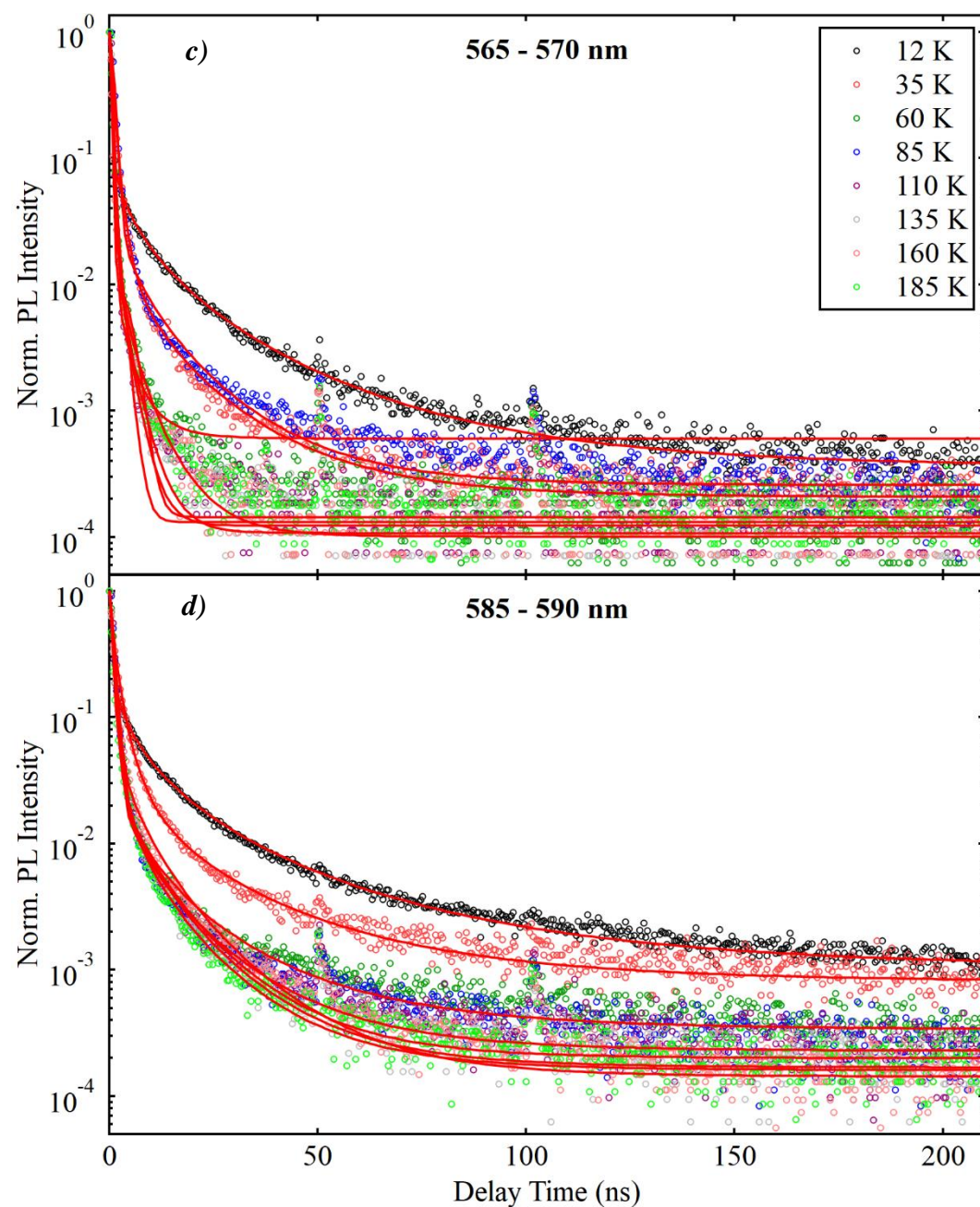


Figure 7-11: Low dimensionality emissive states TRPL spectra of a 3.5:1 film on quartz. Panels a) and b) show the emitted PL as a function of time for isolated detection wavelengths at 12 K and 135 K. Panels c) and d) show the temperature dependence of the time resolved intensity recorded at the wavelength corresponding to the local maxima of the emission. The red solid lines show the fitting of the stretched exponential function.

Instead of the complete rate equation approach adopted in Chapter 5, we will consider a simplified model often used in similar perovskite carrier dynamics studies [117]. The intensity of the emitted photoluminescence as a function of time is described using a stretched exponential function [118], [119]. $I(t) =$

$$I(t) = A_1 e^{-(k_1 t)^{\beta_1}} + A_2 e^{-(k_2 t)^{\beta_2}}$$

Here the measured intensity I at time t is the sum of two decay terms, where A_1 and A_2 are the amplitude constants, k_1 and k_2 are the decay rates and β_1 and β_2 are the stretching factors.

Figure 7-12 reports the decay rates k_1 and k_2 as a function of collection wavelength (a and b) for the 12 and 35 K, and as a function of temperature (c and d) for two fixed collection wavelengths, as obtained from the double stretched exponential fits plotted on the correspondent decays in Figure 7-11.

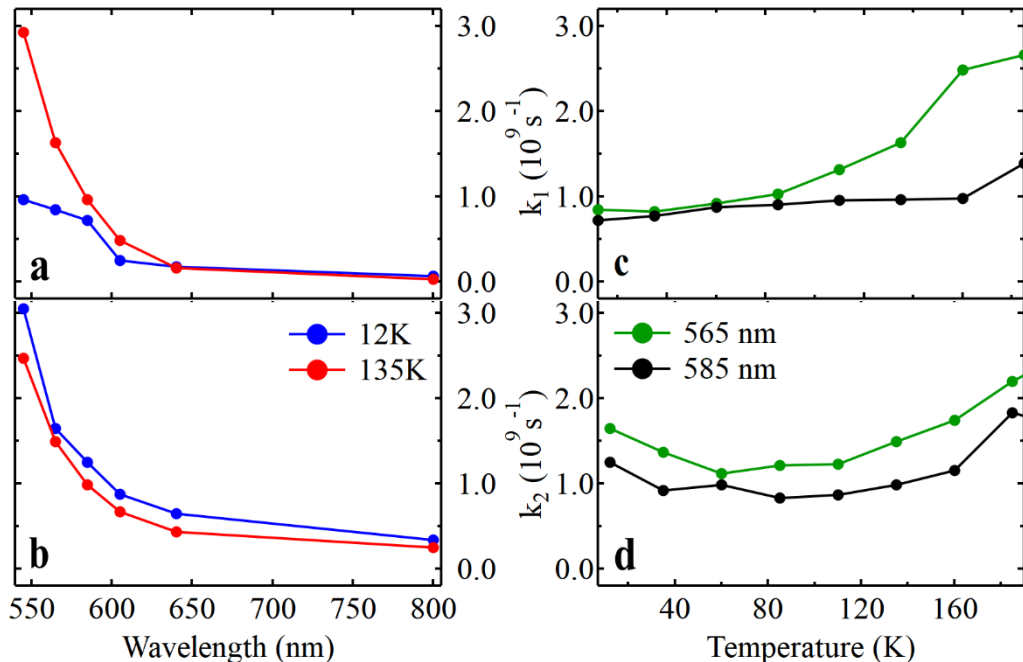


Figure 7-12: Decay rates k_1 and k_2 of double stretched exponential fit for 3.5:1 film on quartz. Panels a and b show k_1 and k_2 as a function of the detection wavelength for the temperatures 12 K and 135 K. Panels c

*and d show the same rates as a function of the sample temperature
for the emission wavelengths of 565 nm and 585 nm*

The higher decay rate, in our case k_2 , corresponds to a smaller decay time, and therefore to a fast component of the decay. We speculate that the lower decay rate k_1 corresponds to a slow component of the decay. Previous works on perovskite carrier dynamics associated the slower decay to the bulk properties of the material, like bimolecular or exciton recombination, and, on the other hand, the fast component to non-radiative recombination due to surface effects and trap states.[117], [120] Panels a and b show how both the decay constants decrease as a function of increasing wavelength. We note here how the decrease of the rate associated with the non-radiative decay channels is consistent with an increase of the intensity of the photoluminescence observed in the steady state spectra (Figure 7-8). The observed decrease of the decay rates can be interpreted as a result of the reduced electron-hole confinement [7], [8]. This correspond to the scenario where the observed features at higher energy are result of excitonic states. States at higher energy seem then to present a higher electron-hole confinement, and therefore perhaps a higher exciton binding energy. Interestingly, the temperature dependence of the rates k_1 and k_2 doesn't exhibit a clear dependence. At the present time we are not sure what is the effect of temperature on the decay rates and therefore more research will be done on this aspect in order to clarify the observed dependences.

Conclusions We studied the structural, morphological and photophysical properties of mixed-halide perovskite containing an excess of methylammonium. We reported that the films deposited by hot cast spin coating were highly polycrystalline, and X-ray scattering spectra revealed the coexistence of a common bulk perovskite phase with different features exclusive of the 3.5:1 samples. Therefore, we simulated scattering patterns showing that the observed features are compatible with a quasi-2D perovskite of the form $(MA)_4Pb_3I_{10}$ ($n = 3$). We observed and recognised by optical spectroscopy analysis the presence of photoluminescence emission from the 3d perovskite phase in all the deposited films. A series of emission features at higher energy were observed in these films, and steady state and time resolved photoluminescence spectroscopy revealed the

excitonic like nature of these features. This is consistent with the presence of a series of low-dimensional states in the quasi-2D perovskite phase of the material.

We want to highlight how the decay dynamics for the three samples, still being very similar, exhibit a series of differences. We suppose that these differences depend on various factors. Therefore, as future work, we think it might be of great interest to apply the techniques developed in the previous chapters, and in particular the modelling of the recombination dynamics from the rate equations, on the NBEPL of these perovskites. As we observed in paragraph 7.2, it's possible to obtain different morphologies for films deposited from different solutions. This can be used as a tool to control the density of surface trap states and then obtain a deeper understanding of the effect of the trapping-detrappling mechanisms that were reported in Chapter 6. Furthermore, the X-Ray analysis suggest that the amount of disorder in the crystalline structure might be different for non-stoichiometric films and therefore it would be possible to study the influence of this parameter on the carrier dynamics.

Chapter 8 Conclusions

To date a vivid and stimulating scientific debate is occurring in the PV community aiming to put together the many pieces of a puzzle that could be a realistic answer to the energy demand of a modern and expanding world. The solution to this problem may come from the capability to find efficient and abundant materials for light harvesting. One of the key aspects necessary to find the best combination of efficiency, module lifetime, up-scalability and low-cost seems to be bound to the need of a deep understanding of the optoelectronic and photo-physical properties of hybrid organic-inorganic perovskites. This class of materials represent in the eyes of the scientific community one of the most reliable candidate to joins Si-based PV in the competition against fossil fuels and non-renewable energy sources. Animated by this purpose, this thesis focused on the construction of a model capable of describing the carrier dynamics of MAPI perovskites polycrystalline thin films, over a wide temperature range and incident excitation fluence spectrum.

We combined a series of spectroscopic experiments and analysis to achieve this goal.

In Chapter 4, we used Elliott's theory to calculate the exciton binding energy from absorption measurements on MAPI solution processed thin films. The exciton binding energy is one of the most crucial properties of a semiconductor material, especially for PV applications. This is because the additional energy needed to dissociate the electron-hole pairs could turn to be a limitation to the efficiency of the charge collection at the electrodes of a solar panel. We used the Saha equation to calculate the ratio between excitons and free carriers.

In Chapter 5 we collected other important information on the nature of the recombination processes by a series of observations on the properties of the steady state photoluminescence. We inferred the presence of two main NBEPL peaks, attributed to the tetragonal and orthorhombic phases of MAPI across the range between 290 and 12 K. Furthermore, from the study of the intensity of the emitted fluorescence as a function of the excitation power, we learned that the mechanisms

Conclusions

of electron and exciton recombination require the presence of intraband states. We demonstrated that these trap states heavily influence the dynamics observed.

In Chapter 6 we formulated a precise model accounting for a series of recombination pathways for electron-hole pairs and excitons alike. We then tested this model with a series of TRPL experiments, and showed that the proposed model is capable of reproducing the full extent of the observed features over the whole temperature and excitation fluence spectrum. We additionally extracted two complete sets of parameters that describe quantitatively the features highlighted by our model. We proved that two different sets of parameters are required to adequately describe the measured NBEPL time evolution of MAPI from both its crystalline phases observed in the temperature experimental range.

Finally, in Chapter 7, mixed quasi-2D/3D perovskite thin films from non-stoichiometric precursors were studied with a combination of topography, X-ray diffraction, steady-state photoluminescence and time-resolved photoluminescence analysis. Upon adding a molar excess of MAI in the precursors solution grazing incidence X-ray scattering highlighted the presence of additional scattering features. Fitting of simulated radial scattering profiles revealed the compatibility of the observed features with a $n = 3$ $(MA)_4Pb_3I_{10}$ 2D-type perovskite. The optical analysis revealed the coexistence of a 3D perovskite phase and a series emissive states characteristic of the low dimensionality phases. These states appears to be consistent with excitonic like processes related to the presence of quasi-2d perovskites in the films.

8.1 Future Work

In Chapter 5 we presented the results of spectroscopy studies of lead halide perovskite thin-films that made us conclude that a coexistence of structural phases in $MAPbI_{3-x}Cl_x$ is present in our samples. It has previously been evidenced that at lower temperatures a mechanism of charge transfer from the orthorhombic to the tetragonal phase is possible [121]. In our studies, interestingly, we do not observe

this kind of feature, suggesting a different behaviour that we attribute to differences in the sample. Our material presents a different morphology compared to the authors referenced, as we were able to observe from the scanning electron microscopy images of the samples. Therefore, we suggest as future case of study to investigate the inter-phase charge transfer at low temperatures, comparing our samples of MAPbI_3 and $\text{MAPbI}_{3-x}\text{Cl}_x$. To corroborate the observation of this phenomena we think it would be beneficial to acquire simultaneous spectrally and time-resolved photoluminescence data. Moreover, we think that this data would help revealing more information on the contributions of excitons and free-carriers to the time-resolved photoluminescence, which would follow therefore the structure of the work presented in Chapter 6.

Furthermore, we recently started to investigate the photoluminescence properties of lead halide perovskite thin films using scanning near-field optical microscopy. At present, only preliminary results have been acquired from this technique and the author and colleagues are in the process of carrying out experiments. Future studies will be performed to investigate the effect of illuminating the films over longer time periods on the nano-scale photoluminescence properties. Moreover, the technique could be extended to record the photoluminescence spectrum and transient decays to assist in the understanding of photophysical processes in lead halide perovskites. The author is currently planning to perform observation of the nanoscale photoluminescence properties the polycrystalline thin films that could reveal the effects of grain boundaries, where surface states and therefore defects and impurities are more likely to be present, therefore affecting the recombination dynamics of this class of materials.

Lastly, the collaborators of the author fabricated and characterised perovskite solar cells hybridised with a blend of CdTe quantum dots in the hole conducting layer. This has been done the framework of a research plan aiming to investigate on the effect of this hybridisation and explore potential processes such as luminescent downshifting, resonance energy transfer, and light scattering. We therefore suggest additional experiments similar to the ones carried in Chapter 6, where the technique utilised to study the carrier dynamics on methylammonium lead iodide perovskite

Conclusions

thin film will be applied to hybridised devices, aiming to therefore understand the influence of the nanoparticles on the carrier dynamics, and finally determine and optimise configurations that should be used to optimise photovoltaic hybrid devices.

Bibliography

- [1] M. M. Lee, J. Teuscher, T. Miyasaka, T. N. Murakami, and H. J. Snaith, “Efficient hybrid solar cells based on meso-superstructured organometal halide perovskites.,” *Science*, vol. 338, no. 6107, pp. 643–7, Nov. 2012.
- [2] H. Zhou *et al.*, “Interface engineering of highly efficient perovskite solar cells,” *Science* (80-.), vol. 345, no. 6196, 2014.
- [3] Z. Cheng and J. Lin, “Layered organic–inorganic hybrid perovskites: structure, optical properties, film preparation, patterning and templating engineering,” *CrystEngComm*, vol. 12, no. 10, p. 2646, Sep. 2010.
- [4] H. Kronmüller and S. S. P. Parkin, *Handbook of magnetism and advanced magnetic materials*. John Wiley & Sons, 2007.
- [5] Z. Ye, Z. Qi, B. Zhang, M. Wang, A. Rahimi-Iman, and H. Wu, “Characterization of an abnormal photoluminescence behavior upon crystal-phase transition of perovskite $\text{CH}_3\text{NH}_3\text{PbI}_3$,” *Phys. Chem. Chem. Phys.*, vol. 17, no. 25, pp. 16405–16411, 2015.
- [6] “Halide Perovskite: Observing Phase Transitions in a Halide Perovskite,” *Edinburgh Instruments*. [Online]. Available: <https://www.edinst.com/phase-transitions-halide-perovskite/>.
- [7] X. Hong, T. Ishihara, and A. V. Nurmikko, “Dielectric confinement effect on excitons in PbI_4 -based layered semiconductors,” *Phys. Rev. B*, vol. 45, no. 12, pp. 6961–6964, Mar. 1992.
- [8] Y. Tabuchi, K. Asai, M. Rikukawa, K. Sanui, and K. Ishigure, “Preparation and characterization of natural lower dimensional layered perovskite-type compounds,” *J. Phys. Chem. Solids*, vol. 61, no. 6, pp. 837–845, Jun. 2000.
- [9] C. Bi *et al.*, “Understanding the formation and evolution of interdiffusion grown organolead halide perovskite thin films by thermal annealing,” *J. Mater. Chem. A*, vol. 2, no. 43, pp. 18508–18514, Nov. 2014.

Bibliography

- [10] F. Zhu *et al.*, “Shape Evolution and Single Particle Luminescence of Organometal Halide Perovskite Nanocrystals,” *ACS Nano*, vol. 9, no. 3, pp. 2948–2959, Mar. 2015.
- [11] T. Zhao, C. C. Chueh, Q. Chen, A. Rajagopal, and A. K. Y. Jen, “Defect Passivation of Organic-Inorganic Hybrid Perovskites by Diammonium Iodide toward High-Performance Photovoltaic Devices,” *ACS Energy Lett.*, vol. 1, no. 4, pp. 757–763, Oct. 2016.
- [12] A. Kojima, K. Teshima, Y. Shirai, and T. Miyasaka, “Novel Photoelectrochemical Cell with Mesoscopic Electrodes Sensitized by Lead-halide Compounds (11),” *Meet. Abstr.*, vol. MA2008-02, no. 1, p. 27, 2008.
- [13] W. Zhang *et al.*, “Highly Efficient Perovskite Solar Cells with Tunable Structural Color,” *Nano Lett.*, vol. 15, no. 3, pp. 1698–1702, Mar. 2015.
- [14] P. Schouwink *et al.*, “Structure and properties of complex hydride perovskite materials,” *Nat. Commun.*, vol. 5, no. 1, p. 5706, Dec. 2014.
- [15] C. G. Bischak *et al.*, “Origin of Reversible Photoinduced Phase Separation in Hybrid Perovskites,” *Nano Lett.*, vol. 17, no. 2, pp. 1028–1033, 2017.
- [16] W. Shockley, H. J. Queisser, and R. Ell, “Detailed Balance Limit of Efficiency of pn Junction Solar Cells,” *J. Appl. Phys.*, vol. 32, p. 510, 1961.
- [17] G. E. Eperon, V. M. Burlakov, A. Goriely, and H. J. Snaith, “Neutral Color Semitransparent Microstructured Perovskite Solar Cells,” *ACS Nano*, vol. 8, no. 1, pp. 591–598, Jan. 2014.
- [18] N. Marinova, S. Valero, and J. L. Delgado, “Organic and perovskite solar cells: Working principles, materials and interfaces,” *Journal of Colloid and Interface Science*, vol. 488. Academic Press Inc., pp. 373–389, 15-Feb-2017.
- [19] C. Wehrenfennig, M. Liu, H. J. Snaith, M. B. Johnston, and L. M. Herz, “Charge-Carrier Dynamics in Vapour-Deposited Films of the Organolead Halide Perovskite $\text{CH}_3\text{NH}_3\text{PbI}_3 - x\text{Cl}_x$,” *Energy Environ. Sci.*, vol. 7, p.

2269, 2014.

[20] M. Soroush and K. Lau, *Dye-Sensitized Solar Cells*, 1st ed. Elsevier, 2019.
ISBN: 9780128145418

[21] S. Luo and W. A. Daoud, “Recent progress in organic–inorganic halide perovskite solar cells: mechanisms and material design,” *J. Mater. Chem. A*, vol. 3, no. 17, pp. 8992–9010, Apr. 2015.

[22] N. J. Jeon, J. H. Noh, Y. C. Kim, W. S. Yang, S. Ryu, and S. Il Seok, “Solvent engineering for high-performance inorganic-organic hybrid perovskite solar cells,” *Nat. Mater.*, vol. 13, no. 9, pp. 897–903, Sep. 2014.

[23] “Igor Pro from WaveMetrics | Igor Pro by WaveMetrics.” [Online]. Available: <https://www.wavemetrics.com/>. [Accessed: 24-Mar-2019].

[24] W. G., W. H. Press, S. A. Teukolsky, W. T. Vetterling, and B. P. Flannery, “Numerical Recipes in Fortran: The Art of Scientific Computing.Numerical Recipes in C: The Art of Scientific Computing.,” *Math. Comput.*, vol. 62, no. 205, p. 433, 2006.

[25] L. M. Herz, “Charge-Carrier Dynamics in Organic-Inorganic Metal Halide Perovskites,” *Annu. Rev. Phys. Chem.*, vol. 67, no. 1, pp. 65–89, 2016.

[26] Y. P. Varshni, “Temperature dependence of the energy gap in semiconductors,” *Physica*, vol. 34, no. 1, pp. 149–154, Jan. 1967.

[27] M. Hirasawa, T. Ishihara, T. Goto, K. Uchida, and N. Miura, “Magnetoabsorption of the lowest exciton in perovskite-type compound (CH₃NH₃)PbI₃,” *Phys. B Condens. Matter*, vol. 201, pp. 427–430, Jul. 1994.

[28] K. Tanaka, T. Takahashi, T. Ban, T. Kondo, K. Uchida, and N. Miura, “Comparative Study in the Excitons in Lead- Halide based Perovskite-type Crystals CH₃NH₃PbBr₃ CH₃NH₃PbI₃,” *Solid State Commun.*, vol. 127, no. 9–10, pp. 619–623, Sep. 2003.

Bibliography

- [29] Q. Lin, A. Armin, R. Chandra, R. R. C. R. Nagiri, P. L. Burn, and P. Meredith, “Electro-optics of perovskite solar cells,” *Nat. Photonics*, vol. 9, no. 2, pp. 106–112, Dec. 2014.
- [30] S. Sun *et al.*, “The origin of high efficiency in low-temperature solution-processable bilayer organometal halide hybrid solar cells,” *Energy Environ. Sci.*, vol. 7, no. 1, pp. 399–407, Dec. 2014.
- [31] T. J. Savenije *et al.*, “Thermally activated exciton dissociation and recombination control the carrier dynamics in organometal halide perovskite,” *J. Phys. Chem. Lett.*, vol. 5, no. 13, pp. 2189–2194, Jun. 2014.
- [32] K. Wu *et al.*, “Temperature-dependent excitonic photoluminescence of hybrid organometal halide perovskite films,” *Phys. Chem. Chem. Phys.*, vol. 16, no. 41, pp. 22476–22481, 2014.
- [33] V. D’Innocenzo *et al.*, “Excitons versus free charges in organo-lead trihalide perovskites,” *Nat. Commun.*, vol. 5, p. 3586, Apr. 2014.
- [34] J. Even, L. Pedesseau, J. M. Jancu, and C. Katan, “Importance of spin-orbit coupling in hybrid organic/inorganic perovskites for photovoltaic applications,” *J. Phys. Chem. Lett.*, vol. 4, no. 17, pp. 2999–3005, 2013.
- [35] Y. Yamada, T. Nakamura, M. Endo, A. Wakamiya, and Y. Kanemitsu, “Photoelectronic responses in solution-processed perovskite $\text{CH}_3\text{NH}_3\text{PbI}_3$ solar cells studied by photoluminescence and photoabsorption spectroscopy,” *IEEE J. Photovoltaics*, vol. 5, no. 1, pp. 401–405, Jan. 2015.
- [36] M. Saba *et al.*, “Correlated electron-hole plasma in organometal perovskites,” *Nat. Commun.*, vol. 5, no. May, p. 5049, 2014.
- [37] Y. Yang *et al.*, “Observation of a hot-phonon bottleneck in lead-iodide perovskites,” *Nat. PHOTONICS* /, vol. 10, p. 53, 2016.
- [38] R. J. Elliott, “Intensity of optical absorption by excitons,” *Phys. Rev.*, vol. 108, no. 6, pp. 1384–1389, 1957.

- [39] C. Wehrenfennig, M. Liu, H. J. Snaith, M. B. Johnston, and L. M. Herz, “Charge carrier recombination channels in the low-temperature phase of organic-inorganic lead halide perovskite thin films,” *APL Mater.*, vol. 2, no. 8, p. 081513, 2014.
- [40] C. L. Davies *et al.*, “Bimolecular recombination in methylammonium lead triiodide perovskite is an inverse absorption process,” *Nat. Commun.*, vol. 9, no. 293, 2018.
- [41] J. Even, L. Pedesseau, C. Katan, B. Lauret, D. Saporì, and E. Deleporte, “Solid-State Physics Perspective on Hybrid Perovskite Semiconductors,” *J. Phys. Chem. C*, vol. 119, no. 19, pp. 10161–10177, 2015.
- [42] J. M. Frost, K. T. Butler, F. Brivio, C. H. Hendon, M. van Schilfgaarde, and A. Walsh, “Atomistic Origins of High-Performance in Hybrid Halide Perovskite Solar Cells,” *Nano Lett.*, vol. 14, no. 5, pp. 2584–2590, May 2014.
- [43] J. Singh, *Optical properties of condensed matter and applications*. John Wiley & Sons, 2006. ISBN:9780470021927
- [44] F. Urbach, “The Long-Wavelength Edge of Photographic Sensitivity and of the Electronic Absorption of Solids,” *Phys. Rev.*, vol. 92, no. 5, pp. 1324–1324, Dec. 1953.
- [45] S. De Wolf *et al.*, “Organometallic halide perovskites: Sharp optical absorption edge and its relation to photovoltaic performance,” *J. Phys. Chem. Lett.*, vol. 5, no. 6, pp. 1035–1039, 2014.
- [46] J. Even, L. Pedesseau, and C. Katan, “Analysis of multivalley and multibandgap absorption and enhancement of free carriers related to exciton screening in hybrid perovskites,” *J. Phys. Chem. C*, vol. 118, no. 22, pp. 11566–11572, 2014.
- [47] A. Miyata *et al.*, “Direct measurement of the exciton binding energy and effective masses for charge carriers in organic–inorganic tri-halide

Bibliography

perovskites,” *Nat. Phys.*, vol. 11, no. 7, pp. 582–587, Jul. 2015.

[48] C. Wehrenfennig, G. E. Eperon, M. B. Johnston, H. J. Snaith, and L. M. Herz, “High charge carrier mobilities and lifetimes in organolead trihalide perovskites,” *Adv. Mater.*, vol. 26, no. 10, pp. 1584–1589, 2014.

[49] S. D. Stranks *et al.*, “Electron-Hole Diffusion Lengths Exceeding 1 Micrometer in an Organometal Trihalide Perovskite Absorber,” *Science*, vol. 342, no. 2013, pp. 341–344, 2014.

[50] Y. Yamada, T. Nakamura, M. Endo, A. Wakamiya, and Y. Kanemitsu, “Photocarrier Recombination Dynamics in Perovskite $\text{CH}_3\text{NH}_3\text{PbI}_3$ for Solar Cell Applications,” *J. Am. Chem. Soc.*, vol. 136, no. 33, pp. 11610–3, Aug. 2014.

[51] C. S. Poncea *et al.*, “Organometal Halide Perovskite Solar Cell Materials Rationalized: Ultrafast Charge Generation, High and Microsecond-Long Balanced Mobilities, and Slow Recombination,” *J. Am. Chem. Soc.*, vol. 136, p. 5189–5192, 2014.

[52] M. N. Saha, “On a Physical Theory of Stellar Spectra,” *Proc. R. Soc. A Math. Phys. Eng. Sci.*, vol. 99, no. 697, pp. 135–153, May 1921.

[53] J. Szczytko, L. Kappei, J. Berney, F. Morier-Genoud, M. T. Portella-Oberli, and B. Deveaud, “Determination of the Exciton Formation in Quantum Wells from Time-Resolved Interband Luminescence,” *Phys. Rev. Lett.*, vol. 93, no. 13, 2004.

[54] R. L. Milot, G. E. Eperon, H. J. Snaith, M. B. Johnston, and L. M. Herz, “Temperature-Dependent Charge-Carrier Dynamics in $\text{CH}_3\text{NH}_3\text{PbI}_3$ Perovskite Thin Films,” *Adv. Funct. Mater.*, vol. 25, no. 39, pp. 6218–6227, Sep. 2015.

[55] A. D. Wright, R. L. Milot, G. E. Eperon, H. J. Snaith, M. B. Johnston, and L. M. Herz, “Band-Tail Recombination in Hybrid Lead Iodide Perovskite,” *Adv. Funct. Mater.*, vol. 27, no. 29, p. 1700860, Jun. 2017.

- [56] U. Rothlisberger *et al.*, “Origin of unusual bandgap shift and dual emission in organic-inorganic lead halide perovskites,” *Sci. Adv.*, vol. 2, no. 10, p. e1601156, 2016.
- [57] T. Baikie *et al.*, “Synthesis and crystal chemistry of the hybrid perovskite (CH₃NH₃)PbI₃ for solid-state sensitised solar cell applications,” *J. Mater. Chem. A*, vol. 1, no. 18, p. 5628, 2013.
- [58] P. S. Whitfield *et al.*, “Structures, Phase Transitions and Tricritical Behavior of the Hybrid Perovskite Methyl Ammonium Lead Iodide.,” *Sci. Rep.*, vol. 6, p. 35685, 2016.
- [59] L. D. Whalley, J. M. Frost, Y.-K. Jung, and A. Walsh, “Perspective: Theory and simulation of hybrid halide perovskites,” *J. Chem. Phys.*, vol. 146, p. 220901, 2017.
- [60] M. A. Pérez-Osorio *et al.*, “Vibrational Properties of the Organic-Inorganic Halide Perovskite CH₃NH₃PbI₃ from Theory and Experiment: Factor Group Analysis, First-Principles Calculations, and Low-Temperature Infrared Spectra,” *J. Phys. Chem. C*, vol. 119, no. 46, pp. 25703–25718, Nov. 2015.
- [61] A. D. Wright *et al.*, “Electron-phonon coupling in hybrid lead halide perovskites,” *Nat. Commun.*, vol. 7, no. 11755, 2016.
- [62] P. J. Dean, “Photoluminescence as a diagnostic of semiconductors,” *Prog. Cryst. Growth Charact.*, vol. 5, no. 1–2, pp. 89–174, Jan. 1982.
- [63] Q. Kim and D. W. Langer, “Effects of Excitation Intensity on Photoluminescence of Pure CdTe,” *Phys. status solidi*, vol. 122, no. 1, pp. 263–268, Mar. 1984.
- [64] D. E. Cooper, J. Bajaj, and P. R. Newman, “Photoluminescence spectroscopy of excitons for evaluation of high-quality CdTe crystals,” *J. Cryst. Growth*, vol. 86, no. 1–4, pp. 544–551, Jan. 1988.
- [65] T. Taguchi, J. Shirafuji, and Y. Inuishi, “Excitonic emission in cadmium

Bibliography

telluride," *Phys. status solidi*, vol. 68, no. 2, pp. 727–738, Apr. 1975.

[66] T. Schmidt, K. Lischka, and W. Zulehner, "Excitation-power dependence of the near-band-edge photoluminescence of semiconductors," *Phys. Rev. B*, vol. 45, no. 16, pp. 8989–8994, 1992.

[67] S. D. Stranks, V. M. Burlakov, T. Leijtens, J. M. Ball, A. Goriely, and H. J. Snaith, "Recombination Kinetics in Organic-Inorganic Perovskites: Excitons, Free Charge, and Subgap States," *Phys. Rev. Appl.*, vol. 2, no. 3, p. 034007, Sep. 2014.

[68] X. Wen *et al.*, "Defect Trapping States and Charge Carrier Recombination in Organic-Inorganic Halide Perovskites," *J. Mater. Chem. C*, vol. 4, pp. 793–800, Dec. 2016.

[69] E. M. Hutter *et al.*, "Direct-indirect character of the bandgap in methylammonium lead iodide perovskite," *Nat. Mater.*, vol. 16, no. 1, pp. 115–120, 2017.

[70] G. Meng *et al.*, "New insight into the ultra-long lifetime of excitons in organic–inorganic perovskite: Reverse intersystem crossing," *J. Energy Chem.*, vol. 27, no. 5, pp. 1496–1500, 2017.

[71] C. Piermarocchi, F. Tassone, V. Savona, A. Quattropani, and P. Schwendimann, "Nonequilibrium dynamics of free quantum-well excitons in time-resolved photoluminescence," *Phys. Rev. B*, vol. 53, no. 23, pp. 15834–15841, 1996.

[72] V. Perebeinos and P. Avouris, "Exciton Ionization, Franz–Keldysh, and Stark Effects in Carbon Nanotubes," *Nano Lett.*, vol. 7, no. 3, pp. 609–613, 2007.

[73] S. W. Koch, M. Kira, G. Khitrova, and H. M. Gibbs, "Semiconductor excitons in new light," *Nat. Mater.*, vol. 5, pp. 523–531, 2006.

[74] P. Andreakou, M. Brossard, C. Li, M. Bernechea, G. Konstantatos, and P. G. Lagoudakis, "Size- and temperature-dependent carrier dynamics in oleic

acid capped PbS quantum dots," *J. Phys. Chem. C*, vol. 117, no. 4, pp. 1887–1892, 2013.

[75] J. I. Pankove, *Optical Processes in Semiconductors*. Dover Publications, 2010. ISBN: 0800759602759

[76] T. H. Gfroerer, L. P. Priestley, F. E. Weindruch, and M. W. Wanlass, "Defect-related density of states in low-band gap double heterostructures grown on InP substrates," *Appl. Phys. Lett*, vol. 80, p. 4570, 2002.

[77] G. Li, M. Price, and F. Deschler, "Research Update: Challenges for high-efficiency hybrid lead-halide perovskite LEDs and the path towards electrically pumped lasing," *APL Mater.*, vol. 4, no. 9, p. 091507, Sep. 2016.

[78] M. Ahmadi, T. Wu, and B. Hu, "A Review on Organic-Inorganic Halide Perovskite Photodetectors: Device Engineering and Fundamental Physics," *Adv. Mater.*, vol. 29, no. 41, p. 1605242, Nov. 2017.

[79] M. A. Green, A. Ho-Baillie, and H. J. Snaith, "The emergence of perovskite solar cells," *Nat. Photonics*, vol. 8, no. 7, pp. 506–514, Jul. 2014.

[80] B. Conings *et al.*, "Intrinsic Thermal Instability of Methylammonium Lead Trihalide Perovskite," *Adv. Energy Mater.*, vol. 5, no. 15, p. 1500477, Aug. 2015.

[81] N. Aristidou *et al.*, "Fast oxygen diffusion and iodide defects mediate oxygen-induced degradation of perovskite solar cells," *Nat. Commun.*, vol. 8, p. 15218, May 2017.

[82] C. Bracher, B. G. Freestone, D. K. Mohamad, J. A. Smith, and D. G. Lidzey, "Degradation of inverted architecture $\text{CH}_3\text{NH}_3\text{PbI}_{3-x}\text{Cl}_x$ perovskite solar cells due to trapped moisture," *Energy Sci. Eng.*, vol. 6, no. 1, pp. 35–46, Feb. 2018.

[83] Z. Wang, Q. Lin, F. P. Chmiel, N. Sakai, L. M. Herz, and H. J. Snaith,

Bibliography

“Efficient ambient-air-stable solar cells with 2D–3D heterostructured butylammonium-caesium-formamidinium lead halide perovskites,” *Nat. Energy*, vol. 2, no. 9, p. 17135, Sep. 2017.

[84] G. Grancini *et al.*, “One-Year stable perovskite solar cells by 2D/3D interface engineering,” *Nat. Commun.*, vol. 8, p. 15684, Jun. 2017.

[85] A. Mei *et al.*, “A hole-conductor-free, fully printable mesoscopic perovskite solar cell with high stability,” *Science (80-.).*, vol. 345, no. 6194, pp. 295–298, Jul. 2014.

[86] Y. Chen, Y. Sun, J. Peng, J. Tang, K. Zheng, and Z. Liang, “2D Ruddlesden–Popper Perovskites for Optoelectronics,” *Adv. Mater.*, vol. 30, no. 2, p. 1703487, Jan. 2018.

[87] A. Vassilakopoulou, D. Papadatos, I. Zakouras, and I. Koutselas, “Mixtures of quasi-two and three dimensional hybrid organic-inorganic semiconducting perovskites for single layer LED,” *J. Alloys Compd.*, vol. 692, pp. 589–598, Feb. 2017.

[88] H. Tsai *et al.*, “High-efficiency two-dimensional Ruddlesden–Popper perovskite solar cells,” *Nature*, vol. 536, no. 7616, pp. 312–316, Aug. 2016.

[89] T. Kataoka, T. Kondo, R. Ito, S. Sasaki, K. Uchida, and N. Miura, “Magneto-optical study on excitonic spectra in (C₆H₁₃NH₃)₂PbI₄,” *Phys. Rev. B*, vol. 47, no. 4, pp. 2010–2018, Jan. 1993.

[90] I. Papagiannouli, E. Maratou, I. Koutselas, and S. Couris, “Synthesis and Characterization of the Nonlinear Optical Properties of Novel Hybrid Organic–Inorganic Semiconductor Lead Iodide Quantum Wells and Dots,” *J. Phys. Chem. C*, vol. 118, no. 5, pp. 2766–2775, Feb. 2014.

[91] Q. Wang, X.-D. Liu, Y.-H. Qiu, K. Chen, L. Zhou, and Q.-Q. Wang, “Quantum confinement effect and exciton binding energy of layered perovskite nanoplatelets,” *AIP Adv.*, vol. 8, no. 2, p. 025108, Feb. 2018.

[92] J. A. Sichert *et al.*, “Quantum Size Effect in Organometal Halide Perovskite Nanoplatelets,” *Nano Lett.*, vol. 15, no. 10, pp. 6521–6527, Oct. 2015.

[93] C. C. Stoumpos *et al.*, “Ruddlesden–Popper Hybrid Lead Iodide Perovskite 2D Homologous Semiconductors,” *Chem. Mater.*, vol. 28, no. 8, pp. 2852–2867, Apr. 2016.

[94] R. L. Milot *et al.*, “Charge–Carrier Dynamics in 2D Hybrid Metal–Halide Perovskites,” *Nano Lett.*, vol. 16, no. 11, pp. 7001–7007, Nov. 2016.

[95] M. R. Filip, G. E. Eperon, H. J. Snaith, and F. Giustino, “Steric engineering of metal-halide perovskites with tunable optical band gaps,” *Nat. Commun.* 2014 5, vol. 5, no. 1, p. 5757, Dec. 2014.

[96] I. C. Smith, E. T. Hoke, D. Solis-Ibarra, M. D. McGehee, and H. I. Karunadasa, “A Layered Hybrid Perovskite Solar-Cell Absorber with Enhanced Moisture Stability,” *Angew. Chemie Int. Ed.*, vol. 53, no. 42, pp. 11232–11235, Oct. 2014.

[97] D. B. Mitzi, “Templating and structural engineering in organic–inorganic perovskites,” *J. Chem. Soc. Dalt. Trans.*, vol. 0, no. 1, pp. 1–12, Jan. 2001.

[98] L. Mao *et al.*, “Hybrid Dion–Jacobson 2D Lead Iodide Perovskites,” *J. Am. Chem. Soc.*, vol. 140, no. 10, pp. 3775–3783, Mar. 2018.

[99] C. Myae Myae Soe *et al.*, “New Type of 2D Perovskites with Alternating Cations in the Interlayer Space, $(C(NH_2)_3(CH_3NH_3)_nPb_nI_{3n+1}$: Structure, Properties, and Photovoltaic Performance,” *J. Am. Chem. Soc.*, vol. 139, p. 19, 2017.

[100] Z. Song, S. C. Watthage, A. B. Phillips, B. L. Tompkins, R. J. Ellingson, and M. J. Heben, “Impact of Processing Temperature and Composition on the Formation of Methylammonium Lead Iodide Perovskites,” *Chem. Mater.*, vol. 27, no. 13, pp. 4612–4619, Jul. 2015.

[101] D. Bi *et al.*, “Efficient luminescent solar cells based on tailored mixed-

Bibliography

cation perovskites,” *Sci. Adv.*, vol. 2, no. 1, p. e1501170, Jan. 2016.

[102] N.-G. Park, “Nonstoichiometric Adduct Approach for High-Efficiency Perovskite Solar Cells,” *Inorg. Chem.*, vol. 56, no. 1, pp. 3–10, Jan. 2017.

[103] M. L. Petrus *et al.*, “The Influence of Water Vapor on the Stability and Processing of Hybrid Perovskite Solar Cells Made from Non-Stoichiometric Precursor Mixtures,” *ChemSusChem*, vol. 9, no. 18, pp. 2699–2707, Sep. 2016.

[104] S. Lilliu *et al.*, “Grain rotation and lattice deformation during perovskite spray coating and annealing probed *in situ* by GI-WAXS,” *CrystEngComm*, vol. 18, no. 29, pp. 5448–5455, Jul. 2016.

[105] A. A. Petrov *et al.*, “Crystal Structure of DMF-Intermediate Phases Uncovers the Link Between $\text{CH}_3\text{NH}_3\text{PbI}_3$ Morphology and Precursor Stoichiometry,” *J. Phys. Chem. C*, vol. 121, no. 38, pp. 20739–20743, Sep. 2017.

[106] D. H. Cao, C. C. Stoumpos, O. K. Farha, J. T. Hupp, and M. G. Kanatzidis, “2D Homologous Perovskites as Light-Absorbing Materials for Solar Cell Applications,” *J. Am. Chem. Soc.*, vol. 137, no. 24, pp. 7843–7850, Jun. 2015.

[107] Y. Yang *et al.*, “Annealing Induced Re-crystallization in $\text{CH}_3\text{NH}_3\text{PbI}_3-x\text{Cl}_x$ for High Performance Perovskite Solar Cells,” *Sci. Rep.*, vol. 7, no. 1, p. 46724, Dec. 2017.

[108] Y. Tian *et al.*, “Giant photoluminescence blinking of perovskite nanocrystals reveals single-trap control of luminescence,” *Nano Lett.*, vol. 15, no. 3, pp. 1603–1608, 2015.

[109] M. Yuan *et al.*, “Perovskite energy funnels for efficient light-emitting diodes,” *Nat. Nanotechnol.*, vol. 11, no. 10, pp. 872–877, Oct. 2016.

[110] D. Papadatos, A. Vassilakopoulou, and I. Koutselas, “Yellow Light Energy Transfer Emitting Diodes Based on mixed Quasi-2D Perovskites,” *J.*

Lumin., vol. 188, pp. 567–576, Nov. 2016.

[111] Q. Shang *et al.*, “Unveiling Structurally Engineered Carrier Dynamics in Hybrid Quasi-Two-Dimensional Perovskite Thin Films toward Controllable Emission,” *J. Phys. Chem. Lett.*, vol. 8, no. 18, pp. 4431–4438, Sep. 2017.

[112] N. Mercier, S. Poiroux, A. Riou, and P. Batail, “Unique Hydrogen Bonding Correlating with a Reduced Band Gap and Phase Transition in the Hybrid Perovskites (HO(CH₂)NH₃)₂PbX₄ (X = I, Br),” *Inorg. Chem.*, vol. 43, pp. 8361–8366, 2004.

[113] D. Meggiolaro *et al.*, “Iodine chemistry determines the defect tolerance of lead-halide perovskites,” *Energy Environ. Sci.*, vol. 11, no. 3, pp. 702–713, Mar. 2018.

[114] J. Qian, Q. Guo, L. Liu, B. Xu, and W. Tian, “A theoretical study of hybrid lead iodide perovskite homologous semiconductors with 0D, 1D, 2D and 3D structures,” *J. Mater. Chem. A*, vol. 5, no. 32, pp. 16786–16795, Aug. 2017.

[115] J. Xing *et al.*, “Color-stable highly luminescent sky-blue perovskite light-emitting diodes,” *Nat. Commun.*, vol. 9, no. 1, p. 3541, Dec. 2018.

[116] J. Huang, S. Tan, P. D. Lund, and H. Zhou, “Impact of H₂O on organic–inorganic hybrid perovskite solar cells,” *Energy Environ. Sci.*, vol. 10, no. 11, pp. 2284–2311, Nov. 2017.

[117] M. I. Saidaminov *et al.*, “High-quality bulk hybrid perovskite single crystals within minutes by inverse temperature crystallization,” *Nat. Commun.*, vol. 6, no. 1, p. 7586, Nov. 2015.

[118] K. C. B. Lee *et al.*, “Application of the Stretched Exponential Function to Fluorescence Lifetime Imaging,” *Biophys. J.*, vol. 81, no. 3, pp. 1265–1274, Sep. 2001.

[119] J. Kröger, “Stretched exponential relaxation in molecular and electronic

Bibliography

glasses,” *Reports Prog. Phys.*, vol. 69, no. 4, pp. 899–969, 2006.

[120] D. Shi *et al.*, “Low trap-state density and long carrier diffusion in organolead trihalide perovskite single crystals,” *Science (80-.)*, vol. 347, no. 6221, pp. 519–522, Jan. 2015.

[121] L. Q. Phuong, Y. Yamada, M. Nagai, N. Maruyama, A. Wakamiya, and Y. Kanemitsu, “Free Carriers versus Excitons in $\text{CH}_3\text{NH}_3\text{PbI}_3$ Perovskite Thin Films at Low Temperatures: Charge Transfer from the Orthorhombic Phase to the Tetragonal Phase,” *J. Phys. Chem. Lett.*, vol. 7, no. 13, pp. 2316–2321, Jun. 2016.